이학박사 학위논문

Dzyaloshinskii-Moriya Interaction in Pt/Co/NM Trilayer Systems : Beyond the Interfacial Perspective

Pt/Co/NM 자성박막에서의 Dzyaloshinskii-Moriya 상호작용 : 계면 현상적 관점을 넘어선 현상에 대한 연구

2020 년 2 월

서울대학교 대학원

물리천문학부

박 용 근

Dzyaloshinskii-Moriya Interaction in Pt/Co/NM Trilayer Systems : Beyond the Interfacial Perspective

Yong-Keun Park

Supervised by

Professor Sug-Bong Choe

A Dissertation in Physics

Submitted to the Faculties of

Seoul National University

in Partial Fulfillment of the Requirements for the Degree of

Doctor of Philosophy

February 2020

Department of Physics and Astronomy

The Graduate College of Natural Sciences

Seoul National University

Dzyaloshinskii-Moriya Interaction in Pt/Co/NM Trilayer Systems : Beyond the Interfacial Perspective

Pt/Co/NM 자성박막에서의 Dzyaloshinskii-Moriya 상호작용 : 계면 현상적 관점을 넘어선 현상에 대한 연구

지도교수 최석봉

이 논문을 이학박사 학위논문으로 제출함

2020년 1월

서울대학교 대학원

물리천문학부

박 용 근

박용근의 이학박사 학위논문을 인준함

2019년 12월

위 원 장 이 탁 희 (인)

부위원장 최 석 봉 (인)

위 원 정 현 석 (인)

위 원 김 도 헌 (인)

위 원 민 병 철 (인)

Abstract

Extensive efforts have been made to understand the Dzyaloshinskii-Moriya interaction (DMI) owing to its peculiar properties for realizing chiral spin structures in magnetic systems with broken inversion symmetry. A sizeable DMI generates an inbuilt chirality of magnetic domain walls (DWs), which is essential for current-induced DW motion via spin orbit torques (SOTs). The ultimate speed of the DW motion has been revealed to be governed by DMI strength. Moreover, a sizeable DMI is an essential component in generating magnetic skyrmions, which can be used in high-density digital technologies for racetrack memory and logic devices. Therefore, DMI engineering is also important to this field in its attempts toward large DMIs.

Early studies of the DMI were conducted in an antiferromagnetic oxide system understood by three-site atomic super-exchange interaction, established by I. Dzyaloshinskii and T. Moriya in 1960. The conduction electron-mediated DMI mechanism in metallic systems was suggested by A. Fert and P.M. Levy by means of spin-orbit scattering in 1980, and recent research has suggested that the DMI is linked with conduction electron-related phenomena in metallic systems. Therefore, numerous efforts have been devoted to understanding the underlying physics of DMIs, although the most significant parameters and mechanisms for DMI are still under debate.

The commonly accepted concept for DMIs in multilayer systems is that the DMI is an interfacial effect. Therefore, interest in the DMI has been primarily

focused on interfaces, and many attempts at enlarging the DMI strength have been conducted by engineering the interface conditions, changing the materials adjacent to the ferromagnetic layer, and inserting thin layers at interfaces. However, if DMI is understood and realized simply as an interfacial effect, there will be limited ways of increasing its strength because the strength of the DMI may be determined by only the relevant properties of the materials that form the interface, and there are only two interfaces sitting adjacent to the ferromagnetic layer. In addition, the most popularly employed materials for DMIs are certain heavy metals, because it has been understood that the DMI strength is related to the spin-orbit coupling strength.

We conducted studies to further understand the DMI and to discover and suggest new directions for DMI engineering, with the goal of eventually overcoming the limit. In Chapter 1, we introduce the basic physics of ferromagnetism, the suggested mechanism for DMIs, and the measurement techniques employed. The measurement techniques for DMIs are the same for each chapter, and therefore a detailed introduction of these techniques is given in Chapter 1, with the method explained briefly in each subsequent chapter. Following Chapter 1, the DMI, according to the change of each part in a trilayer system is studied. In Chapters 2, 3, and 4, non-magnetic material dependence, ferromagnetic layer thickness dependence, and non-magnetic layer thickness dependence of the DMI are investigated and presented, respectively. While the research in Chapters 2, 3, and 4 mainly examine the physical aspects of DMIs, the research in Chapter 5 attempts to achieve efficient device applications through DMI engineering.

In Chapter 2, the most decisive parameter in the DMI, the work function of non-magnetic metal, is found for the Pt/Co/X trilayer system. The inferred mechanism and the relationship between the work function and the DMI is discussed. After the investigations in Chapter 2, further research mainly focuses on Pt/Co/W and Pt/Co/Cu systems, because of the peculiar properties in these systems. Detailed research and discussions are presented in Chapters 3–5.

In Chapter 3, it is shown that the DMI trend, with respect to Co thickness, derives from an inverse proportionality to the Co thickness in Pt/Co/W and Pt/Co/Cu/W systems. Conversely, it has been typically expected that interfacial phenomena follow trends of inverse proportionality to the ferromagnetic layer thickness, but our measurement data suggests that there exists a critical Co thickness for the full emergence of DMI, which is inferred via the derivation from the inverse proportionality. Unlike the DMI, the strength of the SOT generated by the spin Hall effect in the non-magnetic metal layer is inversely proportional to the Co thickness. This difference between the DMI and SOT suggests that the origin of the interfacial effect is important for understanding the DMI's tendencies in relation to Co thickness.

In Chapter 4, it was found that the DMI has an oscillating tendency with respect to the Cu thickness in a Pt/Co/Cu trilayer system. To analyze the DMI oscillation period with respect to the Cu orientation, and to compare this with the oscillations of similar samples and phenomena in quantum well states, the Ruderman-Kittel-Kasuya-Yosida interaction is also measured in Co/Cu/(Pt)/Co spin

valve systems. From this, it was inferred that the DMI oscillation can be linked to the quantum well state in Cu.

In Chapter 5, from the research results for Cu, attempts were made to simultaneously increase the thermal stability and reduce the magnetization switching current density. It is understood that it is typically difficult to satisfy both at the same time. By inserting an ultrathin Cu layer at the Co/Pt interface in Pt/Co/Pt trilayers, it was possible to accomplish these simultaneously. The most important result of the Cu layer insertion was the simultaneous increase of perpendicular magnetic anisotropy (PMA) and DMI. It was confirmed that the increase of thermal stability resulted from the increase of PMA, and that the decrease of switching current density resulted from the increase of DMI.

In Chapter 6, the outlook of the results introduced in this thesis is suggested. Our main findings in this thesis—based on the fact that DMI will be affected by conduction electrons-mediated effects—provide further physical understanding of DMI, and suggest possible new directions for DMI engineering for magnetic trilayer and multilayer systems.

Keyword: domain wall, Dzyoshinskii-Moriya interaction, spin orbit torque, perpendicular magnetic anisotropy, work function, conduction electron, quantum well, Ruderman-Kittel-Kasuya-Yosida interaction, magnetization switching

Student number: 2014-21344

Contents

List of Figures

List of Tables

Chapter 1

Introduction

1.1. Sample fabrication

1.1.1 PMA film deposition

Since the discovery of perpendicular magnetic anisotropy (PMA) in ultrathin magnetic multilayered systems, many studies have been conducted on the PMA system in an attempt to understand the physical phenomena as well as to realize magnetic device applications such as racetrack memory. In layered systems, the magnetic anisotropy is understood by the following relation for ferromagnetic layer thickness t_{FM} [1,2], $K_{\mathrm{U}}^{\mathrm{eff}} = \left(K_{\mathrm{V}} - \frac{1}{2}\mu_0 M_{\mathrm{S}}^2\right) + \frac{K_{\mathrm{S}}^{\mathrm{tot}}}{t_{\mathrm{FM}}}$. Here, $K_{\mathrm{U}}^{\mathrm{eff}}$ is the effective uniaxial anisotropy, K_{V} is the volume anisotropy, M_{S} is the saturation magnetization, and $K_{\mathrm{S}}^{\mathrm{tot}}$ is the total surface magnetic anisotropy. The term $\frac{1}{2}\mu_0 M_{\mathrm{S}}^2$ is the demagnetization energy term of the sample, and is sometimes combined with K_{V} to express effective volume magnetic anisotropy $K_{\mathrm{V}}^{\mathrm{eff}}\left(= K_{\mathrm{V}} - \frac{1}{2}\mu_0 M_{\mathrm{S}}^2\right)$. The equation for $K_{\mathrm{U}}^{\mathrm{eff}}$ is usually written in the form $K_{\mathrm{U}}^{\mathrm{eff}} t_{\mathrm{FM}} = K_{\mathrm{V}}^{\mathrm{eff}} t_{\mathrm{FM}} + K_{\mathrm{S}}^{\mathrm{tot}}$. Typically, when $K_{\mathrm{U}}^{\mathrm{eff}}$ is positive, it is defined as PMA, and if negative, the easy-axis is in-plane.

Figure 1.1 is a $K_{\mathrm{U}}^{\mathrm{eff}} t_{\mathrm{FM}} - t_{\mathrm{FM}}$ plot for the Pt/Co/W trilayer samples fabricated for experiments and it is typical of layered thin film systems. As shown in Fig. 1.1,

the magnetic layer thickness must be thin enough for the PMA to appear. In the case of Pt/Co layered systems, the samples exhibit PMA when the thickness is $\sim 0.3\ \text{nm} \leq t_{\text{FM}} \leq \sim 1.3\ \text{nm}$ [3].

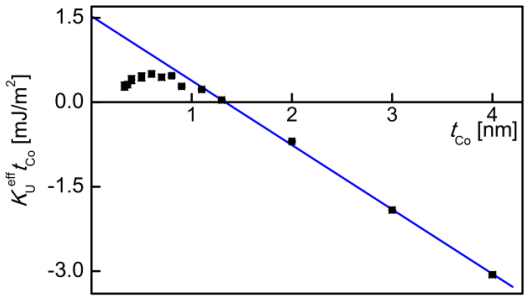

Figure 1.1 $K_{\text{U}}^{\text{eff}} t_{\text{Co}} - t_{\text{Co}}$ plot of 3 nm Pt/t_{Co} nm Co/ 0.6 nm Cu/5 nm W trilayer. The blue line is the linear fitting line.

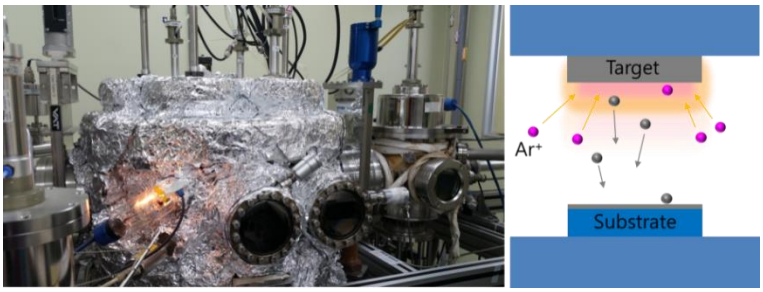

Figure 1.2 Ultrahigh vacuum DC magnetron sputtering system.

The PMA is present in several atomic monolayers (MLs), and therefore, the film quality of the ultrathin magnetic layer is important. For this, ultrathin films

were deposited in an ultrahigh vacuum DC magnetron sputtering system at a base pressure of less than 5×10^{-8} Torr (Fig. 1.2). The working pressure was set to 2 mTorr using 99.999% Ar gas, and the deposition rate (~ 0.4 Å/s) was minimized by reducing the power of the sputter gun to ~ 10 W within the stable limits of Ar plasma in the DC magnetron sputtering system, for precise thin film thickness control. The films were deposited on a 500-μm Si (100) / 100-nm SiO_2 substrate or a 500-μm Si (100) / 300-nm SiO_2 substrate with dry oxidation of SiO_2.

In the case of a commonly manufactured Pt/Co system, it is understood that PMA appears only when the fcc Co layer has the growth orientation (111) on the fcc Pt (111) layer [4-6]. Our Pt/Co system was confirmed to have the fcc structure by a grazing incidence X-ray diffraction (GI-XRD) measurement (Fig. 1.3). The formation of a clear bubble domain exhibiting PMA observed by magneto-optical Kerr effect (MOKE) microscopy, in up to 0.3 nm of Co, is possible (Fig. 1.4).

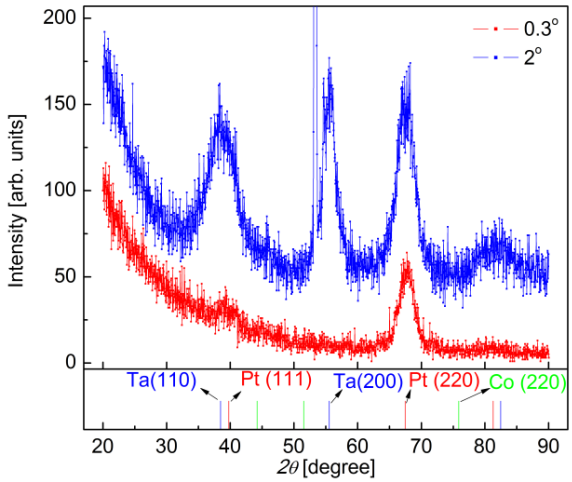

Figure 1.3 GI-XRD data of 2.5 nm Pt/1.1 nm Co/4 nm Pt trilayer. The X-ray beam incident angles are denoted in the figure. The peaks of Pt, Ta, and Co are denoted in the lower part of the plot, and with a different color. The sharp peak near 53.3° is from the substrate.

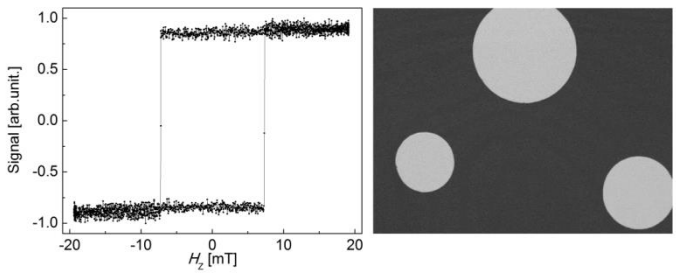

Figure 1.4 Out-of-plane hysteresis loop and domain image of 2.5 nm Pt/0.3 nm Co/1.5 nm Pt trilayer. The hysteresis loop was obtained by MOKE. In the domain image, the brighter region is the up-domain and the darker region is the down-domain.

1.1.2 Microwire and Hall bar patterning process

Samples for domain wall (DW) motion experiments or spin torque efficiency ε measurements were mainly fabricated into microwires of 5-20 μm width and 100-400 μm length. Cross-shape Hall bars of ~10 μm width were fabricated for measuring the effective magnetic anisotropy field H_K through the magneto-resistance (MR) measurements and magnetization switching experiments of Chapters 4 and 5.

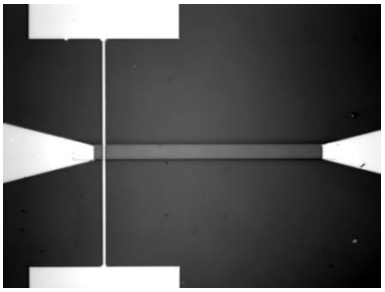

Figure 1.5 Image of patterned microwire structure. The rectangular structure at the center of the image is patterned magnetic film (350-μm length and 20-μm width), and the brighter structures at the edges of the image are 5-nm Ti/100-nm Au electrodes.

The conditions of the processes are detailed below.

● Photo-Lithography

First, photo-resist (PR) was coated onto the films for 5 seconds at 500 RPM, and then 30 seconds at 3000 RPM. The PR used was AZ 4210 MIF (positive tone). Next, the PR-coated films were baked at 110℃, for 2 minutes on a hot plate. Then, ultra-violet (UV) light was exposed to the films to form patterns, and the mask align and photo-lithography system employed was MA-6 (SUSS) with a UV light lamp. The exposure dose was $150\ \mathrm{mJ/cm^2}$. Subsequently, the UV-exposed samples were developed. The developer used was AZ 300 MIF, and the developing time was 1.5 minutes. Finally, the samples were rinsed for 30 seconds with distilled water, and then N_2 gas blowing was conducted for 30 seconds.

● E-Beam-lithography

First, e-beam-resist (ER) was coated on the films for 10 seconds at 500 RPM, and then 30 seconds at 3000 RPM. The ERs used were ma-N 2403 (negative tone), and 950 PMMA A2 (positive tone). Next, the ER-coated films were baked at 90℃, 2-minutes for ma-N 2403 on a hot plate, and 120 ℃, 1.5 minutes for 950 PMMA A2 on a hot plate. Then, e-beam lithography was conducted using a JEOL JSM-6500F scanning electron microscope system with a 20 keV intensity. The exposure dose were $80-250\ \mu\mathrm{C/cm^2}$ for ma-N 2403, and $100-160\ \mu\mathrm{C/cm^2}$ for 950 PMMA A2. Subsequently, the samples were developed. The developers used were

ma-D 332 for ma-N 2403, the developing time was 50 seconds, and MIBK:IPA (3:1) for 950 PMMA A2, with a developing time of 60 seconds. Finally, the samples were rinsed for 30 seconds with distilled water for ma-N 2403, and with isopropyl alcohol for 950 PMMA A2. Finally, N_2 gas blowing was conducted.

- Dry etch process

After the PR or ER patterning processes, a dry etching process using Ar ions was conducted in a milling chamber with base pressure of 2×10^{-6} Torr, to fabricate the microwire and hall bar structure. The angle perpendicular to the film plane was set as zero degrees, and milling was first performed at 10 degrees with 300 V and 0.3 A, then the structure edge was milled to 70 degrees with 300 V and 0.3 A. After milling, the samples were placed in acetone, to remove PR or ER with ultra-sonic radiation. Then, the samples were rinsed with methanol, and N_2 gas blowing was conducted for 30 seconds.

- Lift-off process

After the deposition of 5 nm Cr/ 100 nm Au or 5 nm Ti/ 100 nm Au electrodes, a lift-off process was performed to remove PR with acetone and ultra-sonic radiation. Then, the samples were rinsed with methanol, and N_2 gas blowing was conducted for 30 seconds.

1.1.3 Basic magnetic properties characterization

- The M_S and H_K estimations from vibrating sample magnetometer (VSM)

In the easy-axis loop measured by the vibrating sample magnetometer (VSM), M_S was obtained from the average magnetization value of each saturation region (Fig. 1.6a). In the hard axis loop H_K, the effective field of magnetic anisotropy, was obtained from the intersection of each fitting line between the region and each saturation region (Fig. 1.6b). From the relation of $K_U^{eff} = \frac{1}{2}\mu_0 M_S H_K$, K_U^{eff} is estimated [7].

- The H_K estimation from the hard-axis hysteresis loop measurement by MR from the anomalous Hall effect

If H_K is too large, it is difficult to see the saturation of the hysteresis loop in the hard axis with VSM. In this case, H_K was obtained from the hard-axis hysteresis loop by measuring the MR from the anomalous Hall effect (AHE) [7-9].

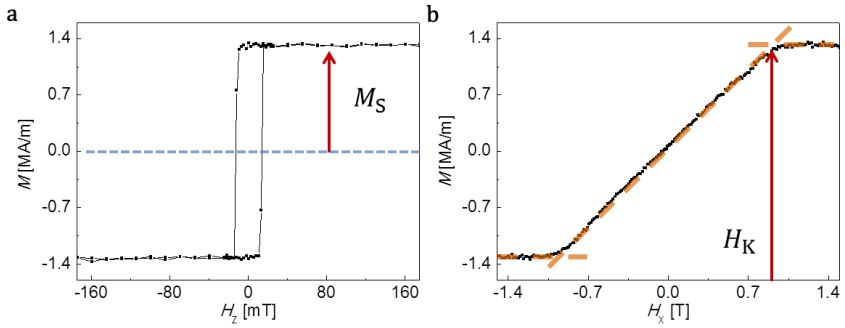

Figure 1.6 Hysteresis loop obtained by VSM. a. The easy-axis hysteresis loop. The M_S is denoted in the figure. The blue horizontal line is where $M = 0$. **b.** The hard axis hysteresis loop. H_K is denoted in the figure. The orange lines are linear fitting lines at saturation regions and slope regions. The red arrows indicate the intersection positions between the fitting lines.

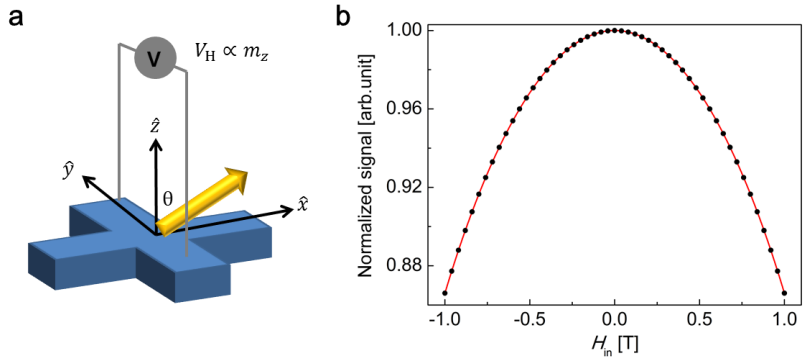

Figure 1.7 Measurement from hard-axis MR hysteresis loop. a. The schematic depiction of magnetic field and angles. **b.** Normalized MR signal of patterned Hall bar, with respect to H_{in}.

When an external magnetic field is induced to magnetization, the change in the hysteresis loop can be explained by the Stoner-Wohlfarth (SW) model [7-9]. The magnetic energy volume density is known as $E = K_{\mathrm{U}}^{\mathrm{eff}}\sin^2\theta - \mu_0 M_{\mathrm{S}} H_{\mathrm{ext}}\cos(\theta - \phi)$, where H_{ext} is the external magnetic field, θ is the angle of magnetization, and ϕ is the angle of the external magnetic field (Fig. 1.7a). Using $K_{\mathrm{U}}^{\mathrm{eff}} = \frac{1}{2}\mu_0 M_{\mathrm{S}} H_{\mathrm{K}}$ and the energy differential to find the stabilization in terms of θ, $\frac{\partial E}{\partial \theta} = M_{\mathrm{S}} H_{\mathrm{K}}\sin\theta_{\mathrm{eq}}\cos\theta_{\mathrm{eq}} + M_{\mathrm{S}} H_{\mathrm{oop}}\sin\theta_{\mathrm{eq}} - M_{\mathrm{S}} H_{\mathrm{in}}\cos\theta_{\mathrm{eq}} = 0$ is obtained. Here, H_{oop} is the external magnetic field in the direction perpendicular to the film plane, and H_{in} is the in-plane direction. If θ_{eq} is small, the equation is simplified and the result can be expressed by $m_z = \cos\theta_{\mathrm{eq}} \cong 1 - \frac{H_{\mathrm{in}}^2}{2\left(H_{\mathrm{K}} + H_{\mathrm{oop}}\right)^2}$. Since the MR signal from AHE is proportional to the vertical component m_z of the magnetization [9], when H_{in} is changed by a small and constant H_{oop}, H_{K} can be obtained from the fitting by measuring the MR signal (Fig. 1.7b).

1.2 The Dzyaloshinskii-Moriya Interaction

The Dzyaloshinskii-Moriya Interaction (DMI) is an interaction that allows the spin to have a chiral structure. The DMI was first proposed on phenomenological grounds by I. Dzyaloshinskii in 1958 [10], and T. Moriya explained it theoretically with the super-exchange interaction model in 1960 [11]. The simple Hamiltonian form of DMI is represented by $E_{\mathrm{DMI}} = -\vec{D} \cdot \left(\vec{S_\iota} \times \vec{S_J}\right)$. Here, the $\vec{D}$ is the DMI

vector, and its intensity determines the strength of the DMI, D. For the two spins S_i and S_j, the chirality is determined by the direction of $\vec{D}$, (Fig. 1.8).

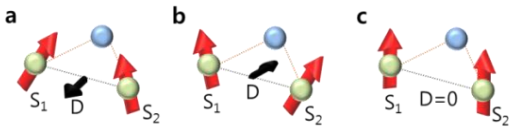

Figure 1.8 Spin chirality dependence on $\vec{D}$. a. Left-handed chirality, **b.** Right-handed chirality, **c.** No chirality (DMI = 0).

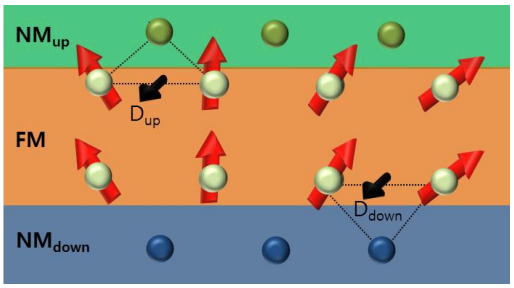

Figure 1.9 Broken inversion symmetry and spin texture in trilayer system. Each D-vector is drawn in the figure. The circles depict ferromagnetic and non-magnetic material atoms.

The DMI is an indirect exchange interaction and hence, the characteristics of the interaction depend on the position of the atom and the material between the two spins. For the same atom, the chirality is reversed depending on its position (Figs.

1.8a and b). If there is an asymmetry between two spins, the DMI takes a non-zero value (Figs. 1.8a and 1.8b) however, for the symmetric case, the DMI is zero. Therefore, it is important that the DMI emerges from the broken inversion symmetry system. If the samples are layer structures, the interface between the ferromagnetic (FM) layer and the adjacent non-magnetic (NM) layer is the place where the inversion symmetry is broken (Fig. 1.9). In such cases, the DMI manifests itself at the interface, and is commonly understood as an interfacial effect, often called interfacial DMI (Fig. 1.9).

Because DMI significantly affects the energy, static, and dynamic properties of spin chiral structures, a deep understanding of the DMI is required. Recent interest in the DMI focuses on the magnitude and sign of the DMI at the interface. To obtain a larger DMI, the DMI strength itself at interfaces needs to be large, and the DMI signs at the two interfaces in the vicinity of the ferromagnetic layer should be different from each other. For example, in a symmetric system such as Pt/Co/Pt, the DMI signs of the Pt/Co and the Co/Pt interface oppose and thus cancel out each other, so a small DMI is expected.

The DMI is a spin orbit coupling (SOC) phenomenon [11] and as a result, theoretical predictions and experimental measurements have been performed for heavy metals (HMs) such as Pt, which is known to have a large SOC strength. However, there is still a need for a better understanding of DMIs, and it remains difficult to clearly predict which materials, combinations, and structures generate larger DMIs.

1.2.1. DMI by anisotropic super-exchange interaction

I. Dzyaloshinskii and T. Moriya explained the phenomenon of the weak ferromagnetism of antiferromagnet α–Fe_2O_3 as tilting between anti-parallel aligned spins. The α–Fe_2O_3 system has a net magnetic moment of zero, due to the anti-parallel arrangement between spins, however, a weak net magnetic moment $\vec{m}_{\mathrm{net}}$ in one direction can be caused by chiral spin tilting (Fig. 1.10) [10,11]. Since its discovery, DMI has mainly been studied in oxide systems.

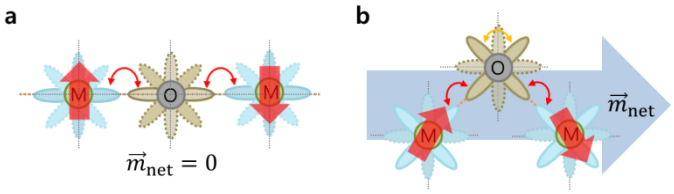

Figure 1.10 Net magnetic moment of antiferromagnet with spin tilting. a. Without DMI in symmetric structure, **b.** With DMI in asymmetric structure.

1.2.2. DMI by spin orbit scattering

In 1980, A. Fert and P.M. Levy predicted that spin chiral effects may occur due to spin orbit scattering [12]. Their study theoretically explained the formation of spin chiral structures around impurity atoms when there are impurity atoms in spin glasses such as CuMn alloy. It is reported that the tilting of spins occurs due to the scattering between the conduction electrons mediating the interactions of local spins and the orbitals of the impurity atom (Fig. 1.11). Because Moriya's calculations

showed the parallel and chiral terms occurring between spins by the super-exchange interaction [11], A. Fert and P.M. Levy compared the Ruderman-Kittel-Kasuya-Yosida (RKKY) interaction (spin parallel) with the DMI by spin orbit scattering (spin chiral), through conduction electron-mediated spin interactions [12].

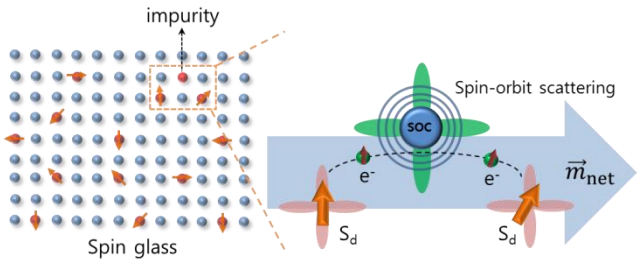

Figure 1.11 Illustration of spin orbit scattering in spin glass system. The e^- are conduction electrons. The S_{d} are local spins.

1.2.3. DMI by Rashba interaction and RKKY interaction

After Fert and Levy's work, some studies were published showing that the DMI can be understood by, or related to, Rashba and RKKY interactions [13-15]. In these studies, the DMI is expected to show oscillation characteristics in the magnitude and sign according to the distance between the spins, similar to the RKKY interaction. Although this prediction was confirmed experimentally [16], these were mainly studied theoretically.

1.2.4. DMI by orbital characteristic and interfacial charge distribution

It was found by S. Kim *et al*. that the magnitude of the DMI and the vertical orbital moment of Co correlate with each other in the Pt/Co/MgO system [17]. Although a model exists showing the relationship between the components of the orbital moment and the Rashba coefficient [18,19], there are many factors that determine this orbital moment and so it is not clearly understood whether it is explicitly related to the Rashba effect. In addition, a theoretical calculation shows that there is a correlation between the relative electric dipole change, Fermi level, and DMI energy due to the change of charge distribution near the interface [20].

1.3. DMI and SOT measurement - spin torque efficiency measurement technique

1.3.1 Spin Hall effect and SOT generated by spin Hall effect

When electric current flows through the non-magnetic metal layers, its trajectory of motion changes depending on the spin of the conduction electrons. This phenomenon is called the spin Hall effect (SHE) [21]. One of the mechanisms explaining the causes of the SHE is a skew scattering mechanism, in which the scattering trajectory varies depending on the spin of the electrons. This occurs when there is an impurity in the material and SOC with a conduction electron near the impurity [21]. Another mechanism is an intrinsic one arising from the anomalous

velocity caused by the difference in the Berry curvature, which is dependent on the spin [21]. Another mechanism is the side jump mechanism, which accounts for the scattering and trajectory differences caused by the difference in Berry phase due to the spin near the impurity [21]. In the SHE, spin polarization of charge current occurs mainly in the NM layer (Fig. 1.12). Due to the SHE effect, spin current J_S can be generated and injected into the FM, inducing spin orbit torque (SOT) in the magnetization of FM.

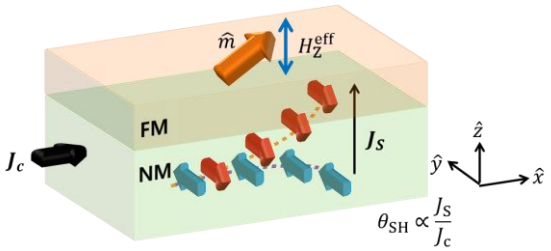

Figure 1.12 Spin Hall effect in non-magnetic metal layer.

The SOT by SHE is understood by the relation $\frac{\hbar\theta_{SH}}{2eM_S t_{FM}}\hat{m} \times \left(\hat{m} \times (\hat{z} \times J_c)\right)$ [22]. Here, θ_{SH} is the rate at which charge current is converted to spin current in the NM, the so-called spin Hall angle, $\hat{m}$ is the unit vector indicating the magnetization direction in FM, J_c is the charge current. The larger the SOC strength of the NM material, the larger the θ_{SH} expected, and hence, a larger SOT is usually expected.

1.3.2. DMI estimation scheme by spin torque efficiency measurement

The DMI can be understood as the H_{DMI}, the effective magnetic field of the DMI, acting on the magnetization inside the DWs [22,23]. In PMA systems, a Bloch type DW, which has a gradual change on the DW surface, is more energy-efficient than a Néel type DW, which has a gradual change on perpendicular direction from the DW surface [23]. However, if the DMI is large enough, the Néel type DW, which has a structure that gradually changes in the direction perpendicular to the DW plane, becomes more stable (Fig. 1.13b) [23]. The H_{DMI} acts like a magnetic field in the direction perpendicular to the DW plane, making a Néel type DW preferable [23]. Notably, when the DMI strength is sufficiently strong, the chirality of the DWs are determined by the sign of the DMI (Fig. 1.13).

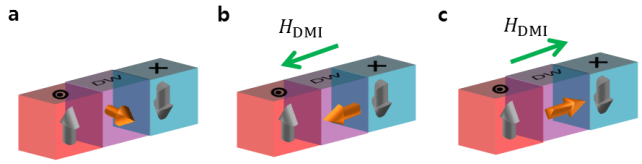

Figure 1.13 Domain wall type and effects of DMI to DW. a. Bloch type domain wall ($D = 0$). **b.** Néel type domain wall (left-handed chirality, $D < 0$) and **c,** Néel type domain wall (right-handed chirality, $D > 0$). The directions of the H_{DMI} induced in the DW are denoted in the figure.

It has been previously mentioned that the SOT from the SHE has a direction parallel to $\hat{m} \times (\hat{m} \times (\hat{z} \times J_c))$, which corresponds to a situation in which there exists an effective magnetic field parallel to $\hat{m} \times (\hat{z} \times J_c)$. As J_c flows in the x-direction, this effective field is proportional to $\hat{m} \times \hat{y}$ (Fig. 1.12). Therefore, the finite *x*-component of $\hat{m}$ inside the DW generates the *z*-component of $\hat{m} \times \hat{y}$, that is, the perpendicular component of the SOT-induced effective magnetic field. With Néel type DWs, $\hat{m} = \pm 1$ and the effective field magnitude generated by SOT is maximized and saturated. With Bloch type DWs, $\hat{m} = 0$ and the effective field becomes zero. This explains why the DMI is so important for DW motion. Sufficiently large DMIs produce Néel type DWs with maximum spin torque, and the direction of magnetization is determined by the sign of the DMI for the same current direction, so that the effective field direction of SOT is determined, and the moving direction of DW is also determined.

The ε and H_{DMI} are measured from the depinning field of the DWs with respect to H_x, which is the in-plane external magnetic field along the current direction. There is a certain magnetic field that is required to produce depinning of the DWs, this is called the depinning field $H_Z^{\mathrm{dep.}}$. The $H_Z^{\mathrm{dep.}}$ is combined with the external magnetic field H_Z^{ext} and H_Z^{eff} by SOT from the electric current, that is, $H_Z^{\mathrm{dep.}} = H_Z^{\mathrm{ext}} + H_Z^{\mathrm{eff}}$. In this case, the required H_Z^{ext} will change according to H_Z^{eff} for the same $H_Z^{\mathrm{dep.}}$. By measuring H_Z^{ext} while changing the current, ε can be measured.

The measurement process is as follows: Firstly, a large perpendicular external magnetic field was applied to saturate the magnetization of the sample, in either spin up or spin down. Secondly, a DW was created at a position inside the microwire and adjacent to the DW writing electrode, as shown by the white vertical line in Fig. 1.14a. Finally, under application of a fixed current bias, the out-of-plane magnetic field was swept until the DW moved from the initial position. By repeating this procedure using different magnitudes of the current bias (Fig. 1.14b), the depinning field was measured as a function of the total current density, J. From the linear dependence of the perpendicular external field H_Z^{ext} on J, shown in Fig. 1.14c, we quantified ε using the relation $\varepsilon = -\partial H_Z^{ext}/\partial J = \partial H_Z^{eff}/\partial J$. The measurement was repeated for different H_x values.

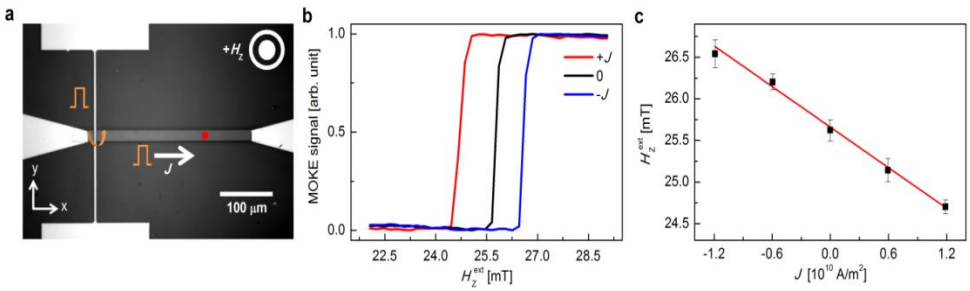

Figure 1.14 Measurement procedure of the spin torque efficiency. a. Depiction of field and current pulse in microwire. **b.** MOKE signal change when DWs pass through the laser spot. **c.** External magnetic field with respect to current density. The red line is the linear fitting line.

The plots of ε in Fig. 1.15 exhibit three distinct regimes that are frequently observed in SOT-induced DW motions: two saturation regimes of the Néel-type DW configurations and a transition regime in between. In the transition regime, a Bloch-type DW configuration appeared at the intercept to the abscissa (as shown by the orange vertical lines), in which the magnetic field H_{x}^{0} exactly compensates for H_{DMI} (i.e., $H_{\mathrm{x}}^{0} + H_{\mathrm{DMI}} = 0$). We could therefore quantify H_{DMI} from the intercept of the x-axis and the strength of the spin torque efficiency, ε_0, from saturation regions of the plot.

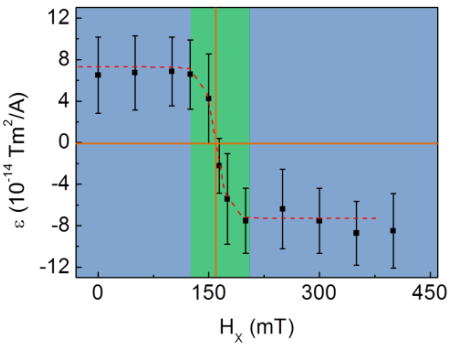

Figure 1.15 Typical spin torque efficiency plot. The horizontal orange line is the x-axis and the vertical orange line is at the position where $\varepsilon = 0$.

Chapter 2

Material dependence of the Dzyaloshinskii-Moriya interaction in trilayer structure

The mechanisms for DMI are introduced in Chapter 1, there are important physical phenomena or origins of each mechanism. However, phenomena affecting DMI are more likely to occur comprehensively, and it is difficult to accurately predict the magnitude and tendency of DMI experimentally from each physical theory, and the DMI strength also vary depending on the specific sample structure. In that sense, it is necessary to identify the change of DMI according to the change of each factor in the trilayer systems.

There may be three major factors that can change the conditions for DMI experimentally in the trilayer systems : First, use a various non-magnetic materials. Second, change the thickness of the ferromagnetic layer. Third, change the thickness of the non-magnetic layers. First of all, in this chapter, as a confirmation of the first factor, the results of research to find the parameters related to DMI by changing the materials but keeping the basic structure of the samples same are introduced. The next two chapters show the results of the second and third factors.

The results of this chapter may not be well understood in terms of atomic three-site super-exchange interactions, which are understood as Dzyaloshinskii and

Moriya's research. Besides, since the sample systems are metallic systems, conduction electron mediated spins interactions may have a significant effect.

2.1 Introduction

Chiral magnetic materials, the phenomena associated with them, and the technological opportunities provided by emerging spintronic devices [24,25] have recently attracted increasing academic attention. Such chiral magnetic phenomena are caused by DMI. In magnetic thin films, a sizeable DMI generates built-in chirality of magnetic DWs, which is essential for current-induced DW motion via SOTs [22,26]. The ultimate speed of the DW motion has been revealed to also be governed by the DMI strength [23]. In addition, a sizeable DMI is an essential ingredient for generating topological objects, such as magnetic skyrmions [27,28], which can be used in high-density digital devices for racetrack memory [24,25,27].

Because of the academic interest and technological importance, numerous efforts have been devoted to understanding the DMI and its role on magnetic phenomena. Nevertheless, the physical origin of the DMI at a metallic interface still remains elusive, so an experimental study of the key intrinsic parameters of the DMI will be of great help and can provide an empirical guideline in terms of both experiment and sample structure design for application and to help understand the DMI.

Therefore, we are interested in the DMI at interfaces between ferromagnetic metal and nonmagnetic metals in a bilayer system. The interfacial DMI in such

metallic bilayers arises from a three-site indirect exchange mechanism among two atomic spins and a neighboring atom with a large SOC [11,12,25]. In antiferromagnetic crystals, the DMI is known to originate from an anisotropic super-exchange interaction that linearly depends on the strength of the SOC [11]. In this case, the DMI magnitude is proportional to $(\Delta g/g)J_{\mathrm{ex}}$, where g is the gyromagnetic ratio, Δg is its deviation from the value of a free electron, and J_{ex} is related to the magnitude of the exchange interaction [11].

Whether associating this elegant picture to polycrystalline metallic systems is possible is an interesting question. Spin-glass alloy systems shed light on the origin of the DMI in metallic systems in which the DMI arises from the spin-orbit scattering of conducting electrons by nonmagnetic transition-metal impurities [12]. This condition inspired us to investigate the material parameters that may be correlated with *the scattering potential* at the metal–metal interface. If we can find a correlation between the DMI strength and other material parameters, such as the work function, electronegativity, and SOC constant, this would provide a productive guideline for engineering the DMI strength. In this paper, we report an experimental observation of the correlation between the DMI strength and the work function difference at the metal–metal interface.

2.2 Experimental details

The detailed film structure is 5 nm Ta/2.5 nm Pt/0.9 nm Co/2.5 nm X/1.5 nm Pt, where X was selected as Ti, Cu, W, Ta, Al, Ru, Pd, Au, or Pt, which was deposited

by dc-magnetron sputtering on Si wafers with a 300 nm SiO_2 layer. This structure was chosen to observe the relative DMI tendency of bilayer systems while keeping the bottom Pt layer and Co thickness the same. The lowermost Ta layer is a seed layer used to enhance the crystallinity of the films, and the uppermost Pt layer is a protective layer used to prevent oxidation. To keep the quality of the Pt/Co/X films as similar as possible and to exclude other unknown factors that affect the depinning field measurement, the sputtering conditions (Ar working pressure ~2 mTorr, sputtering power ~10 W) were carefully kept the same for all Pt/Co/X films. High-resolution transmission electron microscopy [29] revealed that the Pt layer has an fcc (111) crystalline structure along the growth direction [30], which is known to exhibit a strong PMA [4-6]. The overall film roughness, R, was measured via atomic force microscopy as listed in Table 2.1. No clear grain structure was observed, possibly due to the thin thickness of our films [30]. The depinning fields, H_P, are also listed in Table 2.1. These measurements confirm that there is no significant variation in both R and H_P among all the samples.

X	Ti	Cu	W	Ta	Al	Ru	Pd	Au	Pt
R [nm]	0.80	0.47	0.59	0.67	0.54	0.68	0.58	0.75	0.93
H_P [mT]	13.0 ± 0.2	17.5 ± 0.3	11.1 ± 0.2	13.6 ± 0.2	16.0 ± 0.7	10.8 ± 0.3	16.8 ± 0.4	13.8 ± 0.2	13.7 ± 0.2

Table 2.1 Film roughness R and domain wall depinning field H_P. Here, the film roughness, R, was obtained via the standard deviation of the surface height, and H_P was measured when J and H_x were zero.

2.3 Quantifying the H_{DMI} by measuring spin torque efficiency

To measure the SOT efficiency ε and the H_{DMI}, the samples were patterned to 20 μm-wide and 350 μm-long microwires by photolithography and an ion-milling process, as shown in Fig. 1.5. The H_{DMI} of each Pt/Co/X trilayers are measured by the method of spin torque efficiency measurement described in Chapter 1.

Fig. 2.1 shows the plot of ε with respect to H_x for the samples with different X values, as denoted in each panel. All the plots of ε exhibit three distinct regimes that are frequently observed in SOT-induced DW motions: two saturation regimes of the Néel-type DW configurations and a transition regime in between [31]. In the transition regime, a Bloch-type DW configuration appeared at the intercept to the abscissa (as shown by the red vertical lines) in which magnetic field H_x^0 exactly

compensated for H_{DMI} (i.e., $H_{\mathrm{x}}^{0} + H_{\mathrm{DMI}} = 0$). We could therefore quantify H_{DMI} from these measurements. All the samples with broken inversion symmetry exhibited non-zero H_{DMI}, except the sample with X = Pt, which had an almost zero H_{DMI} because of its symmetrically layered structure.

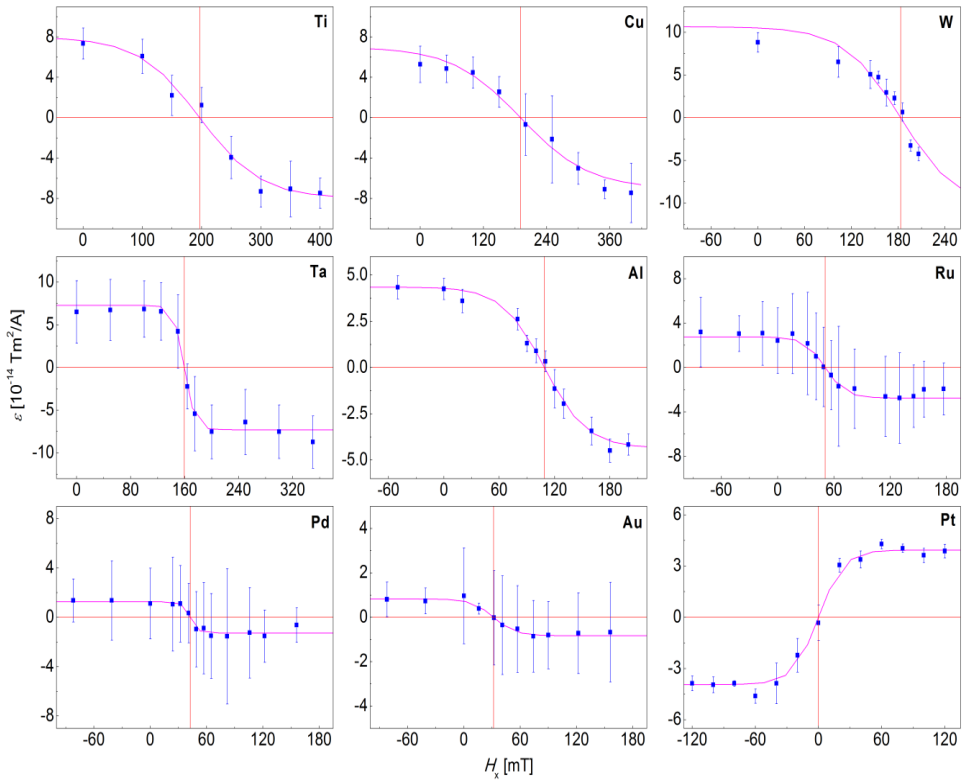

Figure 2.1 SOT efficiency of Pt/Co/X. Plots of ε with respect to H_{x} for different X values as denoted in the figures. The curved solid lines are best fits to guide the eye. The horizontal linear lines show the axis of $\varepsilon = 0$ for each measurement. The vertical linear lines indicate the positions of H_{x}^{0} for $\varepsilon = 0$.

The ε corresponds to the overall SOT efficiency with respect to J, where J is defined as the total current divided by the section of the wire. Since ε is composed of the contributions from the upper X and lower Pt layers, of which the local current densities are different to each other due to their different conductivities, there may be several other ways to define the current density [32]. However, a different definition of J changes only the scale of the ordinate in Fig. 2.1, whereas the intercept to the abscissa (i.e., H_{x}^{0}) can be uniquely determined. Of note, the DMI can be determined without current injection (i.e., no SOT phenomena) by purely field-induced DW motion or spin wave propagation [33,34].

2.4 Measurement of work function of material X via ultraviolet photoelectron spectroscopy

The work function of each material was measured by ultraviolet photoelectron spectroscopy (UPS). When ultra-violet light (21.2 eV for He light source) with a specific energy are injected into the metal, photoelectrons are released due to the photoelectric effect. Then, the electron that is separated from the metal by receiving the energy of light has kinetic energy (K.E.) except binding energy (B.E.), i.e. $\mathrm{K.E.} = E_{\mathrm{light}} - \mathrm{B.E.} = 21.2\ \mathrm{eV} - \mathrm{B.E.}$ The kinetic energy of electrons entering the detector are measured by electron energy analyzer.

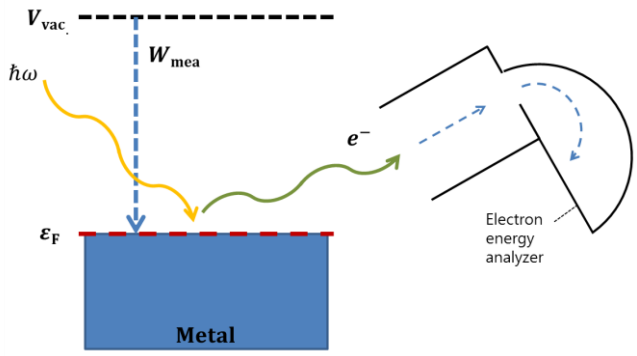

Figure 2.2 UPS measurement scheme. The $V_{\mathrm{vac.}}$ denoted vacuum state

The work function of the metal is obtained by the relation of $W_{\mathrm{mea}} = E_{\mathrm{light}} - (\varepsilon_{\mathrm{cut}} - \varepsilon_{\mathrm{F}})$, where the $\varepsilon_{\mathrm{cut}}$ is the cut-off edge at which the electrons reaching the detector start to be released, and the ε_{F} is the Fermi edge with the binding energy of zero, that is, the Fermi energy position.

The $\varepsilon_{\mathrm{cut}}$ and ε_{F} were obtained from the intersection of the bottom line and each linear fitting line in the increasing and decreasing regions. These are shown in an enlarged plots near the $\varepsilon_{\mathrm{cut}}$ and ε_{F} positions of Co in Figure 2.3. The measured work function W_{mea} of each material is compared with the W_{ref}, work function from the literature, as shown in Figure 2.4. In Fig. 2.4, the linear line has a slope of 1, and the symbols are placed linearly near this line, indicating that the measured work function values are similar to known values. The value of W_{mea} and W_{ref} are presented in Tables 2.2 and 2.3.

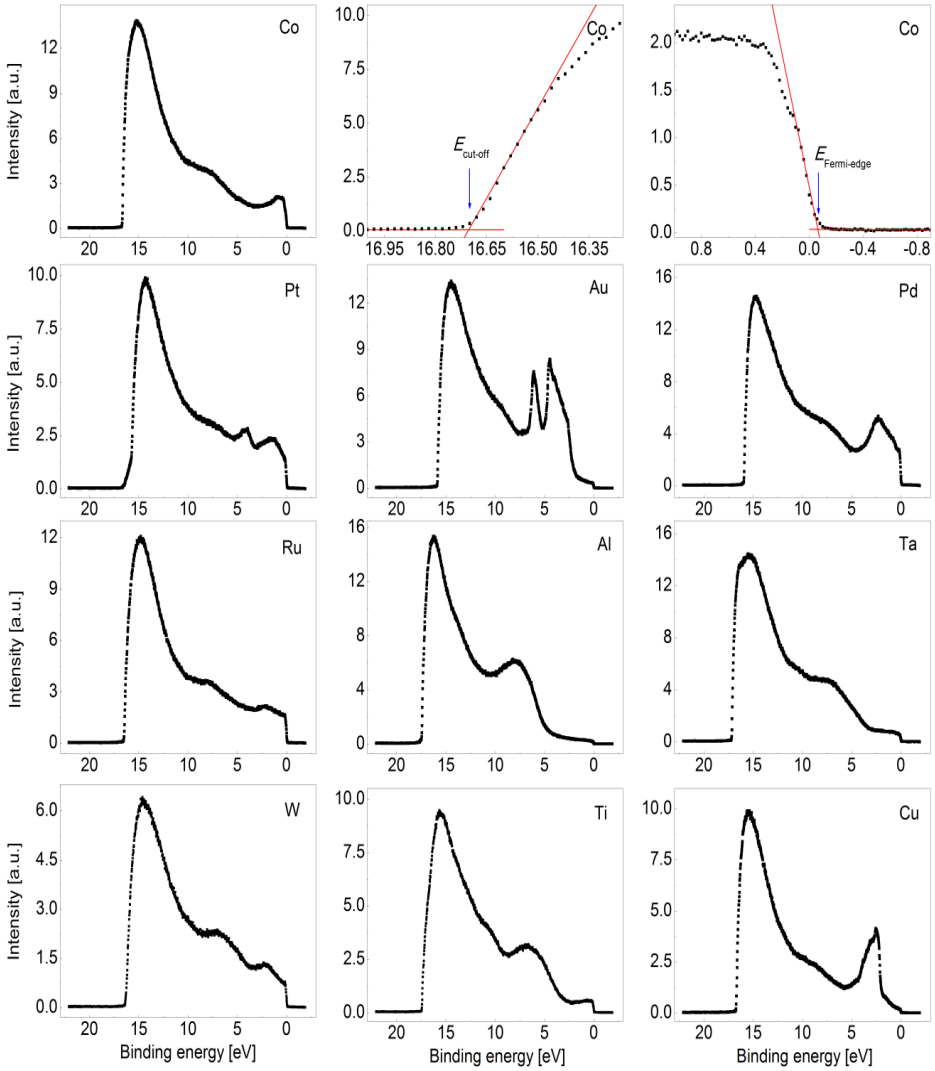

Figure 2.3 The UPS data of X. The UPS Intensity responds to the number of photoelectron arriving to the detector. Each material is denoted in each figure. In the figures of Co, the position of $E_{\mathrm{cut-off}}$ and $E_{\mathrm{Fermi-edge}}$ are shown. The red lines are linear fitting lines.

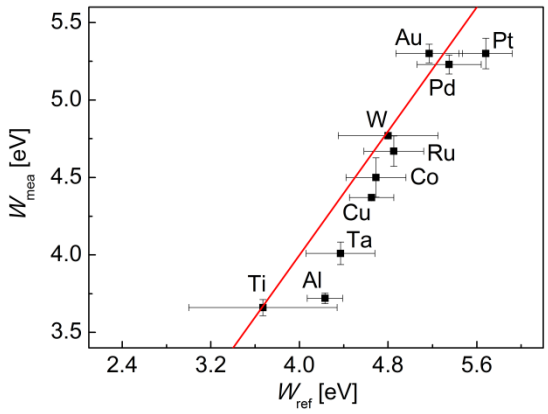

Figure 2.4 Comparison between W_{mea} and W_{ref}. The red linear line is drawn for eye guide, which slope is one. Each X is denoted near the symbols in the figure.

2.5 Comparison the H_{DMI} with material parameters

Tables 2.2 and 2.3 list the measured values of H_{DMI}, H_K, K_U^{eff}, D, W_{mea}, and the literature values of W_{ref}, electronegativity, χ, and SOC constant, ξ. These material parameters were chosen because of their potential relationship with the electrostatic potential barrier at the interface between the Co and X layers. In addition, the correlation between these easily accessible bulk values may be better as a practical guideline for the selection of the top and bottom nonmagnetic layers from the literature.

From the tables, we see that H_{DMI} has a better correlation with W than the other parameters. The correlations between W, χ, and ξ are plotted and shown in Fig. 2.5, where the W_{mea} values are denoted by red symbols and the W_{ref} values are black symbols, which confirm that a better correlation exists in Fig. 2.5a than in the other figures.

X	H_{DMI} [mT]	H_{K} [T]	$K_{\mathrm{U}}^{\mathrm{eff}}$ [10^5J/m^3]	D [mJ/m^2]	W_{mea} [eV]
Ti	-197 ± 25	1.13 ± 0.013	7.94 ± 0.09	-1.45 ± 0.18	3.66 ± 0.052
Cu	-190 ± 25	0.90 ± 0.021	6.28 ± 0.15	-1.58 ± 0.19	4.37 ± 0.007
W	-183 ± 5	0.95 ± 0.012	6.62 ± 0.08	-1.48 ± 0.03	4.77 ± 0.002
Ta	-160 ± 10	1.20 ± 0.018	8.37 ± 0.13	-1.15 ± 0.06	4.01 ± 0.073
Al	-109 ± 5	0.94 ± 0.049	6.61 ± 0.35	-0.88 ± 0.02	3.72 ± 0.034
Ru	-51 ± 4	0.65 ± 0.006	4.54 ± 0.04	-0.49 ± 0.04	4.67 ± 0.098
Pd	-43 ± 4	0.46 ± 0.006	3.24 ± 0.04	-0.49 ± 0.04	5.23 ± 0.034
Au	-32 ± 5	0.75 ± 0.006	5.22 ± 0.04	-0.29 ± 0.04	5.30 ± 0.061
Pt	0 ± 10	0.79 ± 0.010	5.51 ± 0.07	0.00 ± 0.09	5.30 ± 0.098

Table 2.2 Measured H_{DMI}, H_{K}, $K_{\mathrm{U}}^{\mathrm{eff}}$, D, and W_{mea} for the Pt/Co/X samples with material X. The W_{mea} of Co is 4.50 ± 0.127 eV.

X	W_{ref} [eV]	χ^{*} [Pauling]	ξ^{**} [10^4 m^{-1}]	References for W_{ref}
Ti	3.67 ± 0.67	1.5	1.2	38,44,57
Cu	4.65 ± 0.20	1.9	8.6	38,44,45,47,53,55
W	4.8 ± 0.45	2.4	24.3	38,41-44,47,52
Ta	4.37 ± 0.31	1.5	19.7	38-41,44,47,48
Al	4.23 ± 0.16	1.6	0.6	38,41,44,45,47,49,51,58
Ru	4.85 ± 0.27	2.2	10.4	38,44,47
Pd	5.35 ± 0.29	2.2	15.0	38,44,46,47,50
Au	5.17 ± 0.30	2.5	51.0	38,41,44,47,51,54,57
Pt	5.68 ± 0.24	2.5	44.8	38,44,47

Table 2.3 W_{ref}, χ (Pauling scale), and ξ for material X. The values and the error bars of W_{ref} were calculated as the means and standard deviations of values from Refs. [35-58]. The W_{ref} of Co is 4.69±0.27 eV [35-38,44]. Superscripts * and ** indicate relevant Refs. [59] and [60], respectively.

More specific and precise measurements would provide a more accurate relationship between the DMI and work function. Since the present W_{mea} was measured after in-situ surface cleaning on relatively thick X layers, there may be artefacts, such as crystal deformation, induced strain, and atomic mixing, which formed during the surface cleaning process. Additionally, since the X layers must be thicker than the penetration depth of the UPS measurement, accurate information at the vicinity of the interface might not have been precisely collected. Despite these experimental limits and possible artefacts, our observation suggests the possibility that the work function may play a more significant role in the generation of H_{DMI}.

Based on the concept of the potential gradient at the interface, the electronegativity may also have a relationship with the DMI, as shown in Fig. 2.5b, with a rough correlation between χ and H_{DMI}. Although the electronegativity difference between Co and X also implies a potential gradient at the interface, it is relevant to atomic and/or molecular systems but less relevant to metallic bilayer system because it is associated with the chemical energy of the valence bond. In addition, because the spin-orbit scattering-mediated spin-chiral effect may play a leading role in our trilayer system, our Pt/Co/X metallic system shows a better relationship between the DMI and work function compared with the DMI and electronegativity.

Another important factor in determining the strength of the DMI is the SOC. The D could be linearly proportional to the strength of the SOC, which is similar to that in antiferromagnetic crystals [11]. However, the experimental correlation between H_{DMI} and ξ was found to be pretty scattered, as shown in Fig. 2.5c. Because our values of ξ correspond to the atomic SOCs from the literature, if more specific and precise SOC values relevant to the metallic bilayer systems were available, we may possibly see a more accurate relationship between the DMI and SOC.

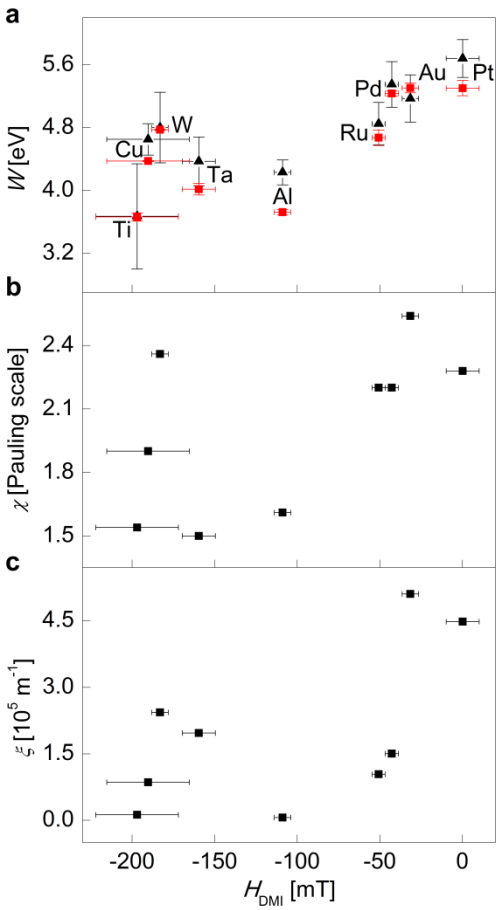

Figure 2.5 Parameter relationships with H_{DMI}. a. Work function, W, **b**. electronegativity, χ; and **c**. SOC constant, ξ, as functions of H_{DMI} for Pt/Co/X samples with different X values, as denoted in the figure. In each plot, W_{mea} (red square symbols) is the measurement work function, and W_{ref} (black triangle symbols), χ, and ξ are the literature values from Refs. [35–60]. The error bars for H_{DMI} correspond to the experimental accuracy determined from several repeated measurements. The error bars for W_{mea} and W_{ref} were obtained from measurement error and from the standard deviation of several different values from references.

2.6 The correlation between the strength of DMI and Work function

The magnitude of D was estimated from the relation of $D = \mu_0 H_{\mathrm{DMI}} M_{\mathrm{S}} \lambda$ with a Bloch-type DW width of λ $(= \sqrt{A/K_{\mathrm{U}}^{\mathrm{eff}}})$ [22,23,61], where A is the exchange stiffness. The Co value of A (2.2×10^{-11} J/m) and M_{S} of Co (1.4×10^{6} A/m) were used in the estimation for a qualitative comparison [3,61]. The effective anisotropy was quantified from the relation $K_{\mathrm{U}}^{\mathrm{eff}} = M_{\mathrm{S}} H_{\mathrm{K}}/2$. The D was defined as the total effective DMI, which includes contributions from the upper Pt/Co and lower Co/X interfaces. The scattering potential barrier was presumed to be associated with the work function difference, ΔW, at the Co/X interface. Fig. 2.6 shows a summary of the D values as a function of ΔW_{mea} $(\equiv W_{\mathrm{mea,X}} - W_{\mathrm{mea,Co}})$ and ΔW_{ref} $(\equiv W_{\mathrm{ref,X}} - W_{\mathrm{ref,Co}})$, where ΔW_{mea} values are denoted by red symbols measured via UPS and ΔW_{ref} values are shown as black symbols, which were obtained from the literature. The correlation between D and ΔW is better than between H_{DMI} and W.

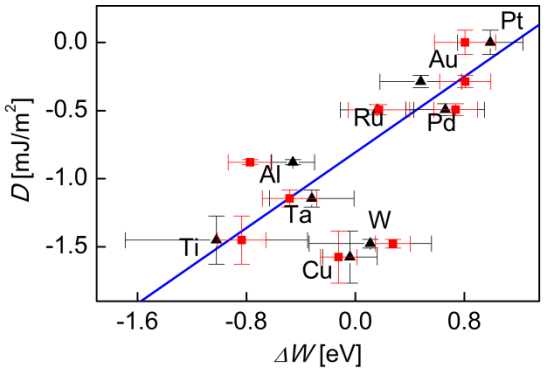

Figure 2.6 Plot of D as a function of ΔW for the Pt/Co/X samples with different X values. Each material is denoted near the symbols. The ΔW_{mea} values are denoted by red square symbols, and ΔW_{ref} values are shown by black triangle symbols. The linear line shows the best linear fit. The error bars for D were obtained from the statistical summation of the experimental accuracy of H_{DMI} and H_{K} determination. The error bars for W_{mea} are from measurement errors, and those for W_{ref} were obtained from the standard deviation of several different values from references.

2.7 Discussion

Ref.12 described how to calculate the magnitude of the DMI for non-magnetic transition-metal impurities (Ti, Ni, Pd, Fe, Co, and Pt) in CuMn spin-glass alloys. The DMI is associated with "the shift in the ground state energy of gas of conduction electrons interacting with two localized spins." [12], "On the site of nonmagnetic transition metal impurities, the spin-orbit coupling of a conduction electron is considerably enhanced because the admixture of the impurity *d* states into the conduction band allows the conduction electrons to experience the strong spin-

orbit forces of the *d* states." [12] They showed that the DMI is due to spin-orbit scattering of conduction electrons by non-magnetic impurities, and the strength of the DMI is proportional to the magnitude of the scattering potential [12]. In the FM/HM bi-layer systems, such as those in our experiments, the work function difference between the two metals provides such a scattering potential. When two metals with different work functions are brought into contact, the Fermi energy levels of two metals are aligned to build a very narrow potential barrier within the Thomas-Fermi length. The height of this potential barrier is proportional to the work function difference of the two metals. Consequently, the strength of the DMI may be related to the work function difference between two metals.

The signs of the DMI are all negative for the samples of the Pt/Co/X trilayer structure, except for X=Pt. The negative DMI generates left-handed chiral DWs [62]. For the case of X=Pt, a negligibly small DMI was expected due to its symmetric structure; however, several recent studies have reported a small but positive DMI, which is possibly due to the different interfaces that form between Pt/Co and Co/Pt [33,63]. Our observation of negative DMIs in the other samples is in agreement with other studies for the Pt/Co/Pd [64], Pt/Co/Al [65], Pt/Co/Cu [65], Pt/Co/Ta [66], Pt/Co/$[Ni/Co]_4$/Cu [32], and Pt/Co/$[Ni/Co]_4$/Ta [32] films after consideration of sign conventions. It is known that a strong SOC exists at the Pt/Co interface, and consequently, the DMI strength is very large at the Pt/Co bilayer interface [67,68]. From these results, we infer that the sign of the DMI may be determined in our trilayer samples by the underlayer Pt. Because our measurement is the sum of the effects on the DMI of the two interfaces, the effect of each interface cannot be

independently observed. Even if the underlayer Pt is dominant in the total DMI, directly knowing the sign and magnitude of the DMI at the Co/X bilayer interface is difficult. However, the relative strength of the DMI between the Pt/Co/X trilayers remains significant.

2.8 Conclusion

We presented experimental observations regarding the correlation between the DMI strength and the work function. This correlation may be related to the spin-orbit scattering in the electric potential barrier due to the work function difference at the interfaces. This correlation suggests that the DMI strength can be engineered via material selection following guidelines related to the intrinsic material parameters.

Chapter 3

Ferromagnetic layer thickness dependence of the Dzyaloshinskii-Moriya interaction in trilayer structure

This chapter is about the second way to change the conditions experimentally in trilayer systems : the result of the tendency of DMI by changing the thickness of the ferromagnetic layer. As a common picture for interfacial phenomena, there are two predictions about the magnitude of interfacial effects. First, the interface phenomenon is generated in the boundary where two different material layers meet. In this concept, it can be understood that materials that are not in direct contact may hardly affect the interfacial effects. Second, assuming that the magnetizations in each atomic layer in the direction perpendicular to the thin film inside the magnetic layer will all behave identically due to strong exchange interactions, the interfacial phenomenon generated at the interfaces is distributed to the entire magnetic layer. In this concept, the strength of the interfacial effects has inverse proportionality to the ferromagnetic layer thickness.

If these two predictions are correct, they will be negative in terms of application rather than physical in DMI, because there is little "degree of freedom" of DMI strength control. For the same ferromagnetic layer thickness, the non-magnetic materials adjacent to the ferromagnetic layer itself may entirely determine

the strength of the DMI. For the same non-magnetic materials, the only way to increase the DMI strength is to reduce the thickness of the ferromagnetic layer.

The results of the studies to identify the tendency of interfacial effects and overcome these shortcomings are introduced in Chapter 3 and 4. In this chapter, the peculiar tendency of DMI will be introduced by changing the thickness of the ferromagnetic layer with the non-magnetic layer materials fixed.

3.1 Introduction

The DMI has attracted much attention because of its peculiar properties for realizing chiral spin structures in magnetic systems with broken inversion symmetry. The interest in the DMI has exploded recently because of the discovery on huge DMIs at interfaces of magnetic multilayered systems [17,69,70]. By use of these systems, the interfacial DMI strength has been engineered to be strong enough to demonstrate magnetic skyrmions at room temperature [69]. Beyond the original concept based on atomic three-site anisotropic super-exchange interaction with spin-orbit coupling [10,11], recent studies have suggested more comprehensive mechanisms with different governing parameters such as the work function difference at the interface as presented in Chapter 2, orbital characteristics [17,67], charge distribution and interface dipole moment [20], and Rashba effect [13,14]. Although the most decisive parameters and mechanisms are still under debate, it is

commonly accepted that the interfacial DMI has to be generated by broken inversion symmetries at interfaces of heavy metals with large spin-orbit coupling [11,70].

Similar to other interfacial effects, it is commonly believed that the interfacial DMI arises at the interface itself and thus, its strength average over the ferromagnetic layer is inversely proportional to the layer thickness. Therefore, a system with a thinner layer is expected to show a larger DMI strength, as observed by recent studies [71-73]. Such monotonic dependence has been explained by H. Yang *et al.* [68] based on atomic-layer-resolved calculation of Pt/Co bilayers, by suggesting that the interfacial DMI is generated mostly at the first nearest Co atomic layer to the interface and thus, the DMI strength is inversely proportional to the layer thickness down to an atomic monolayer. Contrarily, another atomic-layer-resolved calculation by H. Jia *et al*. [74] has predicted a significant contribution of the second nearest Co atoms to the DMI in Pt/Co bilayers, resulting in a non-monotonic dependence of the DMI strength on the layer thickness. Both studies are in consensus that the interfacial phenomena originate from a few atomic layers near the interfaces, but the detailed contributions of each atomic layer to the DMI with the refined DMI mechanisms are still under debate.

In general cases, even at ideal interfaces with abrupt structural boundaries, the crossover between different material properties requires finite non-zero thickness, over which the interfacial phenomena are generated. Such crossover thickness might arise from the interactions between the conduction and orbital electrons with redistribution of charge and dipole moment or spin chiral mechanisms with the

Rashba effect, resulting in the off-nearest-site atomic interactions [74] beyond the original concept of atomic interactions between the nearest sites.

3.2 Experimental details

Two different series of films were prepared. The full layer stacks of the films are 1.5-nm Ta/3-nm Pt/t_{Co} Co/5-nm W/2-nm AlO_x with different t_{Co} in the range from 0.7 to 1.2 nm for the former Pt/Co/W films and 1.5-nm Ta/3-nm Pt/t_{Co} Co/0.6-nm Cu/5-nm W/2-nm AlO_X with different t_{Co} in the range from 0.3 to 0.8 nm for the latter Pt/Co/Cu/W films. All samples were deposited by dc-magnetron sputtering on Si wafers with a 100-nm-thick SiO_2 layer. The lowermost Ta and uppermost AlO_x layers are employed as seed and protection layers, respectively. The AlO_x layers are formed by natural oxidation after depositing Al layers. To keep the film quality as same as possible, the sputtering conditions were carefully maintained to be the same for all the films with an Ar working pressure ~2 mTorr, and sputtering power ~10 W. To measure ε_0 and H_{DMI}, 20 μm-wide and 350 μm-long microwires were patterned by photolithography and ion-milling processes. To inject electric current into the microwires, 5/100-nm-thick Cr/Au electrodes were deposited by lift-off process.

3.3 Observation of quick DMI decay with decrease of the Co layers thickness

To demonstrate the existence of finite thickness for DMI generation, we examined experimentally the DMI strength with respect to the Co layer thickness (t_{Co}). For this study, a series of Pt/Co/W films were prepared with different t_{Co}. The DMI strengths were then quantified by the measurement scheme as presented by Chapter 1 and 2 based on the variation of the ε in response to the in-plane magnetic field (H_x). Figure 3.1 plots the variation of ε with respect to H_x for the films with different t_{Co}. All the curves exhibit the same typical behaviour that ε is saturated to a value ε_0 (or $-\varepsilon_0$) in the large negative (or positive) H_x regime. The overall shape of the curves is antisymmetric, where the antisymmetric centre (black vertical line) indicates the magnitude of H_x for $\varepsilon = 0$. The antisymmetric centre corresponds to the strength of the H_{DMI}, at which the Bloch-type domain wall appears with compensation between H_x and H_{DMI} i.e. $H_x + H_{\mathrm{DMI}} = 0$ (see Chapter 1). The plots also provide the maximum SOT efficiency as the saturation value ε_0. Figure 3.2 summarizes the measured values of H_{DMI} (a) and ε_0 (b), respectively, with respect to t_{Co}.

Due to the interfacial nature, it is expected that both the strengths of the DMI and SOT increases as t_{Co} decreases via increment of the surface-to-volume ratio [62,71,72,75]. This expectation really happens for the case of the SOT, as seen by Fig. 3.2b, that ε_0 increases monotonically as t_{Co} decreases. However, interestingly, a quite distinct behavior happens for the case of the DMI. Figure 3.2a

shows that H_{DMI} quickly decays in the thinner t_{Co} regime, whereas the typical interfacial behaviour of inverse proportionality appears in the thicker t_{Co} regime. The critical thickness between these two regimes is found to be about 0.8 nm, where the maximum H_{DMI} strength is achieved.

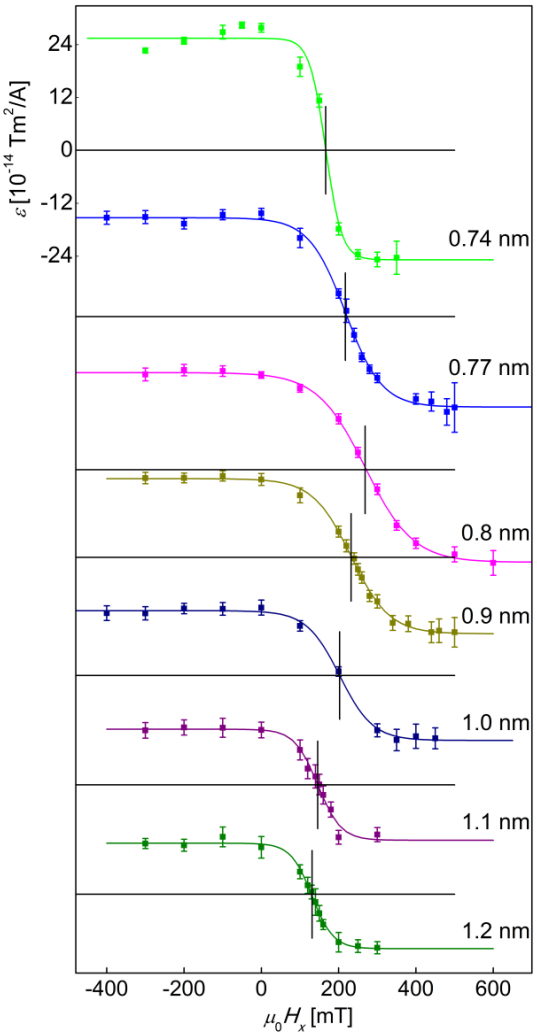

Figure 3.1 Plots of ε with respect to $\mu_0 H_x$ of Pt/Co/W trilayers. The t_{Co} are indicated in the figure. The vertical error bars are the standard deviation of ε measurement. The curved solid lines guide the eyes. The horizontal lines show the axis of $\varepsilon = 0$ for each measurement. The vertical lines indicate the positions of $\varepsilon = 0$, where $H_x + H_{\mathrm{DMI}} = 0$.

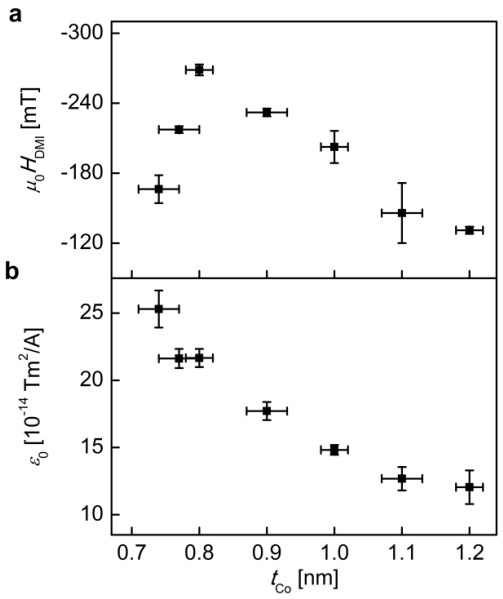

Figure 3.2 The H_{DMI} and ε_0 tendencies of the series of Pt/Co/W films. a, Plot of $\mu_0 H_{\mathrm{DMI}}$ with respect to t_{Co}. The horizontal error bar corresponds to the experimental accuracy of the Co-layer thickness, and the vertical error bar is the standard deviation of measurements. **b,** Plot of ε_0 with respect to t_{Co}. The horizontal and vertical error bars have the same meaning as those of (**a**).

3.4 Consideration on possible structural origins

We first examined structural imperfections as the possible origins of this peculiar behavior. Among the possible structural imperfections, the discontinuous island growth of the Co layer is not observed in our films, but rather continuous crystalline structure of the Co layer appear in a cross-sectional scanning transmission electron microscopy (STEM) as shown by Fig. 3.3a.

The cross-sectional image visualizes a continuous crystalline structure of the Co layer even for the thinnest case of the Co layer, signaling all the Co layers are expected to be continuous for this series of films. A closer look indicates reasonably clear atomic layer boundaries as visualized in Fig. 3.3b and thus, reduced number of atomic pairs at atomically misaligned interfaces is not likely the major origin of the quick H_{DMI} decay.

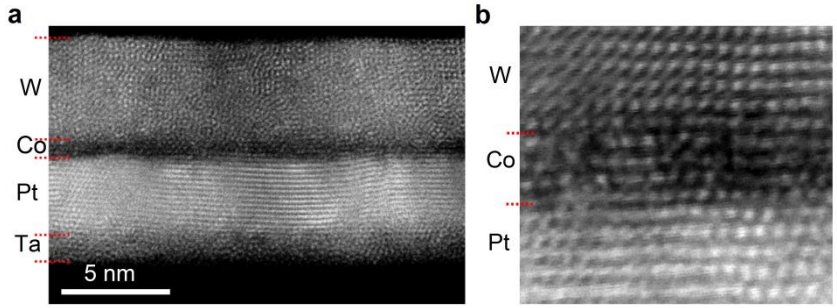

Figure 3.3 Cross-section of Pt/Co/W film observed by means of STEM. a, Wide range image of Pt/Co/W film with the thinnest Co layer ($t_{\mathrm{Co}} = 0.7$ nm). **b,** Image magnified on the Co layer and its interfaces. Each of the layers is denoted in the figure. The red dash lines are at layer boundaries.

Structural variation such as the coherent-to-incoherent transition of crystalline structures [1,2] is also examined by the measurement of the $K_{\mathrm{U}}^{\mathrm{eff}}$ with respect to t_{Co}. The measurement results in Fig. 3.4 indicate that the coherent-to-incoherent transition occurs at about $t_{\mathrm{Co}} \sim 1.2$ nm, which is far distinct from the critical thickness for the quick H_{DMI} decay. In addition, $K_{\mathrm{U}}^{\mathrm{eff}}$ exhibits a gradual thickness dependence dissimilar to the peculiar H_{DMI} variation. Hence, the coherent-to-

incoherent transition associated with the $K_{\mathrm{U}}^{\mathrm{eff}}$ variation is not likely to share the origin of the quick H_{DMI} decay.

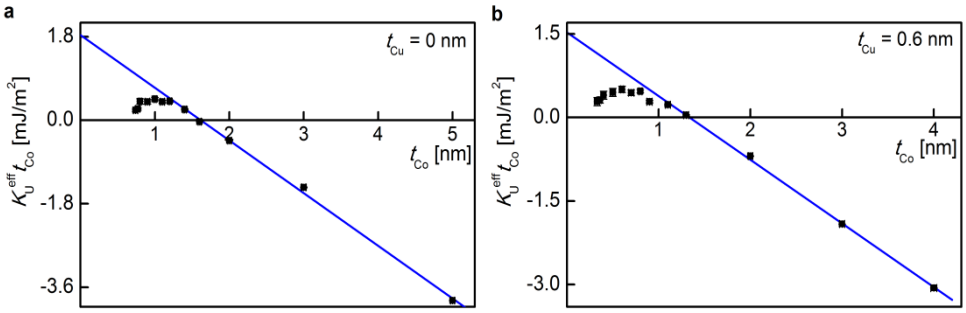

Figure 3.4 Plots of $K_{\mathrm{U}}^{\mathrm{eff}} t_{\mathrm{Co}}$ with respect to t_{Co} of Pt/Co/W and Pt/Co/Cu/W films. a, The plot of Pt/Co/W and **b,** Pt/Co/Cu/W. The blue line is linear fitting line. The data begin to deviate from the linear fitting line where $t_{\mathrm{Co}} \sim 1.2$ nm of Pt/Co/W and $t_{\mathrm{Co}} \sim 1.1$ nm of Pt/Co/Cu/W.

To check whether the quick H_{DMI} decay is possibly caused by reduction of the magnetically-effective thickness ($t_{\mathrm{Co}}^{\mathrm{m}}$) near the interfaces, we examined the reduced amount of $t_{\mathrm{Co}}^{\mathrm{m}}$ with respect to the deposited thickness t_{Co}. For this test, the M_{S} was measured by means of VSM. Figure 3.5a shows the results by plotting $M_{\mathrm{S}} t_{\mathrm{Co}}$ with respect to t_{Co}. The linear dependence between $M_{\mathrm{S}} t_{\mathrm{Co}}$ and t_{Co} manifests that all the films keep the same M_{S} irrespective of t_{Co}. Then, as guided by the blue linear line of the best fit, the non-zero x-intercept indicates the thickness of dead layer (δ), which is quantified about 0.44±0.05 nm. It is worthwhile to note

that δ is noticeably smaller than the critical thickness for the quick H_{DMI} decay, indicating that the mechanisms associated with the δ fomation is not directly responsible of the quick H_{DMI} decay.

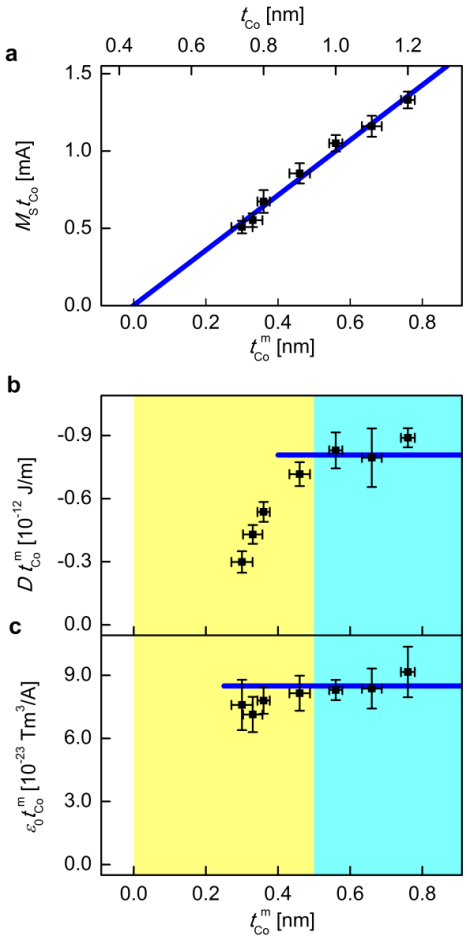

Figure 3.5 Co layer thickness dependence of the magnetic moment, DMI, and SOT for the series of Pt/Co/W. a, Plot of $M_S t_{Co}$ with respect to t_{Co} and t_{Co}^m. The blue line shows the linear fit. The x-intercept indicates δ. **b,** Plot of $D t_{Co}^m$ with respect to t_{Co}^m. The blue and yellow shaded areas show the thick and thin t_{Co} regimes. The blue horizontal line shows the average value over the thick t_{Co} regime. **c,** Plot of $\varepsilon_0 t_{Co}^m$ with respect to t_{Co}^m. The blue horizontal line shows the average value over both the regimes. In all the plots, the horizontal error bars are the experimental accuracy of the Co-layer thickness and the vertical error bars are calculated from the standard deviation of several repeated measurements.

3.5 Analysis with magnetically-effective thickness

To obtain detailed insights into the origin more quantitatively, the D is estimated by the relation $D = \mu_0 H_{\mathrm{DMI}} M_{\mathrm{S}} \lambda$. The measurement data of Pt/Co/W are summarized in Table 3.1. Here, M_{S} is measured by VSM and H_{K} is measured from magneto-resistance with respect to H_{in} (see Chapter 1). The $K_{\mathrm{U}}^{\mathrm{eff}}$ is estimated from the relation $K_{\mathrm{U}}^{\mathrm{eff}} = \frac{1}{2} M_{\mathrm{S}} H_{\mathrm{K}}$.

t_{Co} [nm]	M_{S} [MA/m]	$\mu_0 H_{\mathrm{K}}$ [T]	$K_{\mathrm{U}}^{\mathrm{eff}}$ [10^5 J/m^3]	$\mu_0 H_{\mathrm{DMI}}$ [mT]	D [mJ/m^2]	ε_0 [10^{-14} Tm^2/A]
0.74	0.69±0.03	0.84±0.03	2.90±0.22	-166±11.9	-1.00±0.07	25.3±1.4
0.77	0.72±0.03	0.88±0.02	3.16±0.22	-217±2.9	-1.30±0.03	21.6±0.7
0.8	0.84±0.07	1.20±0.03	5.06±0.60	-269±4.7	-1.49±0.06	21.7±0.7
0.9	0.95±0.04	0.93±0.03	4.42±0.35	-232±3.3	-1.56±0.03	17.7±0.7
1.0	1.05±0.03	0.87±0.02	4.56±0.27	-203±13.8	-1.48±0.10	14.8±0.4
1.1	1.06±0.04	0.68±0.01	3.61±0.18	-146±18.2	-1.20±0.16	12.7±0.9
1.2	1.11±0.03	0.61±0.01	3.41±0.15	-131±3.1	-1.17±0.03	12.1±1.2

Table 3.1 Measured magnetic properties of Pt/Co/W samples.

Then, D is analysed in terms of $t_{\mathrm{Co}}^{\mathrm{m}}$ $(= t_{\mathrm{Co}} - \delta)$. The inverse proportionality between D and $t_{\mathrm{Co}}^{\mathrm{m}}$ is examined by plotting $Dt_{\mathrm{Co}}^{\mathrm{m}}$ with respect to $t_{\mathrm{Co}}^{\mathrm{m}}$ as shown by Fig. 3.5b. This scaled plot is useful to decompose the surface contribution (D_{S}) and the volume contribution (D_{V}) via the relation $Dt_{\mathrm{Co}}^{\mathrm{m}} = D_{\mathrm{S}} + D_{\mathrm{V}} t_{\mathrm{Co}}^{\mathrm{m}}$. It is interesting to see that the plot again exhibits two different regimes. In the thicker $t_{\mathrm{Co}}^{\mathrm{m}}$ regime (blue area), $Dt_{\mathrm{Co}}^{\mathrm{m}}$ shows negligible variation with respect to $t_{\mathrm{Co}}^{\mathrm{m}}$, indicating that D has negligible volume contribution i.e. $D_{\mathrm{V}} \cong 0$ and therefore, the surface contribution is mostly responsible for the DMI i.e. $Dt_{\mathrm{Co}}^{\mathrm{m}} \cong D_{\mathrm{S}}$. In addition, the saturation values of $Dt_{\mathrm{Co}}^{\mathrm{m}}$ manifest that D_{S} is fully generated in this regime, resulting in the inverse proportionality between D and $t_{\mathrm{Co}}^{\mathrm{m}}$.

On the other hand, in the thinner $t_{\mathrm{Co}}^{\mathrm{m}}$ regime (yellow area), $Dt_{\mathrm{Co}}^{\mathrm{m}}$ becomes smaller than the saturation value. The critical thickness between these two regimes is about 0.4 to 0.5 nm (≅ 2 to 2.5 atomic layers), which is consistent with the prediction based on the atomic-layer-resolved calculation by H. Jia *et al.* [74] It is also worthwhile to note that the other atomic-layer-resolved calculation by H. Yang *et al.* [68] can be extended to explain such insufficient DMI generation for the case of incomplete atomic interface formation with large vacancies - the detail discussion about this is in chapter 3.8 - though this case is not likely for our films with reasonably clear atomic layer boundaries as shown by Fig. 3.5b. It is not easy to quantify the exact contributions of these mechanisms, but both cases suggest that incomplete generation of the interfacial DMI might be a possible origin of the quick DMI decay in the thinner regime.

The distinct thickness dependences of the DMI and SOT provide another hint to understand the interfacial and bulk phenomena and also, possibility of independent engineering of the DMI and SOT. In contrast to the DMI that should be generated near the interfaces, the SOT is known to have two sources; at the interfaces via the Rashba effect [76] and from the adjacent nonmagnetic layers via the spin-Hall effect [21,62]. The plot of $\varepsilon_0 t_{\mathrm{Co}}^{\mathrm{m}}$ with respect to $t_{\mathrm{Co}}^{\mathrm{m}}$ (Fig. 3.5c) manifests that $\varepsilon_0 t_{\mathrm{Co}}^{\mathrm{m}}$ remains unchanged over the whole thickness range. This observation indicates that the SOT is less sensitive to interface formation and thus, the SOT originates mainly from the spin-Hall current from the outer nonmagnetic layers in these films. Unlike the SOT, the DMI is sensitive to the thickness of the atomic layers at vicinity of the interface, indicating that the quick DMI decay might be attributed not only to the interface characteristics but also to the incomplete DMI generation with Co layers thinner than the critical thickness.

3.6 Confirmation with other series films without reduction of magnetically-effective thickness

To avoid any possible artefact associated to the mechanisms of the $t_{\mathrm{Co}}^{\mathrm{m}}$ reduction, another series of films with Pt/Co/Cu/W stack was prepared with different t_{Co}. In these films, Cu layer (0.6 nm) was inserted at the Co/W interface to suppress intermixing between Co and W atoms [77]. The same typical ε variation with respect to H_x was observed from this series of films as shown by Fig. 3.6, and the

measurement data of Pt/Co/Cu/W are summarized in Table 3.2. The measurement methods are same as Pt/Co/W samples.

t_{Co} [nm]	M_S [MA/m]	$\mu_0 H_K$ [T]	K_U^{eff} [10^5 J/m^3]	$\mu_0 H_{DMI}$ [mT]	D [mJ/m^2]	ε_0 [10^{-14} Tm^2/A]
0.33	1.36±0.10	1.27±0.11	0.87±0.14	-146±1.3	-1.00±0.01	17.8±0.8
0.36	1.34±0.07	1.29±0.10	0.87±0.12	-234±3.6	-1.58±0.01	17.5±0.7
0.4	1.40±0.09	1.43±0.10	1.00±0.14	-335±4.7	-2.20±0.01	15.7±1.6
0.5	1.31±0.09	1.37±0.04	0.90±0.09	-301±10.4	-1.95±0.10	13.9±0.4
0.6	1.36±0.07	1.24±0.03	0.84±0.07	-209±6.2	-1.45±0.06	11.0±0.3
0.7	1.33±0.06	0.95±0.02	0.63±0.04	-192±9.0	-1.50±0.09	10.3±0.3
0.8	1.33±0.04	0.89±0.01	0.59±0.02	-158±1.5	-1.28±0.02	9.1±0.1

Table 3.2 Measured magnetic properties of Pt/Co/Cu/W samples.

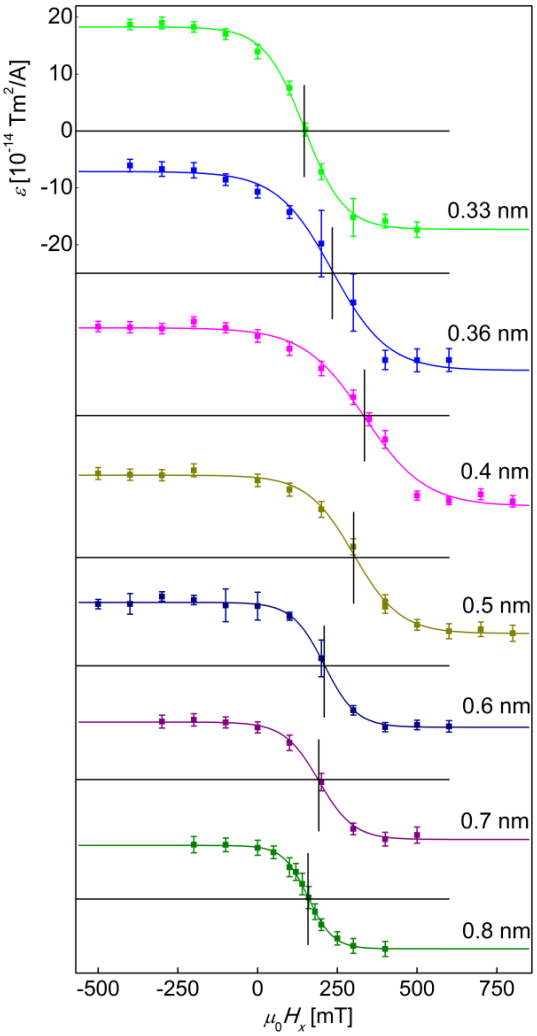

Figure 3.6 Plots of ε with respect to $\mu_0 H_x$ of Pt/Co/Cu/W trilayers. The t_{Co} are indicated in the figure. The vertical error bars are the standard deviation of ε measurement. The curved solid lines guide the eyes. The horizontal lines show the axis of $\varepsilon = 0$ for each measurement. The vertical lines indicate the positions of $\varepsilon = 0$, where $H_x + H_{\mathrm{DMI}} = 0$.

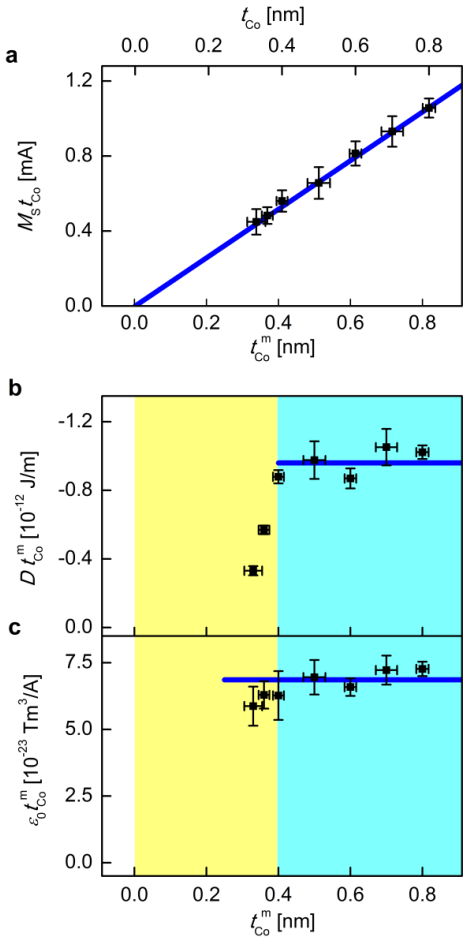

Figure 3.7 Co layer thickness dependence of the magnetic moment, DMI, and SOT for the series of Pt/Co/Cu/W. a, Plot of $M_S t_{Co}$ with respect to t_{Co} and t_{Co}^m. The blue line shows the linear fit. The x-intercept indicates δ. **b,** Plot of $D t_{Co}^m$ with respect to t_{Co}^m. The blue and yellow shaded areas show the thick and thin t_{Co} regimes. The blue horizontal line shows the average value over the thick t_{Co} regime. **c,** Plot of $\varepsilon_0 t_{Co}^m$ with respect to t_{Co}^m. The blue horizontal line shows the average value over both the regimes. In all the plots, the horizontal error bars are the experimental accuracy of the Co-layer thickness and the vertical error bars are calculated from the standard deviation of several repeated measurements.

Figure 3.7a shows a plot of $M_S t_{Co}$ with respect to t_{Co} for this series of films. It is noteworthy that the x-intercept of the linear fit passes close to the origin, indicating that δ is negligibly small and thus, $t_{Co}^{m} \cong t_{Co}$ in these films. Due to the negligibly small δ, this series of films keeps strong perpendicular magnetic anisotropy even for the films with the thinnest t_{Co} down to about 1.5 atomic monolayers. Then, the DMI and SOT are quantified by repeating the same analysis on the data in Fig. 3.6 as done for the former series of films. The results are plotted in Figs. 3.7b and c, respectively, with respect to t_{Co}^{m}. Interestingly, the figures again reproduce the distinct thickness dependence between the DMI and SOT: the interfacial DMI drops quickly in the thinner t_{Co}^{m} regime below 0.4 nm, whereas the SOT remains unchanged over the whole t_{Co}^{m} range. From the same behaviors for both the cases with and without the t_{Co}^{m} reduction, these observations confirm that the peculiar thickness dependence of DMI is not associated to the mechanisms of the t_{Co}^{m} reduction.

3.7 Conclusions

Here, we demonstrate the existence of a finite thickness for full DMI generation at interfaces, from two different series of films Pt/Co/W and Pt/Co/Cu/W with various Co layer thickness. Both the series of films exhibit the same behaviour of quick DMI decay with decrease of the ferromagnetic layer thickness below a threshold thickness. Such quick DMI decay has to be caused by insufficient DMI

generation at interfaces with ferromagnetic layers thinner than the threshold. Therefore, full emergence of the interfacial DMI requires a finite threshold thickness, in contrast to the commonly accepted naïve concept that the interfacial phenomena is generated exactly at the interfaces. Interesting, both the series of films provide the same threshold thickness about 2 to 2.5 atomic layers, signaling a possibility of common key mechanisms for the DMI generation. These results provide a technological criteria to optimize the DMI strength with maximum at the threshold thickness. In addition, the distinct behaviors between the DMI and SOT manifest that the DMI is generated at the vicinity of the interface, whereas the SOT is generated mainly by the spin-Hall current from outer nonmagnetic layers in our series of films. These distinct behaviors provide the perspective of a systematic study on the interfacial DMI and bulk SOT phenomena, providing a way of independent tuning of the DMI and SOT for spintronic applications.

3.8 Theoretical estimation of the DMI tendency when the vacancies in ferromagnet layer are formed during sputtering process

In Ref.68, it is reported that the DMI at the interface of a Co/Pt bilayer mainly originates from the first nearest atomic layer of Co adjacent to the Pt layer. Based on this observation, it is argued that the averaged DMI in the Co layer is inversely proportional to the number of magnetic layers. In other words, $D \propto 1/t_{\mathrm{Co}}$.

However, this argument is valid only for t_{Co} larger than the thickness of a single atomic layer. The purpose of this note is to examine how the argument is altered when t_{Co} is comparable with a single atomic layer in experimental conditions.

The problem with the previous abstraction is that the DMI diverges as $t_{\mathrm{Co}} \to 0$, which is unphysical. Before constructing a mathematical formalism, we illustrate how the unphysical conclusion can be altered. In reality, the thickness of a sample made by sputtering cannot be perfectly uniform. Although this is not so important for thick films as illustrated in Fig. 3.8a, this fluctuation can reduce the number of Co atoms adjacent to the Pt layer and thus, reduce the total DMI for thin films whose thickness is on the order of d as shown in Fig. 3.8b, where d is the thickness of a Co monolayer. Furthermore, for $t_{\mathrm{Co}} < d$ shown in Fig. 3.8c, most atoms are adjacent to the Pt layer. Thus, the total DMI contribution decreases as t_{Co} decreases below d. There is another effect. In Fig. 3.8c, the isolated spin near the vacancy cannot contribute to the DMI due to the sharply decreasing atomic exchange interaction for the next nearest neighbours. As the density of the Co atoms in the first atomic layer goes to zero, the average number of nearest neighbours decrease, thus the DMI eventually goes to zero. In this sense, the DMI value as a function of thickness should satisfy the following: $D \propto 1/t_{\mathrm{Co}}$ for $t_{\mathrm{Co}} \gg d$ while $D(t_{\mathrm{Co}}) \to 0$ as $t_{\mathrm{Co}} \to 0$.

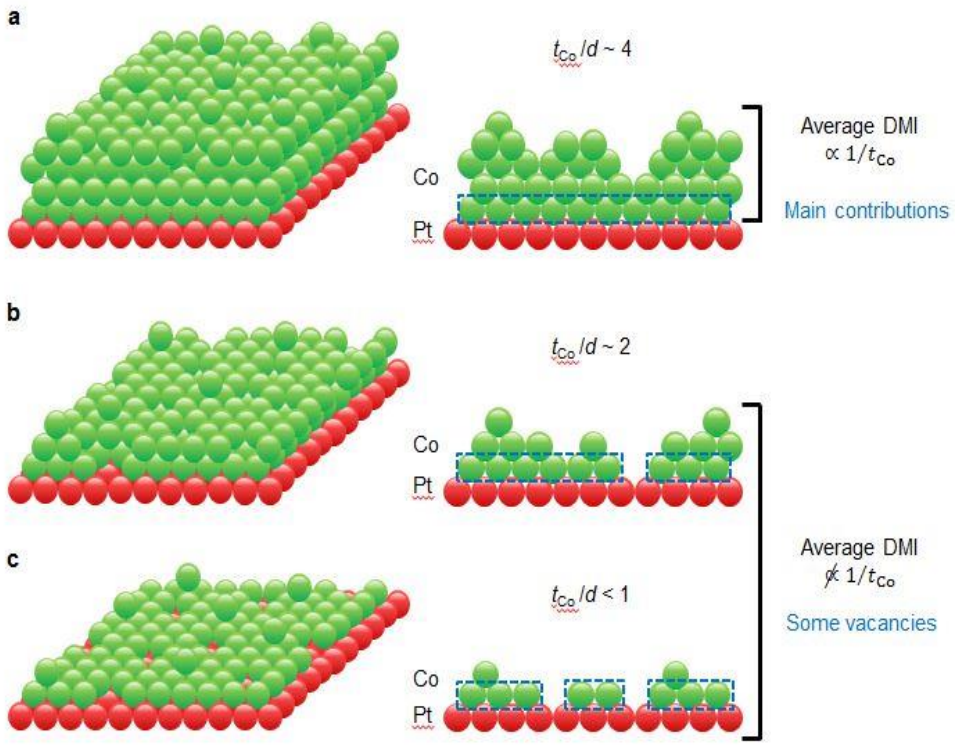

Figure 3.8 Illustration of Co atomic layer deposition on Pt atomic layer. The Co atoms adjacent to the Pt layer are enclosed by a dashed blue rectangle, which might provide major contribution on the DMI. **a,** The Co layer adjacent to the Pt layer has no vacancies, and the average DMI is inversely proportional to t_{Co}. **b,** There are some vacancies in the Co layer, and the average DMI deviates from the inverse proportionality. **c,** More vacancies are formed in more thinner Co layers. Due to the vacancies this thinner Co layer, the strength of the DMI may decrease significantly, despite formation of an obvious layer of Co islands not occurring, as shown in the left image in (**c**).

To mathematically formulate the idea, we denote the number of Co atoms adjacent to the Pt layer by N_{D}, the total number of Co atoms by N_{tot}, and the number of sites of Co atoms *in the plane* by n_{site}. We also denote the DMI

contribution coming from a Co atom adjacent to the Pt layer by D_0. Thus, the averaged DMI strength of the Co layer is given by

$$D = D_0 \times \frac{N_{\mathrm{D}}}{N_{\mathrm{tot}}} \times \frac{N_{\mathrm{D}}}{n_{\mathrm{site}}}.$$

(E1a)

The first factor $N_{\mathrm{D}}/N_{\mathrm{tot}}$ is introduced for averaging the DMI in the same sense as Ref.68. The second factor $N_{\mathrm{D}}/n_{\mathrm{site}}$ is introduced to allow for the reduction of the number of nearest neighbour atoms in the first atomic Co layer. Consideration of *both* factors is crucial to ensure a rapid drop of the DMI for $t_{\mathrm{Co}} \to 0$. Note that $N_{\mathrm{tot}}/n_{\mathrm{site}}$ gives the number of atomic Co layers, that is, t_{Co}/d. Therefore, we obtain

$$D = \frac{D_0 d}{t_{\mathrm{Co}}} \times \left(\frac{N_{\mathrm{D}}}{n_{\mathrm{site}}}\right)^2.$$

(E1b)

For $t_{\mathrm{Co}} \gg d$, the nearest Co layer is mostly occupied $N_{\mathrm{D}} \approx n_{\mathrm{site}}$ thus $D \propto 1/t_{\mathrm{Co}}$. However, if $t_{\mathrm{Co}} \lesssim d$, N_{D} can be smaller than n_{site} and dependent on t_{Co}. To calculate $N_{\mathrm{D}}/n_{\mathrm{site}}$ for a thin film, it is important to find the number of 'vacancies' $(n_{\mathrm{site}} - N_{\mathrm{D}})$. In Fig. 3.8b, one position has no Co atoms; thus, this position does not contribute to the DMI. The mathematical expression for the number of vacancies depends on the nature of the sputtering process. During the

sputtering process, a Co atom arrives at a specific position out of the n_{site} position. In our theory, we assume all positions have equal probability $1/n_{\mathrm{site}}$ that an atom arrive on a certain atomic position for simplicity. We consider a specific position i out of n_{site} sites. When a Co atom reaches the interface, the probability of it not selecting the position $(n_{\mathrm{site}}-1)/n_{\mathrm{site}}$. After the whole sputtering process for N_{tot} Co atoms, the position i has a probability $[(n_{\mathrm{site}}-1)/n_{\mathrm{site}}]^{N_{\mathrm{tot}}}$ of remaining vacant. As a result, we obtain the average number of vacancies as given by

$$n_{\mathrm{site}} - N_{\mathrm{D}} = n_{\mathrm{site}}\left[\frac{(n_{\mathrm{site}}-1)}{n_{\mathrm{site}}}\right]^{N_{\mathrm{tot}}} \approx n_{\mathrm{site}} e^{-t_{\mathrm{Co}}/d},$$

(E2)

where we used $(1-1/n_{\mathrm{site}})^{n_{\mathrm{site}}} \approx e^{-1}$ for $n_{\mathrm{site}} \gg 1$. From the above equation, we obtain $N_{\mathrm{D}}/n_{\mathrm{site}}$ thus Eq. (E1b) gives

$$D = \frac{D_0 d}{t_{\mathrm{Co}}} \times \left(1 - e^{-t_{\mathrm{Co}}/d}\right)^2,$$

(E3)

which is the final result of this model. The D and Dt_{Co} with respect to t_{Co}/d are shown in Fig. 3.9. From Eq. (E3), we observe that Dt_{Co} is quadratically increasing with thinner t_{Co} and becomes flat for thicker t_{Co}, and that D has maximum strength. The qualitative features in Fig. 3.9 from this simple theory match well with the experimental results.

In addition, although the qualitative tendency of the described model match well, the quantitative values of Co thickness where Dt_{Co} is saturated and D is maximized may be different. It may come from simplicity of the model, or the difference between assumption in the model and real situation. For example, in the case of very thin Co atomic layers deposited on the Pt layer, the layer-by-layer growth which is preferred to fill vacancies rather than to form islands of Co clusters, may dominate [78]. If so, the Co thickness where the Dt_{Co} is saturated can be different with the estimated value from the model. Moreover, if the effects such as the contribution to the DMI from the second or subsequent layers in non-magnetic layers from the interface are considered as shown in Ref.74, the critical thickness of Co for the DMI drop or maximum may be changed. To quantify our results more accurately, detail theoretical work for our results will be required with consideration of real situation during deposition.

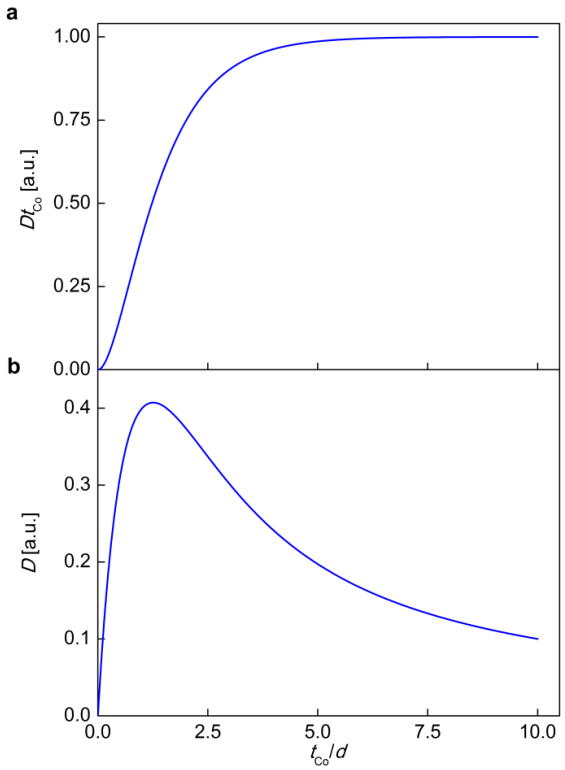

Figure 3.9 Plots of Dt_{Co} and D with respect to t_{Co}/d. The plots of **a,** Dt_{Co} and **b,** D with respect to t_{Co}/d from Eq. (S3). In (**a**), the plot is nearly saturated where $t_{\mathrm{Co}} \gtrsim 3d$. In (**b**), the plot have maximum strength where $t_{\mathrm{Co}} \approx 1.3d$.

As a side remark, if the average factor $N_{\mathrm{D}}/N_{\mathrm{tot}}$ is only considered neglecting the coverage factor $N_{\mathrm{D}}/n_{\mathrm{site}}$, D becomes proportional to the $\left(1-\exp(-t_{\mathrm{Co}}/d)\right)/t_{\mathrm{Co}}$. From this, $Dt_{\mathrm{Co}} \propto \left(1-\exp(-t_{\mathrm{Co}}/d)\right)$ reproduces the tendency as can be seen in Fig. 3.7a, but $D \propto \left(1-\exp(-t_{\mathrm{Co}}/d)\right)/t_{\mathrm{Co}}$ does not exhibit the decay of D. Therefore, to have maximum D at a certain value of t_{Co}, both the average factor and the coverage factor should be considered.

The present model is easily applicable to the series of Pt/Co/Cu/W films with thin Co layers down to approximately 1.5 monolayers. However, applying the present model to the other series of Pt/Co/W films requires more considerations, since the Co layers in this series films are continuous as seen by Fig. 3.3. Even for the continuous Co layers, one has to consider that the W atoms are known to severely alter the magnetic properties of the Co atoms nearby them, causing the reduction of Curie temperature [79,80] and also, the reduction of magnetically-effective thickness. Therefore, for the case that the Co atoms nearby the W atoms behave paramagnetic below their Curie temperature, the effective N_{D} might be possibly reduced at the Pt/Co interfaces as the Co layer thickness decreases. Then, the behaviour similar to the series of Pt/Co/Cu/W films might appear in the series of Pt/Co/W films. The present model together with the atomic-layer-resolved calculation by H. Jia *et al*. [74] thus predicts the existence of the finite threshold thickness of full DMI emergence, but quantification of the exact contributions requires further refined understanding on each mechanism.

Chapter 4

Non-magnetic layer thickness dependence of the Dzyaloshinskii-Moriya interaction in trilayer structure

This chapter describes a third method of changing the experimental conditions in trilayer systems, and the resulting tendencies of the DMI, by changing the thickness of the non-magnetic layer. The common perspectives of interfacial phenomena were introduced in the previous chapter, and the results of our attempts to identify interfacial effects and overcome the limit will also be introduced in this chapter.

In this study, in order to maximize the effects of the conduction electron-mediated spins interaction on the DMI, copper is used as the upper non-magnetic layer material. Copper is known to have a spin diffusion length of approximately 500 nm, so the spin information may not be well dissipated in layers of thinner Cu thickness.

4.1 Introduction

The DMI was first established and described in bulk antiferromagnetic oxide systems, with weak ferromagnetism through spin tilting [10,11]. Recently, it has been reported that DMI-generated peculiar spin chiral structures, such as magnetic skyrmions, were found in multilayer systems with broken inversion symmetry

[25,27,69]. For these layered systems, the DMI's have typically been understood as interfacial phenomenon [70], because the original mechanism was based on an anisotropic super-exchange interaction in atomic three-sites with SOC [11]. As our understanding of DMI has developed, recent studies have suggested more comprehensive mechanisms, which show that the conduction electrons-mediated phenomena in metallic layered systems may affect the DMI [12-14].

These suggested mechanisms provide possible new directions for DMI engineering, including a better understanding of the DMI, and the possibility that the DMI is a relatively long-range interaction [74]. If the DMI is understood and manifested simply as an interfacial effect, there will be a limited number of ways to increase its strength because the strength of the DMI can be determined only by the properties of the materials that form the interface, and there are only two interfaces adjacent to the ferromagnetic layer. In addition, as it is known that the DMI strength is related to the spin-orbit coupling parameter [11], and material searches mainly focus on certain heavy metals [60,81].

To overcome these limits, a study was conducted to enhance understanding of the DMI in metallic layered systems, and to find new controllability beyond that of interface engineering, based on the fact that the DMI will be affected by conduction electron-mediated effects. In quantum well (QW) structures with a ferromagnetic layer and spacer, it has been shown that the electrical and magnetic phenomena are strongly correlated with the QW characteristics [82,83], and even the parameters that can be understood by magnetic volume contribution were changed by the QW

characteristics [84,85]. Therefore, it is necessary to question and confirm whether these phenomena will also be affected, particularly for metallic layered systems.

For this, we conducted our measurements of the DMI in a QW state, using a Cu layer. It is expected that the loss of spin information may be relatively small in the thin Cu layer because the Cu is known to have a long spin diffusion length [86]. Furthermore, the use of Cu has benefits for the precise analysis of the DMI change because it has been shown that with a Cu upper layer, there is no dead layer [3] which would introduce uncertainty into the precise analyses of the DMI's strength because the DMI is also related to the ferromagnetic layer thickness [71,72].

4.2 Experimental details

The stacks of films fabricated for the experiment were 1.5-nm Ta/5-nm Pt/0.5-nm Co/t_{Cu} Cu/2.5-nm AlO_x/2-nm Ta. Here, the Cu thickness, t_{Cu} varied from 0.2 nm to 3.6 nm, with 0.2 nm increments. All samples were deposited on Si wafers with a 300-nm-thick SiO_2 layer. The lowermost Ta was employed as seed layer, and the AlO_x layer was fabricated by plasma oxidation and used as a reflection layer placed at the opposite site of the Co layer. Therefore, the Cu layer was sandwiched between Co and AlO_x. The uppermost Ta was a capping layer.

4.3 Variation of basic magnetic parameters with respect to Cu thickness

We estimated the M_S from the easy-axis hysteresis loop measured by VSM. The measured data are shown in Figures 4.1a and b, and the PMA of all samples were confirmed. Each Cu thickness is denoted in the figure by a different color. The M_S was estimated from the saturation region of the loop, and the obtained values are summarized in Table 4.1. The H_K are obtained through measurement of MR by AHE, as detailed in Chapter 1 [7,8]. The measured, normalized MR data with respect to H_{in} are shown in Fig. 4.1b, with fitting curves. The K_U^{eff} is obtained from M_S and H_K, H_K and K_U^{eff} are also summarized in Table 4.1.

Figs. 4.2a and b show M_S and K_U^{eff}, respectively. Both M_S and K_U^{eff} increase with t_{Cu} when smaller than approximately 0.6 nm, and seem to saturate with little fluctuation when the t_{Cu} is larger than approximately 0.8 nm (Figs. 4.2a and b). To check whether the dead layer of Co was formed in the range $0.2\ \text{nm} \leq t_{Cu} \leq 0.8\ \text{nm}$, the $M_S t_{Co} - t_{Co}$ plots of Cu 0.2 and 0.8 nm were obtained, where t_{Co} is the Co thickness. As shown in Fig. 4.2c, the linear fitting lines of Cu 0.2 nm and 0.8 nm pass through the origin of the plot, which means there are no dead layers in the samples. These are only the results of two Cu thickness cases, but it would not be unreasonable to infer that there are no dead layers for the entire Cu thickness range.

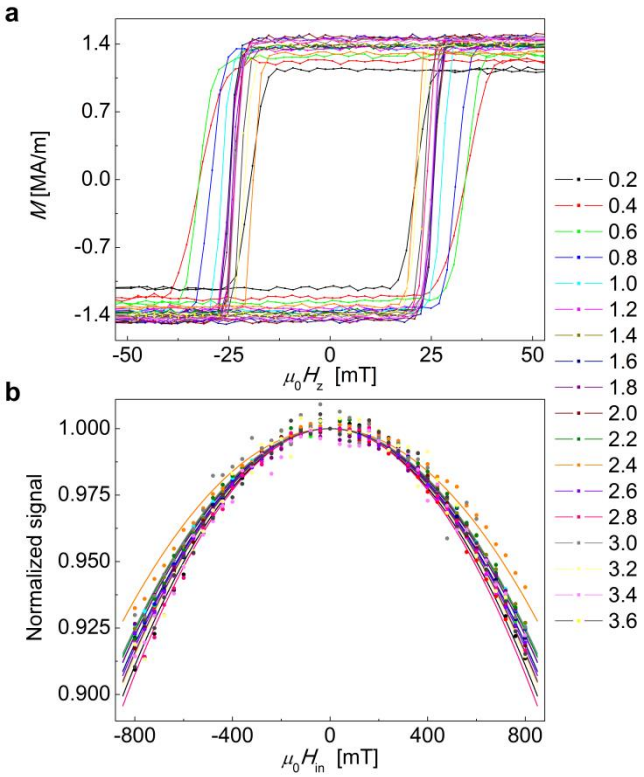

Figure 4.1. The easy-axis hysteresis loops and normalized MR signal of Pt/Co/Cu trilayers. a. The measured magnetization with respect to H_{Z}. **b,** The normalized MR signal plot measured by Hall voltage measurements with respect to H_{in}. The curved solid lines are fitting lines. Each Cu thickness is denoted in the figure, in nm units.

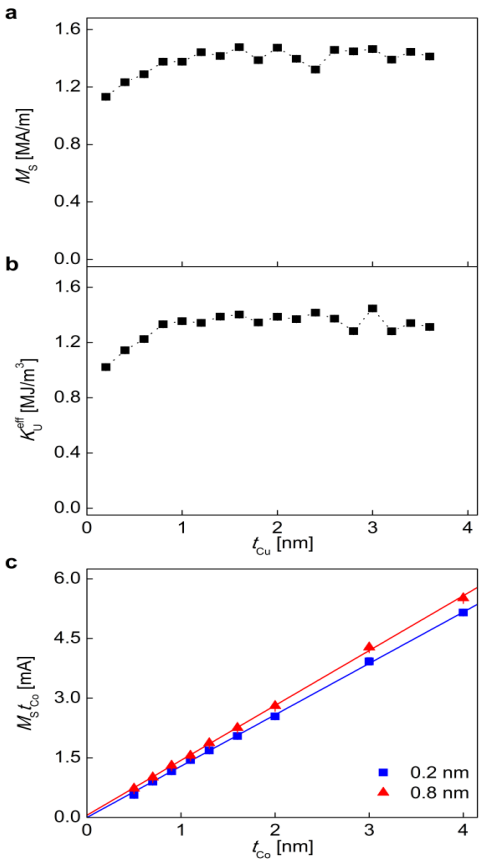

Figure 4.2. The basic magnetic parameters in Pt/Co/Cu trilayers. a. M_S and **b.** K_U^{eff} with respect to t_{Cu}. **c.** The $M_S t_{Co} - t_{Co}$ plots of Cu 0.2 nm (blue square symbols and a solid line) and 0.8 nm (red triangle symbols and a solid line). The lines are linear fitting lines.

4.4 Estimation results of DMI with Curie temperature measurement

The H_{DMI} are obtained by measurement of the SOT efficiency ε (Fig. 4.3). To measure this, the samples were patterned to 20 μm-wide and 350 μm-long

microwires by photolithography, and an Ar ion-milling process. The measured H_{DMI} seems to oscillate with respect to t_{Cu}, (Fig. 4.4a).

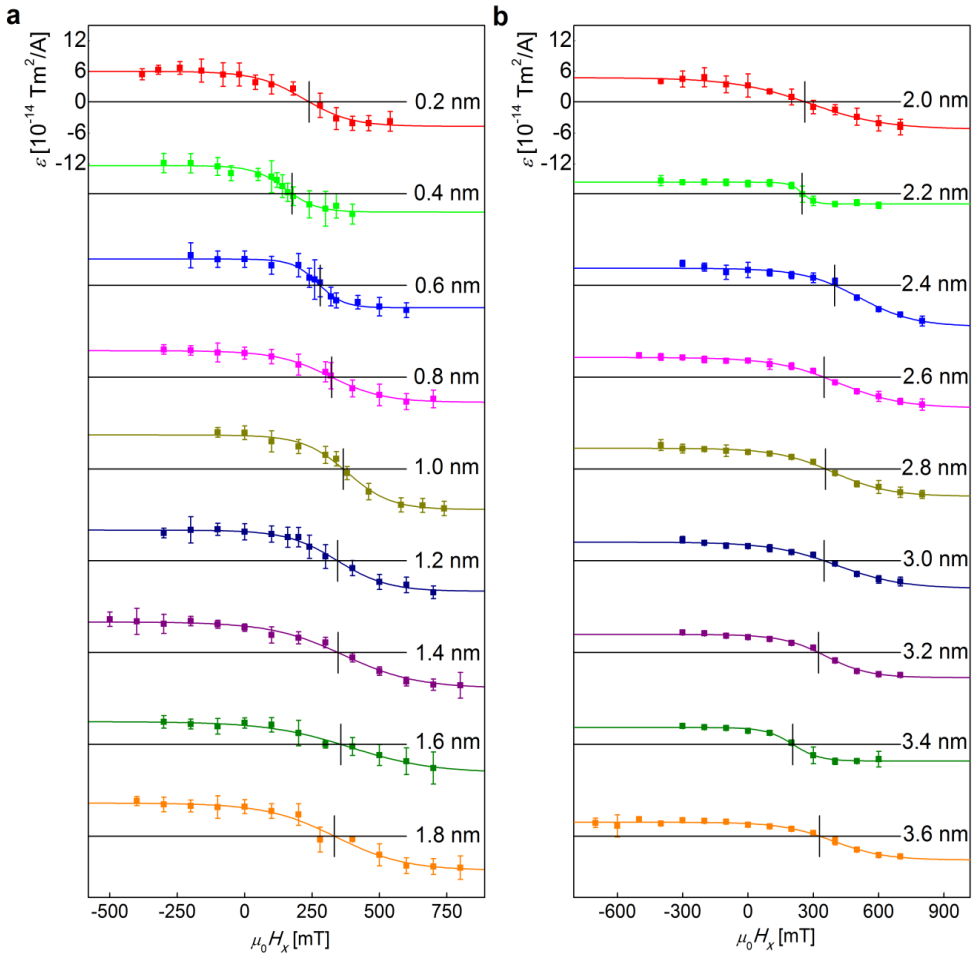

Figure 4.3. Plots of ε of Pt/Co/Cu trilayers with respect to $\mu_0 H_x$. a, The plot of ε for $0.2\ \mathrm{nm} \leq t_{\mathrm{Cu}} \leq 1.8\ \mathrm{nm}$, and **b,** for $2.0\ \mathrm{nm} \leq t_{\mathrm{Cu}} \leq 3.6\ \mathrm{nm}$. Each Cu thickness is denoted in the figure. The vertical error bars are the standard deviation for the measurements. The curved solid lines are for the eye guide. The black horizontal lines indicate the *x*-axes. The black vertical lines indicate the positions of $\varepsilon = 0$, where $H_x = -H_{\mathrm{DMI}}$.

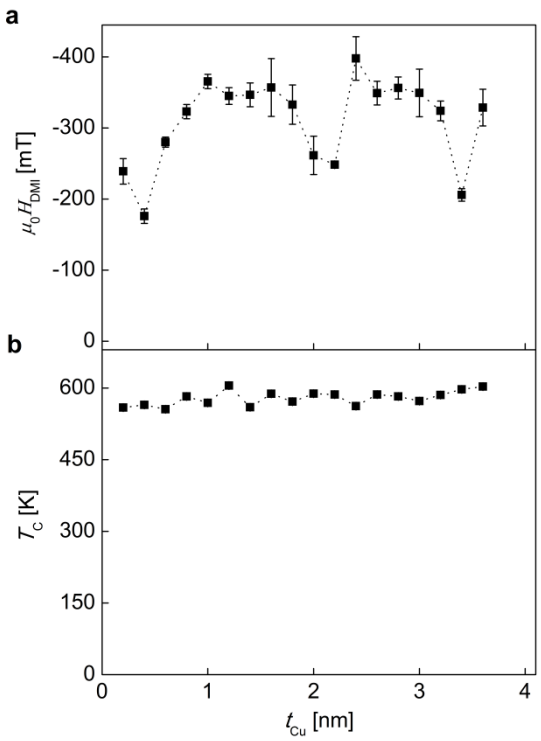

Figure 4.4. Oscillation of H_{DMI} and measured T_{C} of Pt/Co/Cu. a, The measured H_{DMI} and **b,** T_{C} with respect to t_{Cu}. The vertical error bars of H_{DMI} and T_{C} are the standard deviations of the measurements and from the fitting of the data, respectively.

Because the H_{DMI} showed a tendency to oscillate, we estimated D, the strength of the DMI, to confirm whether the DMI strength also oscillated. The relation of D to the H_{DMI} is written as $D = \mu_0 M_{\mathrm{S}} H_{\mathrm{DMI}} \lambda$, where $\lambda \left(= \left(A_{\mathrm{ex}} / K_{\mathrm{U}}^{\mathrm{eff}} \right)^{1/2} \right)$ is the DW width and A_{ex} is the exchange stiffness [23]. The result for H_{DMI} implies that D oscillates, because the M_{S} and $K_{\mathrm{U}}^{\mathrm{eff}}$ were similar

for all samples except for the thin Cu samples. The one remaining parameter is A_{ex}, and this should be measured or indirectly estimated, because the A_{ex} may also oscillates in QW systems [85].

To estimate the degree of possible change of A_{ex} effectively, we obtained the Curie temperature, T_{C}, from the Arrott plot [87], (Fig. 4.5) because it is known that A_{ex} is proportional to T_{C} [85,88]. T_{C} is estimated by the Arrott plot of the easy-axis loop, measured via VSM with temperature variation. We followed the estimation method found in Ref. 87. From the Weiss-Brillouin treatment, the relation of magnetization M to temperature T is expressed as $M = M_0 \tanh\left(\frac{\mu(H_{\mathrm{Z}}+NM)}{k_B T}\right)$, where $N = \left(\frac{k_B T_{\mathrm{C}}}{\mu M_0}\right)$ is the molecular field constant, and μ is the moment per atom [87]. The above equation can be analyzed with a Taylor expansion, $\frac{\mu H_{\mathrm{Z}}}{k_B T} = \left(1 - \frac{T_{\mathrm{C}}}{T}\right)\frac{M}{M_0} + \frac{1}{3}\left(\frac{M}{M_0}\right)^3 + \frac{1}{5}\left(\frac{M}{M_0}\right)^5 + \cdots$. For temperature near T_{C}, where $M \ll M_0$, this can be approximated and summarized in the form $M^3 = -C_1(T - T_{\mathrm{C}})M + C_2 H_{\mathrm{Z}}$, or $M^2 = -C_1'(T - T_{\mathrm{C}}) + C_2' H_{\mathrm{Z}}/M$. When $T = T_{\mathrm{C}}$, the relationship becomes linear in the $M^3 - \mu_0 H_{\mathrm{Z}}$ plot and the $M^2 - \mu_0 H_{\mathrm{Z}}/M$ plot. The plots of $M - \mu_0 H_{\mathrm{Z}}$, $M^3 - \mu_0 H_{\mathrm{Z}}$, and $M^2 - \mu_0 H_{\mathrm{Z}}/M$ of the Cu 1.6 nm sample are demonstrated in Fig. 4.5a-c, and the $M^2 - \mu_0 H_{\mathrm{Z}}/M$ plots of other samples are also shown in Fig. 4.5d-t. The plots of $M^2 - \mu_0 H_{\mathrm{Z}}/M$ show similar tendencies, as shown in Ref.89. In Fig. 4.5b, the data appear to show a linear tendency at 585 K and 590 K. For these data, linear fittings were conducted (Fig. 4.5c). The fitting ranges in Fig. 4.5c were set identical to the H_{Z} value range showing the linear tendency in the $M^3 - \mu_0 H_{\mathrm{Z}}$ plot.

T_C was estimated from each intersection of the y-axis and fitting lines. The summarized values of T_C in Table 4.1 are the average values of those values estimated from each fitting, and the error bars are estimated as the difference of each T_C value from the mean value. The T_C values of the other samples were all obtained in the same way.

The estimated T_C with respect to t_{Cu} are shown in Fig. 4.4b. As seen in the case of the M_S and K_U^{eff}, the T_C of the samples are similar for the whole range of t_{Cu}. There could be an oscillation of T_C, but it is not easy to distinguish whether it oscillates or is simply scattered in our data. Besides, the variation of T_C between the samples is quite small, where the average T_C is 578.77 K and the standard deviation is 15.21 K. Therefore, A_{ex} may not vary significantly across our samples, and may also have no effect on the DMI tendency.

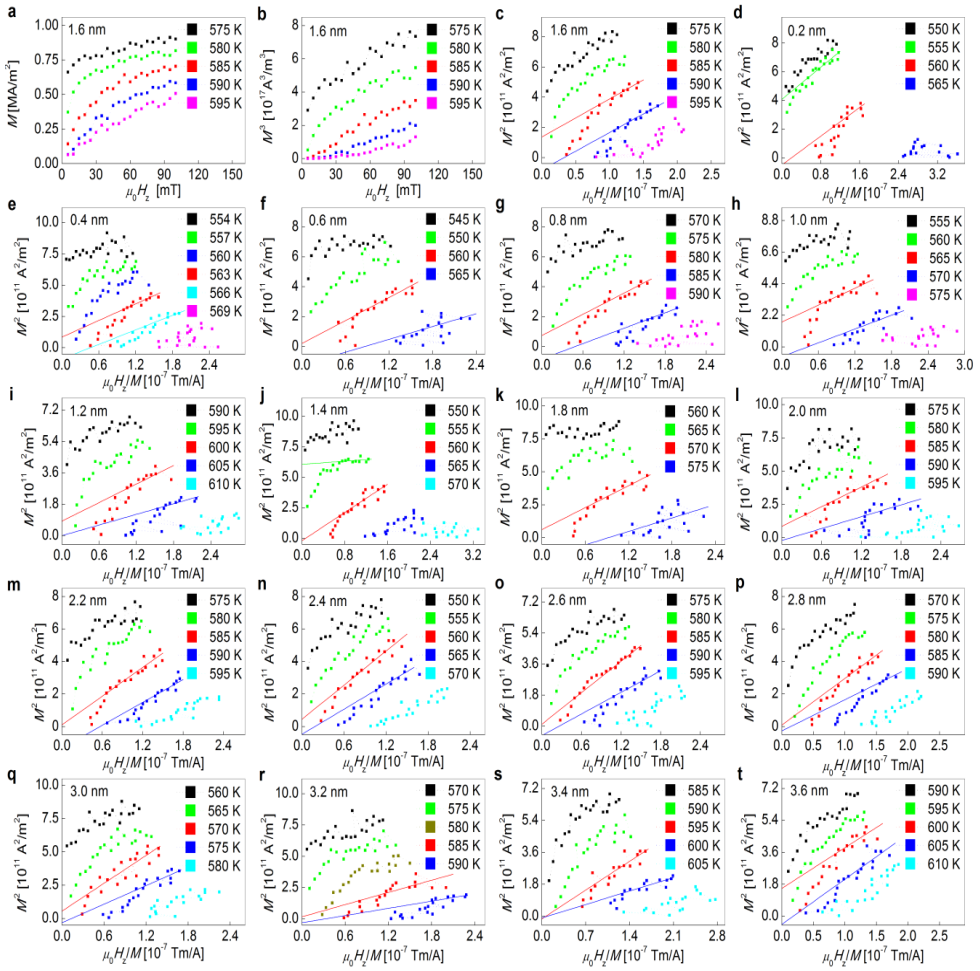

Figure 4.5. Plots of $M-\mu_0 H_Z$, $M^3-\mu_0 H_Z$, and $M^2-\mu_0 H_Z/M$ for different Cu thickness. a, The $M-\mu_0 H_Z$, and **b,** $M^3-\mu_0 H_Z$ plot of a Cu 1.6 nm sample. **c-t**, the $M^2-\mu_0 H_Z/M$ plot of all samples. Each Cu thickness is denoted in the figure. The temperature of each plot is also denoted in the figure. The solid lines are linear fitting lines.

Therefore, we used a constant value of $A_{\mathrm{ex}}(= 14\ \mathrm{pJ/m})$[61] for the estimation of D, and the result shows that the DMI oscillates with respect to t_{Cu} (Fig. 4.6a). To obtain the oscillation period, we assume an empirical oscillation relation $D = D_0 \sin(2\pi t_{\mathrm{Cu}}/\lambda_{\mathrm{DMI}})/t_{\mathrm{Cu}} + C_{\mathrm{DMI}}$ because as yet, there are no models describing DMI oscillations in a QW. The DMI oscillation period, $\lambda_{\mathrm{DMI}} = 1.27 \pm 0.088$, was estimated. Here, the fitting range considered was $1.8\ \mathrm{nm} \leq t_{\mathrm{Cu}} \leq 3.6\ \mathrm{nm}$, for effective comparison of the data with that of the RKKY interaction discussed later in this chapter. The estimated period is similar with that of RKKY interaction in other research using Cu(111) [90]. If the DMI oscillation in our samples is a phenomenon caused by conduction electrons in the QW state, it will be necessary to compare oscillation tendencies and periods across different measurements of similar situations and structures.

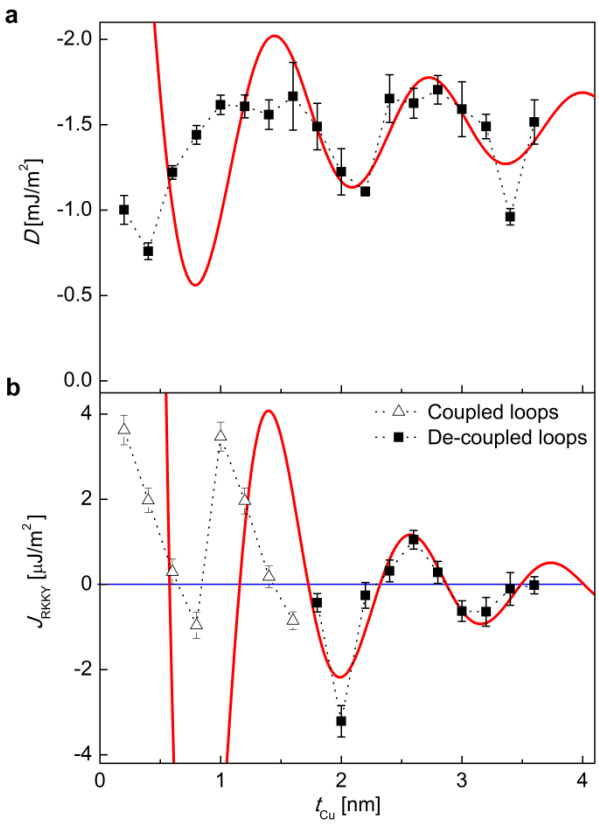

Figure 4.6. Plots of D and J_{RKKY} with respect to t_{Cu}. The plots of **a,** D, and **b,** J_{RKKY}. The J_{RKKY} obtained from coupled loops (open triangle symbols) and de-coupled loops (filled square symbols) are shown together in (b). The horizontal blue line in (b) is where $J_{\mathrm{RKKY}} = 0$. The vertical error bars in (a) are the standard deviation of the measurement, and the vertical error bars in (b) are from the measurement accuracy.

4.5 Estimation of RKKY interaction and comparison with DMI

We measured the RKKY interaction period in samples resembling as closely as possible the structure for the DMI measurement, and compared the period with that of the DMI. Spin valve structures were fabricated for this, and the structure is 1.5-nm Ta/5-nm Pt/0.5-nm Co/t_{Cu} Cu/0.2-nm Pt/0.5 nm Co/1.5-nm Pt. Here, Cu t_{Cu} also varies from 0.2 nm to 3.6 nm with 0.2 nm increments. All fabrication conditions are kept identical to that of the samples for the DMI measurement. We intend Co/Cu(t_{Cu})/Co spin valve structure basically.

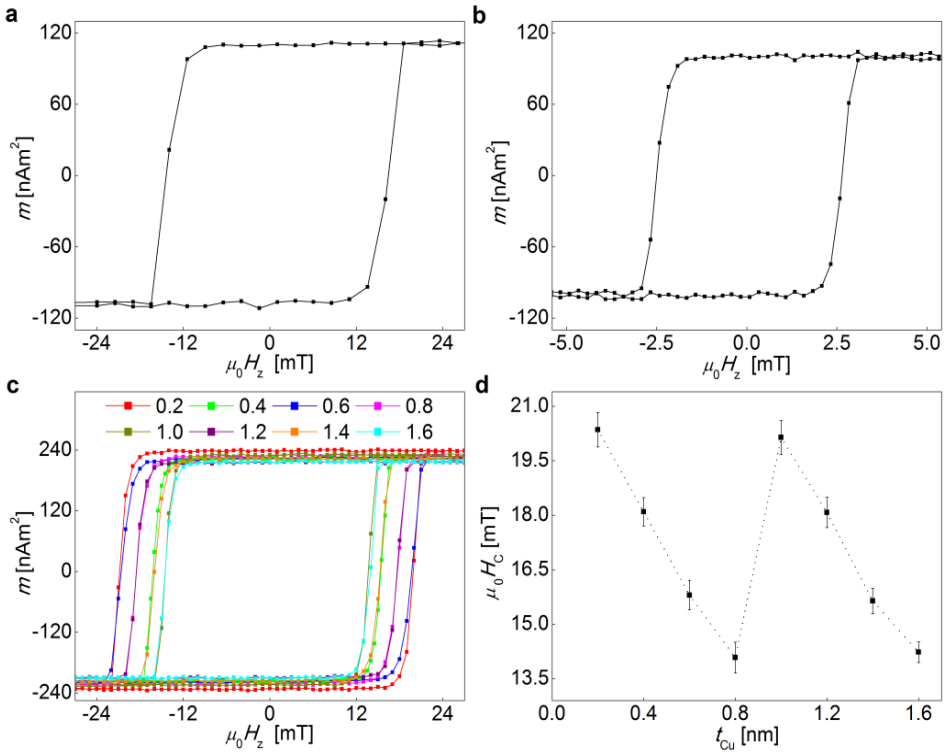

Figure 4.7. The easy-axis hysteresis loops of trilayers and spin valve structures, and the coercivity of samples with respect to t_{Cu}. The easy-axis hysteresis loop of **a,** the Pt/Co/Cu trilayer, and **b,** the Cu/(Pt)/Co/Pt trilayer. **c.** The easy-axis hysteresis loops of spin valve structure samples. Each Cu thickness is denoted in the figure in nanometer units. **d.** The coercivity values with respect to t_{Cu}. The vertical error bars arise from the measurement accuracy.

Before fabricating and measuring the RKKY interaction in a full stack of the Co/Cu/Co spin valve structure, the PMA conditions for each lower and upper trilayer were confirmed by measurement via VSM. The easy-axis hysteresis loop in

Fig. 4.7a is of 1.5-nm Ta/5-nm Pt/0.5-nm Co/3-nm Cu/2-nm Pt. In fact, the lower trilayer structure of Pt/Co/Cu has PMA. We then fabricated and measured the hysteresis loop of 1.5-nm Ta/5-nm Pt/3-nm Cu/0.5-nm Co/2-nm Pt. This Cu/Co/Pt sample did not exhibit PMA (not shown). Therefore, we inserted 0.2 nm Pt at the Cu/Co interface. The easy-axis hysteresis loop in Fig. 4.7b is of 1.5-nm Ta/5-nm Pt/3-nm Cu/0.2-nm Pt/0.5-nm Co/2-nm Pt. The upper trilayer structure of Cu/(Pt)/Co/Pt exhibits PMA. Therefore, the chosen structure of the spin valve is Pt/Co/Cu(t_{Cu})/(Pt)/Co/Pt.

For $t_{\mathrm{Cu}} \leq 1.6\,\mathrm{nm}$, the lower and upper trilayers were coupled, and only one hysteresis loop was obtained (Fig. 4.7c). In the measured loops, the coercivity, H_{C}, varied with the Cu thickness. The obtained H_{C} are shown in Fig. 4.8d. Some studies have shown coercivity oscillations [91, 92] in spin valve structures with coupled hysteresis loops as in this study, and interpreted the results as originating from the RKKY interaction [91]. The strength of the RKKY interaction in a coupled hysteresis loop may be understood as the relation $J_{\mathrm{RKKY}} = \mu_0\left(H_{\mathrm{C}} - H_{\mathrm{C},0}\right)M_{\mathrm{S}}t_{\mathrm{Co}}$ [91]. Here, the H_{C} is of the Co/Cu/(Pt)/Co spin valve structure, and the $H_{\mathrm{C},0}$ is of the Pt/Co/Cu trilayer structure (Fig. 4.7a). The estimated J_{RKKY} of the samples with $t_{\mathrm{Cu}} \leq 1.6\,\mathrm{nm}$ are summarized in Table 4.2.

For $t_{\mathrm{Cu}} \geq 1.8\,\mathrm{nm}$, the lower and upper trilayer was de-coupled (Fig. 4.8a-j). The minor loops were measured, and H_{S}, the effective field of the minor loop shift caused by the RKKY interaction, is estimated from the position of the minor loop center (Fig. 4.8b). The obtained H_{S} are shown in Fig. 4.8l, and the oscillatory tendency can be seen. The J_{RKKY} in the samples with $t_{\mathrm{Cu}} \geq 1.8\,\mathrm{nm}$ were

estimated by the relation $J_{\mathrm{RKKY}} = \mu_0 H_{\mathrm{S}} M_{\mathrm{S}} t_{\mathrm{Co}}$ [91], and are summarized in Table 4.2. The results are shown in Fig. 4.6b, and the oscillation period $\lambda_{\mathrm{RKKY}} (= 1.16 \pm 0.066\ \mathrm{nm})$ was obtained from the relation $J_{\mathrm{RKKY}} = J_{\mathrm{RKKY},0} \sin(2\pi t_{\mathrm{Cu}}/\lambda_{\mathrm{RKKY}})/t_{\mathrm{Cu}}^2 + C_{\mathrm{RKKY}}$ [91], here, the fitting range considered is $1.8\ \mathrm{nm} \leq t_{\mathrm{Cu}} \leq 3.6\ \mathrm{nm}$. The period λ_{RKKY} is similar to λ_{DMI}, the phase is also similar, though features slight differences, implying that these may share some common causes.

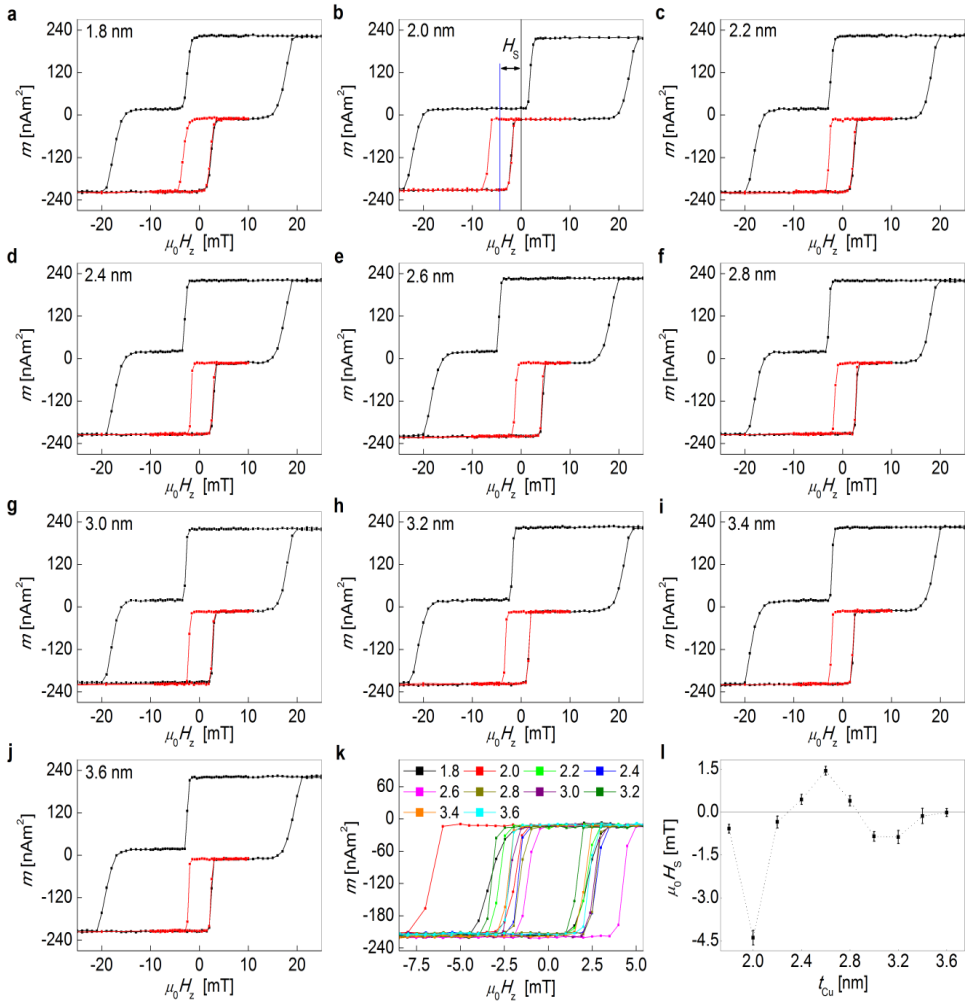

Figure 4.8. The easy-axis hysteresis loops of spin valve structures, and the shift field of the samples with respect to t_{Cu}. a-j. The easy-axis hysteresis loops spin valve structure samples. The major loops are shown in black, the minor loops are in red. Each Cu thickness is denoted in the figure. The H_S is indicated in (b). **k.** All minor loops are drawn in one place. Each Cu thickness is denoted in nanometer units. **l.** The H_S value with respect to t_{Cu}. The vertical error bars are from the measurement accuracy.

4.6 Discussion

Both of the periods were similar to that of the RKKY interaction in a previous experiment with Cu (111) [90]. It is known that the structure and growth orientation of ultrathin Co is fcc and (111) on Pt(111), respectively, and that the sample exhibit PMA in Pt(111)/Co(111) structures [6,78]. Likewise, the Cu layer on Co (111) may also have a (111) orientation because Cu also have the crystal structure of fcc, and the lattice constant of Cu is similar to that of fcc Co [93,94]. Therefore, the Cu crystal orientation lying in the direction perpendicular to the film plane may be (111) in our samples, and for the DMI and RKKY interaction it seems to be Cu(111). In addition, the Cu layer of our samples may have a polycrystalline structure, as the samples were fabricated by DC magnetron sputter. If the growth orientation of Cu is well-defined, a more precise period value will be obtained, and orientation dependent periods will be observed.

In the Cu/Co/Cu(t_{Cu}) structure, even if there is a single ferromagnetic layer rather than a double ferromagnetic layer such as a spin valve structure, there is research showing that the oscillations of parameters such as T_{C} and A_{ex}, with respect to t_{Cu}, can change [82,84,85]. For structures with a spacer near one ferromagnetic layer such as Cu/Co/Cu(t_{Cu}) or Pt/Co/Cu(t_{Cu}) structures [82], and for structures with a spacer sandwiched by ferromagnetic layers such as the Co/Cu(t_{Cu})/Co structure [95], oscillations with half the characteristic oscillation period of Cu are expected. Apart from this, the period itself is known to be

insensitive to adjacent materials, and to be determined by the characteristic of Cu [82]. In this regard, the period of the DMI in Pt/Co/Cu and the RKKY interaction in Co/Cu/(Pt)/Co can be similar. Therefore, the oscillation period values of the DMI and RKKY interaction obtained in our experiment are reasonable, and the results of our DMI oscillation experiment are thought to be due to the QW state.

This DMI strength oscillation may be thought of as arising from phenomena in the QW state. A. Fert and P.M. Levy suggested the DMI mechanism by the spin-orbit scattering of interaction-mediating conduction electrons and orbitals of impurities in metallic systems [12]. If dominant conduction electron states are affected and constrained by the QW state near the interface of Co/Cu, the DMI may oscillate via these dominant conduction electrons. The result may not have been seen before, and so there is no exact model for it and many experimental and theoretical studies will be required.

For Cu of thicknesses less than about 1 nm, neither oscillations match well with fitting (Fig. 4.6). In this thinner thickness range, the proper oscillation periods seem to be larger than the estimated λ_{DMI} and λ_{RKKY}. One possible reason may be linked to the change of M_{S} and $K_{\mathrm{U}}^{\mathrm{eff}}$ compared with the parameters for $t_{\mathrm{Cu}} \geq 0.8$ nm. We do not fully understand why the magnitudes of the parameters change in thin Cu thickness ranges, but unknown details of the conditions of the samples may be different for this range, causing oscillation period variations. Another possible reason is the existence of another oscillation vector. In Cu, the oscillation occurs by one special k–vector only, or by two or more k–vectors [95,96]. Among the k–vectors, the comparatively short oscillations caused by longer k–vectors are often

eliminated by the interface conditions [96], and this shorter oscillation may only be seen in an ultrathin QW state, causing oscillation period variation. Although the k–vectors involved in the oscillation depend strongly on the crystal structure and orientation [95], this hypothesized explanation of the oscillation period variation in thinner Cu is reasonable, because our samples may have the polycrystalline structure of Cu. The other possibility is that the k-vector itself may vary depending on the Cu thickness [82]. It was suggested in Ref.16 that this k-vector consists of the components determined by the QW state and by the bulk Bloch function [82]. It may be natural to think that the k-vector will follow the bulk value as the thickness of Cu increases, while the k-vector is different in thin Cu from that in bulk thicknesses due to the influence of the two components [82].

A further significant point is that the variation of the DMI strength is quite large with respect to t_{Cu} because it has typically been expected that in Cu, the strengths of SOC-related phenomena may be small, including the DMI. Our results suggest that the DMI can respond sensitively to the structural factors of non-magnetic layers as well as the materials themselves, with a non-negligible contribution from non-adjacent layers of the non-magnetic layer. From these results, it can also be thought that specifics of the sample structure such as thickness of non-magnetic layers and the material of the reflection layer on the QW should be considered as well as the non-magnetic material itself, to maximize the DMI strength. Conversely, this result has not been found before, and this may be because the phenomenon does not occur or is not obvious, depending on the specific conditions or structures. In Ref.82, it is shown that the oscillation shows a “cut-off”,

or suddenly disappears when the spacer thickness is increased to a certain extent, which may depend on the materials and sample quality [82].

Further insight from the results may provide new possibilities for engineering DMIs, by changing the conditions of non-magnetic layers through various methods such as alloying the non-magnetic layer, stacking the multilayer of the non-magnetic layer rather than a single layer, controlling the growth orientation of non-magnetic layers, which relate to the changing bulk properties, or by changing the conditions of the interface between the QW and reflection layers, which is relevant in changing the phase. It has been suggested that the oscillation phase in the QW depends on the condition of the interfaces [82]. Even for the same QW thickness, phase changes may bring about changes in the DMI strength. In addition, for the case of RKKY interaction, the oscillation phase change by interface alloying in spin valve system was already shown [97].

4.7 Conclusion

We demonstrate the existence of oscillations of the DMI in Pt/Co/Cu trilayers, with a QW of Cu. By comparing them with the RKKY interaction in a Co/Cu/(Pt)/Co spin valve structure, the DMI oscillation behaviour can be seen to share some causes with these interactions. Our results provide new perspectives for understanding the DMI beyond the interfacial perspective. From our results, another “degree of freedom” of the DMI engineering is expected through alloying,

multilayer-staking, and controlling the growth orientation of non-magnetic layers, and by controlling the interface condition between QW and the capping layer of QW.

t_{Cu} **[nm]**	M_S [MA/m]	$\mu_0 H_K$ [T]	K_U^{eff} [10^6 J/m^3]	$\mu_0 H_{DMI}$ [mT]	D [mJ/m^2]	T_C [K]
0.2	1.13±0.020	1.81±0.011	1.02±0.018	-239.03±17.92	-1.00±0.084	$559.06^{+0.04}_{-4.06}$
0.4	1.23±0.017	1.86±0.008	1.14±0.015	-175.98±10.16	-0.76±0.049	$564.77^{+1.23}_{-1.77}$
0.6	1.29±0.018	1.90±0.004	1.23±0.017	-280.11±7.08	-1.22±0.040	$555.39^{+4.61}_{-5.39}$
0.8	1.38±0.020	1.94±0.006	1.33±0.020	-323.05±10.03	-1.44±0.055	$582.31^{+2.69}_{-2.31}$
1.0	1.38±0.021	1.97±0.005	1.35±0.020	-365.43±10.04	-1.62±0.057	$568.98^{+398}_{-1.02}$
1.2	1.44±0.022	1.86±0.005	1.34±0.021	-345.01±11.70	-1.61±0.067	$605.02^{+4.98}_{-0.02}$
1.4	1.42±0.019	1.96±0.007	1.39±0.019	-346.63±16.75	-1.56±0.086	$559.65^{+0.35}_{-4.65}$
1.6	1.48±0.014	1.90±0.006	1.40±0.013	-356.99±40.64	-1.67±0.20	$587.89^{+2.11}_{-2.89}$
1.8	1.39±0.022	1.94±0.010	1.35±0.021	-332.87±27.65	-1.49±0.14	$571.35^{+3.65}_{-1.35}$
2.0	1.47±0.021	1.88±0.005	1.39±0.019	-261.51±26.98	-1.22±0.14	$588.13^{+1.87}_{-3.13}$
2.2	1.40±0.016	1.96±0.011	1.37±0.016	-248.38±4.24	-1.11±0.025	$586.27^{+3.73}_{-1.27}$
2.4	1.32±0.019	2.14±0.018	1.42±0.020	-397.83±30.66	-1.65±0.14	$562.05^{+2.95}_{-2.05}$
2.6	1.46±0.017	1.88±0.005	1.37±0.016	-349.09±16.71	-1.63±0.088	$586.44^{+3.56}_{-1,44}$
2.8	1.45±0.015	1.77±0.023	1.28±0.014	-356.24±15.49	-1.70±0.083	$582.31^{+2.69}_{-2.31}$
3.0	1.46±0.014	1.98±0.023	1.45±0.014	-349.31±33.47	-1.59±0.16	$572.67^{+2.33}_{-2.67}$
3.2	1.39±0.014	1.84±0.017	1.28±0.013	-324.14±13.89	-1.49±0.072	$585.39^{+4.61}_{-0.39}$
3.4	1.45±0.020	1.86±0.015	1.34±0.019	-205.83±8.82	-0.96±0.048	$597.18^{+2.82}_{-2.18}$
3.6	1.41±0.019	1.86±0.014	1.31±0.017	-328.69±25.78	-1.52±0.13	$603.01^{+1.99}_{-3.01}$

Table 4.1 Measured and estimated magnetic properties of Pt/Co/Cu(t_{Cu}) samples.

t_{Cu} **[nm]**	$\mu_0 H_C$ [mT]	J_{RKKY} [10^{-7} J/m^2]	t_{Cu} [nm]	$\mu_0 H_S$ [mT]	J_{RKKY} [10^{-7} J/m^2]
0.2	20.35±0.47	36.23±3.46	**1.8**	-0.59±0.15	-4.31±2.15
0.4	18.10±0.39	19.72±2.86	**2.0**	-4.39±0.25	-32.12±3.68
0.6	15.80±0.41	2.95±2.98	**2.2**	-0.35±0.21	-2.57±3.02
0.8	14.08±0.42	-9.62±3.10	**2.4**	0.43±0.17	3.18±2.56
1.0	20.14±0.47	34.69±3.41	**2.6**	1.44±0.15	10.50±2.21
1.2	18.08±0.42	19.60±3.05	**2.8**	0.39±0.18	2.82±2.58
1.4	15.64±0.35	1.78±2.58	**3.0**	-0.86±0.17	-6.27±2.43
1.6	14.23±0.28	-8.52±2.08	**3.2**	-0.88±0.23	-6.43±3.38
-	-	-	**3.4**	-0.14±0.26	-1.06±3.84
-	-	-	**3.6**	-0.02±0.14	-0.18±2.02

Table 4.2 Measured and estimated magnetic properties of Pt/Co/Cu(t_{Cu})/Pt(0.2)/Co/Pt samples.

Chapter 5

Application to magnetic devices by DMI engineering

The previous chapters presented studies of the physical aspects of the DMI. In this chapter, DMI engineering was conducted by applying the results obtained from these studies. One of the factors found in previous studies was that the samples exhibit PMA at thinner Co thicknesses when an ultrathin Cu layer is used. Another factor is that the DMI is large in the Pt/Co/Cu trilayer structure. Moreover, copper is known to have a spin diffusion length of approximately 500 nm, as described in the previous chapter, and thus, the spin current injected through the thin Cu layer from the outer non-magnetic layer is expected to be reduced relatively less. For these reasons, Cu was used for DMI engineering, and research was conducted to reduce the magnetization switching current.

5.1 Introduction

Based on various current-induced magnetization processes with spin-transfer torque (STT) and/or SOT [23,98-100] many attempts have been made to realize magnetic devices via current control of magnetization states. One of the most successful prototypes so far is the STT- or SOT-driven magnetization switching [101], which provides building blocks of emerging magnetic memory, logic, and

many other types of devices, due to their non-volatile characteristics with high density and stability.

The most important issues in these magnetic devices are to achieve sufficiently high thermal stability and simultaneously, sufficiently low switching current density. The high thermal stability is required to avoid unwanted switching i.e. memory loss with thermal fluctuation. In practice, the thermal stability factor Δ $(= K_{\mathrm{U}}V/k_{\mathrm{B}}T)$ should be larger than about 40 to secure the data storage stability over 10 years [102]. With decreasing the device volume V for high density storage devices, the magnetic anisotropy K_{U} has to be enhanced accordingly to sustain the proper magnitude of Δ to resist the thermal fluctuation energy $k_{\mathrm{B}}T$. However, a large K_{U} inevitably increases the switching current density through enhancement of switching energy barriers. Therefore, it is difficult to achieve both the thermal stability and switching efficiency simultaneously.

On the other hand, recent studies have revealed that the Dzyaloshinskii-Moriya interaction (DMI) can play a key role in magnetization switching via domain nucleation [73,103,104]. These results suggest that the DMI materials possibly provide an opportunity to control the switching current irrespective of the thermal stability by adjusting the strength of DMI [103, 105]. Since the magnetization switching in the DMI materials is known to initiate at pattern edges, the precise structure engineering and also, study on detailed mechanisms with respect to the device structures are required.

To clearly demonstrate the relation between the switching current density and the DMI strength, it is required to control the DMI strength over a wide range. For

this purpose, we designed a series of films that varies from symmetric (Pt/Co/Pt) to asymmetric (Pt/Co/Cu/Pt) layered structures by inserting an ultrathin Cu layer with various thickness. The Cu insertion layer was selected by following reasons: According to the previous reports [3,77], an ultrathin Cu insertion layer barely changes the PMA irrespective of its thickness. Also, it has been observed that the Cu-insertion films maintain strong PMAs even for thin Co layers. Since the DMI strength follows interfacial characteristics of inverse proportionality on the Co layer thickness [71-73], such thin Co-layered films exhibit large DMI strengths and consequently, a large DMI variation is expected with respect to the insertion layer thickness [77]. To avoid the current shunt to the insertion layer, we limited the thickness of the insertion layers up to 0.4 nm. Then, by measuring the energy barrier and switching current density in addition to the strengths of PMA and DMI from the series of films, we demonstrated that it is possible to achieve simultaneously both thermal stability enhancement and switching current reduction.

5.2 Experimental details

The stacks of films fabricated for the experiments are 5-nm Ta/8-nm Pt/0.3-nm Co/t_{Cu} Cu/1.5-nm Pt with varying t_{Cu} (0, 0.2, and 0.4 nm). All samples were deposited by DC magnetron sputtering on Si wafers with a 300-nm-thick SiO_2 layer. The lowermost Ta is employed as a seed layer. To measure ε and H_{DMI}, 20 μm-wide and 350 μm-long microwires were patterned by photolithography and an ion-

milling processes. To inject electric current into the microwires, 5/100-nm-thick Cr/Au electrodes were deposited by a lift-off process.

5.3 Confirmation of magnetic parameter variation with ultrathin Cu layer insertion

The changes of magnetic parameters were measured, with the measurement results shown in Fig. 5.1. The M_S does not change much is confirmed by a comparison of the intensity of the easy-axis hysteresis loops measured by VSM (Fig. 5.1a). From the measurement of MR by AHE with respect to H_{in}, the H_K are estimated. Fig. 5.1b clearly shows that H_K becomes large when the t_{Cu} increases, indicating that K_U^{eff} is also increased. The ε_0 and H_{DMI} were then obtained by measuring the SOT efficiency. The measurement technique was the same as the method introduced in Chapter 1. As we expected, Fig. 5.1c shows the relatively small and large changes of ε_0 and H_{DMI} by ultrathin Cu layer insertion, estimated from the saturation regions of ε and the position where $\varepsilon = 0$, respectively. The measured parameters are listed in Table 5.1.

From the increase of K_U^{eff}, it can be immediately inferred that the thermal stability of the sample increased due to the insertion of the ultrathin Cu layer, without an external magnetic field. Conversely, if a magnetic field is induced in the samples, the situation becomes more complicated. It is known that the domain nucleation energy barrier is proportional to the square of the DW energy density σ_{DW} when the external perpendicular magnetic field is applied to the PMA system

[104,106,107]. Here, $\sigma_{\mathrm{DW}} = 4\sqrt{A_{\mathrm{ex}}K_{\mathrm{U}}^{\mathrm{eff}}} - \pi\mu_0 H_{\mathrm{DMI}} M_{\mathrm{S}}\lambda$ for Néel-type DWs with $\lambda\left(=\left(A_{\mathrm{ex}}/K_{\mathrm{U}}^{\mathrm{eff}}\right)^{0.5}\right)$ [23,33]. As the Cu thickness increases, not only $K_{\mathrm{U}}^{\mathrm{eff}}$ but also H_{DMI} increases in our samples, so the increases of the two parameters may cancel each other out. Therefore, it is necessary to confirm the changes of the domain nucleation energy barrier due to the ultrathin Cu layer insertion.

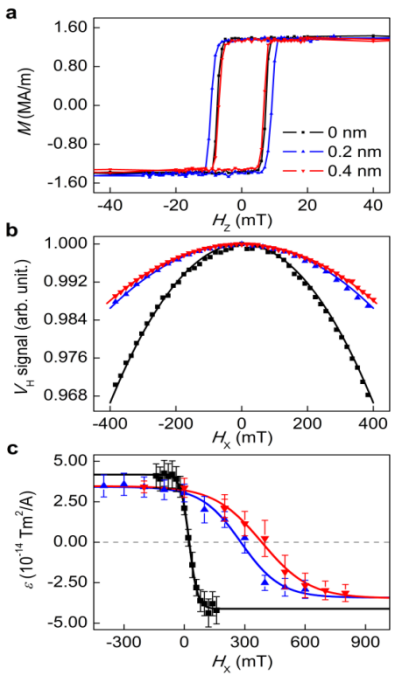

Figure 5.1 The measured basic magnetic parameter with ultrathin Cu layer insertion. a. The easy-axis hysteresis loop measured by VSM. **b.** The normalized MR signal with respect to H_x. The symbols represent measured data and the solid lines are fitting lines. **c.** Plots of ε with respect to $\mu_0 H_x$. The vertical error bars are the standard deviation of several repeated measurements. The grey horizontal line indicates the x-axis. The curved solid lines are the eyes guides. All black, blue, and red symbols and lines correspond to the data of Cu 0, 0.2, and 0.4 nm, respectively.

5.4 Measurement of field-induced magnetization switching

Relative energy barrier changes were confirmed by field-induced magnetization switching (FIMS). For FIMS measurements, samples were patterned with a 6-μm-diameter dot of Co/Cu/Pt on a 10-μm-width Hall bar of Ta/Pt (Fig. 5.2a). The magnetization switching was observed by monitoring m_z via the AHE signal V_{H} ($\propto m_z$). In this measurement, the current density J was kept as low as possible (~7×10^8 A/m^2) to avoid the effect of the SOT, where the SOT-induced effective magnetic field is estimated negligible small (~0.02 mT).

To confirm the magnetization switching type of the sample, the relative change of the switching field H_{SW} was firstly measured by changing the angle ϕ of the external magnetic field. If the switching process is single domain switching, the H_{SW} will follow the trend described by the Storner-Wohlfarth (SW) model [108]. Conversely, if the sample is switched through local domain nucleation and subsequent DW propagation, the H_{SW} will follow the trend described by the Kondorsky model [109]. Our samples all follow the trend expected by the Kondorsky model, as indicated by the dashed magenta line in Fig. 5.2b.

The magnetization switching probability, P, was first measured to estimate the relative energy barrier. When a constant H_{Z} is induced in the sample, the P is expressed as $P = 1 - \exp(-t/\tau)$, where the t is the magnetic field induction time,

and the τ is the characteristic time for the switching, following the exponential relation $\tau = \tau_0 \exp(E_B/k_B T)$ [107,110]. In the magnetic droplet model, the energy barrier E_B has the expression $E_B = \Lambda\left(\frac{1}{H_Z} - \frac{1}{H_0}\right)$ [104,106,107], where $\Lambda\left(= \frac{\pi\sigma_{DW}^2 t_{Co}}{2\mu_0 M_S k_B T}\right)$ is the relative energy barrier, t_{Co} is the Co thickness, k_B is the Boltzmann constant, and T is the temperature. Here, H_0 is maximum coercivity, and we set its value to H_K [106]. For similar magnitudes of H_Z, Λ will be proportional to E_B, so the relative energy barrier can be estimated by the magnitude of Λ.

The samples were switched with a different constant H_Z and thermal assistance, and Fig. 5.2c-e shows the exponential tendency of the P for each sample. We then obtained τ using the relation $P = 1 - \exp(-t/\tau)$, and drew $\ln(\tau) - 1/H_Z$ (Fig. 5.2f). In these plots, Λ can be found from the slope of the linear fitting line, and the estimated Λ are listed in Table 5.2. Λ increases with Cu thickness, and it is understood that σ_{DW} is increased with the increase of t_{Cu}, and the relative energy barrier is consequently increased.

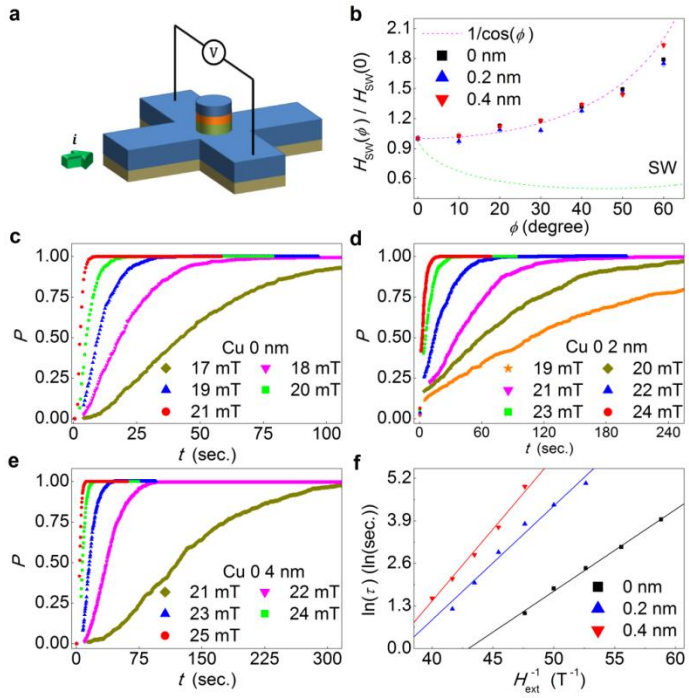

Figure 5.2 The relative energy barrier measurement with FIMS estimated by measurement of switching probability. a. Image depicting the sample structure. 6-μm-diameter Co/Cu/Pt circular dot is on a 10-μm-width Ta/Pt cross Hall bar. **b.** The relative switching field with respect to the angle of applied external field. The dashed magenta line is the estimated trend from the Kondorsky model, and the dashed green line is from the Storner-Wohlfarth model. **c-e.** The switching probability P with respect to field induction time t for different constant external fields. The Cu thickness and field value are denoted in (c)-(e). **f.** The plot of $\ln(\tau)$ with respect to $1/H_Z^{\mathrm{ext}}$. The symbols represent the measured data and solid lines are linear fitting lines. In (b) and (f), all black, blue, and red symbols and lines correspond to the data of Cu 0, 0.2, and 0.4 nm, respectively.

To cross-check this result, the coercivity, H_C, of the dot-patterned samples was measured by MOKE microscopy for changes in the external magnetic field sweep

speed, dH_Z/dt. As demonstrated in Fig. 5.3a, H_C is altered under different sweep speeds. H_C with respect to the sweep speed of each sample is shown in Fig. 5.3b. The relation of H_C to dH_Z/dt is written as $\frac{dH_Z}{dt} = \frac{\exp\left(\frac{\Lambda}{H_0}\right)}{\tau_0 \ln(2)}\left[H_C \exp\left(-\frac{\Lambda}{H_C}\right) - \Lambda\Gamma\left(0, \frac{\Lambda}{H_C}\right)\right]$, where $\Gamma(a,z) = \int_z^\infty t^{a-1}e^{-t}dt$ [107] and Λ in this equation is the same as that used in the switching probability measurement. Here, we also set H_0 to H_K [106]. The results of fitting using this relation are shown as solid lines in Fig. 5.3b, and the results of the fitting follow the data well. Λ and τ_0, the switching attempt time constant estimated from the fitting, are also listed in Table 5.2. Fig. 5.3c and Table 5.2 show that the values of Λ and τ_0 obtained by the two different measurements are similar, and that the relative energy barrier is increased with the ultrathin Cu layer insertion.

The estimated τ_0 is too large because it is typically assumed to be approximately 1~10 ns [107,111]. In our sample, once the local reverse domain is nucleated, DW propagation instantly occurs and subsequently, the switching process is completed. Therefore, the local domain nucleation energy barrier has the most dominant influence on the switching field and switching barrier. Nevertheless, the switching characteristics are not only related to domain nucleation, but also related to DW depinning or propagation. Meanwhile local domain nucleation is predominantly related to the barrier. DW depinning or propagation may affect τ_0 [110,111], and may even be enough to change it by an order of magnitude [110]. Even so, the important point is the nucleation energy barrier and it is barely affected by τ_0.

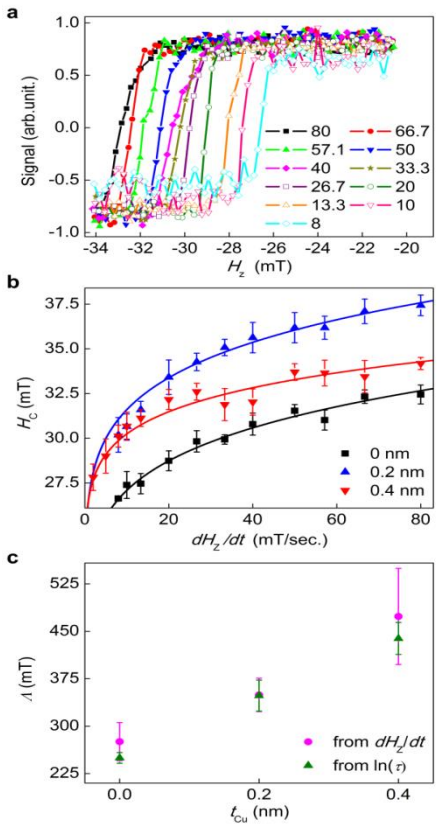

Figure 5.3 The relative energy barrier measurement with FIMS estimated by measurement of coercivity variance with different field sweep rates. a. The easy-axis hysteresis loops of a Cu 0 nm sample measured by MOKE. Each field sweep rate is denoted in the figure. The unit of sweep rate in (**a**) is mT/sec. **b.** The plot of H_C with respect to the field sweep rate. The symbols are measured data and the solid lines are the fitting lines. All black, blue, and red symbols and lines correspond to the data of Cu 0, 0.2, and 0.4 nm, respectively. The vertical error bars are the standard deviation of several repeated measurements. **c.** The relative energy barrier Λ with respect to Cu thickness. Data measured by different measuring methods are represented by two different colored symbols, the magenta circular symbols are from the coercivity measurement, and the green triangular symbols are from the switching probability measurement. The vertical error bars are from the fitting errors.

5.5 Measurement of current-induced magnetization switching

After FIMS measurements, the current-induced magnetization switching (CIMS) measurements were performed. We confirm that the switching current density can be reduced by the increase of DMI. The basic structure is a Pt/Co/Pt symmetric structure, and to facilitate the dramatic change of the DMI and to observe DMI-related physics, the SOT efficiency is not large, and a switching assist field was necessary in the CIMS process. The magnitude of the applied assist field was carefully set to prevent magnetic fields from playing a dominant role in the switching, and the probability of switching due to the assist field alone was estimated as less than 1%.

The measured switching current density J_{SW} is shown in Fig. 5.4a for the relative magnetic field magnitude with respect to H_{C}, i.e. $H_{\mathrm{Z}}/H_{\mathrm{C}}$. The total effective field, that is, the sum of the external magnetic field and the effective field generated by SOT causes switching, and therefore it is natural that the larger the $H_{\mathrm{Z}}/H_{\mathrm{C}}$, the smaller the J_{SW}. The important point is that the J_{SW} decreases as the Cu thickness increases. The J_{SW} is shown again in Fig. 5.4b with respect to $H_{\mathrm{DMI}}/H_{\mathrm{K}}$, and is seen to decrease when $H_{\mathrm{DMI}}/H_{\mathrm{K}}$ increases along with Cu thickness. As the current flows along the *x*-axis direction, the damping-like SOT τ_{DLT} generates the effective perpendicular magnetic field. This field is expressed as

the relation $H_{\mathrm{Z}}^{\mathrm{eff}} \propto \tau_{\mathrm{DLT}} m_x$, where m_x is the x-component of magnetization [22]. Therefore, $H_{\mathrm{Z}}^{\mathrm{eff}}$ is not only affected by the strength of the SOT, but also by the x-component of magnetization.

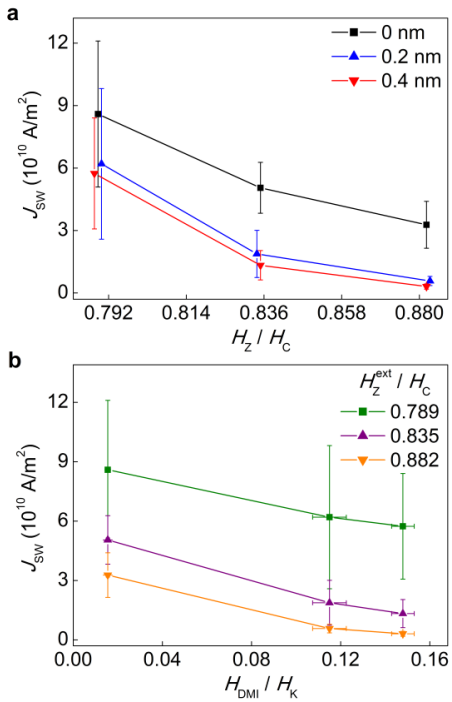

Figure 5.4 The switching current density with respect to Cu thickness. a. Plot of J_{SW} with respect to the relative external field ratio $H_{\mathrm{Z}}^{\mathrm{ext}}/H_{\mathrm{C}}$ with Cu thickness. **b.** Plot of J_{SW} with respect to the $H_{\mathrm{DMI}}/H_{\mathrm{K}}$ with the $H_{\mathrm{Z}}^{\mathrm{ext}}/H_{\mathrm{C}}$. All data corresponds to Cu 0, 0.2 and 0.4 nm from the left-hand symbols to the right-hand ones. In (a) and (b), the vertical error bars are the standard deviation of several repeated measurements.

Unlike the magnetization inside the sample, the magnetization at the sample edge can be tilted by the DMI [73,103,104]. The tilting angle θ_{DMI} caused at the

edge by the DMI, from the z-axis, is expressed as $\sin\theta_{\mathrm{DMI}} = \pm\frac{D\lambda}{2A_{\mathrm{ex}}} = \pm\frac{H_{\mathrm{DMI}}}{H_{\mathrm{K}}} = m_x$, where the sign depends on the sign of the DMI, and this tilting of magnetization causes it to exhibit an m_x component at the edge [104]. Therefore, the $H_{\mathrm{Z}}^{\mathrm{eff}}$ by SOT may be induced only at the edges, and the sample will be switched via nucleation at this edge. It is possible to produce the same magnitude of $H_{\mathrm{Z}}^{\mathrm{eff}}$ needed to generate the switching from a smaller current density when $H_{\mathrm{DMI}}/H_{\mathrm{K}}$ becomes large with ultrathin Cu insertion. The J_{SW} is almost linearly decreased in Fig. 5.4b, possibly because $H_{\mathrm{Z}}^{\mathrm{eff}}$ increases in proportion to $H_{\mathrm{DMI}}/H_{\mathrm{K}}$, that is, $H_{\mathrm{Z}}^{\mathrm{eff}} \propto \tau_{\mathrm{DLT}} m_x \propto H_{\mathrm{DMI}}/H_{\mathrm{K}}$ for the same magnitude of current density and external assist field.

The most significant result of this experiment is that both the thermal stability and domain nucleation energy barrier, in the case without switching current, can be increased while simultaneously reducing the switching current density by ultrathin Cu insertion. As previously explained, typically a larger energy barrier leads not only to higher stability, but also to larger magnetic fields or currents for switching. However, by DMI engineering with edge nucleation, it is possible to improve the stability when no current is applied, and to increase the switching efficiency through the current simultaneously, as our results show.

5.6 Estimation of thermal effect generated by current

We have confirmed two problems that occur due to the thermal effects of Joule heating on the switching process. The first problem is the question of whether the

reason behind the decrease of J_{SW} is the thermal effects that make magnetization switching easier. The thermal coefficient of electric resistance was measured to estimate the temperature increase due to the current. The resistance was measured by changing the temperature and current density, where the electrical resistance has a relationship of $R(T) = R_0[1 + \alpha(T - T_0)]$ to the temperature, and $R(J) = R_0/[1 - \beta J^2] = \beta J^2/[\alpha(1 - \beta J^2)]$ to the current [114]. The relative resistance ratios measured show linear and quadratic behavior depending on the temperature and current density, respectively (Fig. 5.5a).

From the measurements, the estimated values of coefficients were found to be $\alpha = 1.08 \pm 0.0019 \times 10^{-3}\ \mathrm{K}^{-1}$ and $\beta = 2.18 \pm 0.016 \times 10^{-24}\ \mathrm{m}^4/\mathrm{A}^2$. The maximum current density induced in the sample and the estimated maximum temperature increases from room temperature are approximately $1 \times 10^{11}\ \mathrm{A/m^2}$ and 21 K for the Cu 0 nm sample, and approximately $8 \times 10^{10}\ \mathrm{A/m^2}$ and 13 K for the Cu 0.2 and 0.4 nm samples in our experiments. These temperature increases are not negligible during some measurements, but do not affect switching significantly. Besides, the J_{SW} is larger in the Cu 0 nm sample than in the Cu 0.2 and 0.4 nm samples, even though the switching assist by Joule heating will be greater in the Cu 0 nm sample. Therefore, the J_{SW} decrease by DMI will be dominant in our experiments.

The second question is whether the domain phase is changed due to the temperature increase. This was confirmed by the domain observation via MOKE microscopy and VSM (Fig. 5.5b). The hysteresis loops were nearly square when the temperature was below approximately 360 K, which means that the reverse domains

are predominantly nucleated when an external field and current are induced in that temperature range and finite time scale. The reverse domain was large, even at approximately 350 K, and domain wall propagation occurred at this temperature. Conversely, spontaneous domain nucleation without external magnetic field and current occurred at temperatures higher than approximately 360 K. The maximum temperature in our samples during current induction was lower than approximately 320 K, so the case of spontaneous domain nucleation by Joule heating rather than local domain nucleation by the magnetic field and SOT is not seen in our results.

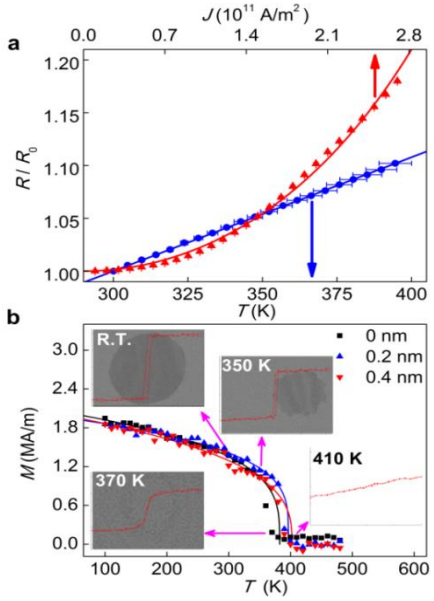

Figure 5.5 Estimation of thermal effects by current. a. Plot of relative electric resistance R/R_0 with respect to temperature T (lower label and blue symbols) and current density J (upper label and red symbols). The error bars are the standard deviation of several repeated measurements. The red and blue lines are linear and quadratic fitting lines, respectively. **b.** The magnetization M with respect to the temperature. The solid symbols are the measured data and the curved solid lines are eye guides. In the insets, domain images obtained by MOKE microscopy are presented with the easy-axis hysteresis loops obtained by VSM for each temperature. Above approximately 380 K, no domains were observed.

5.7 Conclusion

We demonstrate the effects of Cu insertion and the variation of the DMI strength on the magnetization switching. By ultrathin Cu insertion, the magnetic

anisotropy energy and strength of DMI are significantly increased, enhancing the thermal stability and decreasing the switching current density. Therefore, it is possible to achieve an increase of both thermal stability and switching efficiency simultaneously, by DMI engineering with ultrathin Cu insertions, providing effective means of designing sample structures for spintronic applications.

t_{Cu} **[nm]**	M_S [MA/m]	$\mu_0 H_K$ [T]	K_U^{eff} [10^6 J/m^3]	$\mu_0 H_{DMI}$ [mT]	ε_0 [mJ/m^2]
0	1.43±0.078	1.56±0.0043	1.12±0.0031	-24.19±1.23	4.15±0.060
0.2	1.48±0.095	2.44±0.0051	1.81±0.0038	-280.53±19.08	3.43±0.23
0.4	1.42±0.089	2.60±0.0046	1.84±0.0033	-384.54±13.89	3.47±0.17

Table 5.1 Measured magnetic properties of the Pt/Co/Cu/Pt samples.

Measurement	t_{Cu} [nm]	Λ [mT]	τ_0 [sec.]
Switching Probability	0	249.69±8.48	$(1.86\pm2.41)\times10^{-5}$
	0.2	348.18±24.55	$(1.86\pm3.74)\times10^{-6}$
	0.4	438.63±25.27	$(8.69\pm17.22)\times10^{-8}$
Coercivity Variance	0	275.43±30.17	$(1.49\pm1.53)\times10^{-5}$
	0.2	349.33±26.40	$(6.44\pm5.01)\times10^{-6}$
	0.4	473.52±76.04	$(4.73\pm1.13)\times10^{-8}$

Table 5.2 Estimated relative energy barriers and the attempt time constants of Pt/Co/Cu/Pt samples with different measurement methods.

Chapter 6

Outlook

In this thesis, we identified the tendencies of the DMI with non-magnetic layer materials and with ferromagnetic and non-magnetic layer thicknesses in trilayer systems. The underlying physics and assumptions required for interpretation of the results for all experiments are based on the fact that the DMI is affected by conduction electrons in metallic systems. As a result, we obtained experimental results that could not be sufficiently understood on the assumption that the DMI is simply interfacial effects. With our results, we would like to suggest further research points and promising experiments.

The first suggestion relates to the control of the DMI through electric field control at the interface. The work function difference at Co/X is linked to the electric field and charge distribution near the interface. Unfortunately, with metallic materials made of X, the built-in electric field near the Co/X interface is difficult to change with external stimuli such as voltage. Therefore, a structure such as Pt/Co/Oxide is more suitable for controlling the DMI. Moreover, because oxides have a lot of potential to change their properties with different combinations of materials, various trials will be able to produce samples that allow more efficient DMI control. Furthermore, the study of the DMI by inserting a very thin layer at the Co/Oxide interface may represent a good way to control the DMI by electric field induction [115-117].

The second suggestion is the question of whether the contribution of the sub-atomic layer to the DMI is adjustable with external stimuli. If possible, the ferromagnetic layer thickness at which the DMI has a maximum value will vary. Moreover, in such cases, the tendency of the DMI variation through external stimuli such as an external electric field may also vary depending on the ferromagnetic layer thickness.

The third suggestion is to conduct the DMI oscillation experiments performed in this thesis using another material such as alloy, or multilayer stack as the QW layer, as suggested in Chapter 4. Cu is a good material for observing QW characteristic behavior, but is not good for the strength of the SOT because Cu has been known to have negligible spin Hall angle compared with Pt or W [118,119]. If a material that is capable of generating a large SOT and exhibiting obvious QW characteristic behaviors is used as the QW layer, samples with large SOTs and easy DMI controls will result.

The fourth suggestion is to conduct DMI oscillation experiments with a change of reflecting layer conditions or materials, as suggested in Chapter 4. Examples of such changes of the reflecting layer conditions are those of the alloying of metal ions in oxide, and the controlling of the oxidation state and interface electric field by adjusting oxidation conditions or applying external electric fields. If the DMI changes sufficiently with these elements and with the appropriate patterning processes, the change of the DMI in local areas or positions may be possible. Such a change could give a more versatile functionality to magnetic devices such as DW, or skyrmion-based racetracks.

The fifth suggestion is the use of appropriate materials such as W in DMI engineering, to reduce the switching current. In this thesis, the Pt/Co/Pt structure is used for the basic structure so as to observe the physical effects of DMI for magnetization switching phenomena more clearly. However, for device applications, a Pt/Co/Pt structure may not be so useful. The effects of Cu layer insertion on other sample structures may be similar to those we have seen in this experiment. Therefore, the ultrathin Cu insertion on a larger SOT sample will be beneficial. In this regard, structures such as Pt/Co/Cu/W with ultrathin Cu layer are more appropriate for device applications.

The last suggestion is to engineer the H_{K} at the edge of the dot structure. If H_{K} is reduced at the edges within the limit of maintaining domain nucleation stability, it may be possible to reduce the switching current density by increasing the ratio of $H_{\mathrm{DMI}}/H_{\mathrm{K}}$.

References

1. R. Jungblut, M.T. Johnson, J. Stegge, A. Reinders, and F.J.A. Broeder, Orientational and structural dependence of magnetic anisotropy of Cu/Ni/Cu sandwiches: Misfit interface anisotropy, *J. Appl. Phys*. **75**, 6424 (1994).
2. P. Bruno, and J.-P. Renard, Magnetic surface anisotropy of transition metal ultrathin films, *Appl. Phys. A*. **49**, 499-506 (1989).
3. S. Bandiera, R.C. Sousa, B. Rodmacq, and B. Dieny, Asymmetric interfacial perpendicular magnetic anisotropy in Pt/Co/Pt trilayers, *IEEE Magn. Lett*. **2**, 3000504 (2011).
4. P.F. Carcia, Z.G. Li, and W.B. Zeper, Effect of sputter-deposition processes on the microstructure and magnetic properties of Pt/Co multilayers, *J. Magn. Magn. Mater*. **121**, 452-460 (1993).
5. P.F. Carcia, M. Reilly, and Z.G. Li, Ar-sputtered Pt/Co multilayers with large anisotropy energy and coercivity, *IEEE Trans. Magn*. **30**, 4395-4397 (1994).
6. C.L. Canedy, X.W. Li, and G. Xiao, Extraordinary Hall effect in (111) and (100) orientated Co/Pt superlattices, *J. Appl. Phys*. **81**, 5367 (1997).
7. H.-S. Whang, S.-J. Yun, J. Moon, and S.-B. Choe, Optical measurement of magnetic anisotropy field in nanostructured ferromagnetic thin films, *J. Magn*. **20(1)**, 8-10 (2015).
8. S. Okamoto, K. Nishiyama, O. Kitakami, and Y. Shimada, Enhancement of magnetic surface anisotropy of Pd/Co/Pd trilayers by the addition of Sm, *J. Appl.*

Phys. **90**, 4085 (2001).

9. S. Okamoto *et al*. Chemical-order-dependent magnetic anisotropy and exchange stiffness constant of FePt (001) epitaxial films, *Phys. Rev. B.* **66**, 024413 (2002).
10. I. Dzyaloshinsky, A thermodynamics theory of weak ferromagnetism of antiferromagnetics, *J. Phys. Chem. Solid*. **4**, 241-255 (1958).
11. T. Moriya, Anisotropic superexchange interaction and weak ferromagnetism, *Phys. Rev.* **120**, 91-98 (1960).].
12. A. Fert, and P.M. Levy, Role of anisotropic exchange interactions in determining the properties of spin-glasses, *Phys. Rev. Lett*. **44**, 1538-1541 (1980).
13. K.-W. Kim, H.-W. Lee, K.-J. Lee, and M.D. Stiles, Chirality from interfacial spin-orbit coupling effects in magnetic bilayers, *Phys. Rev. Lett.* **111**, 216601 (2013).
14. A. Kundu, and S. Zhang, Dzyaloshinskii-Moriya interaction mediated by spin-polarized band with Rashba spin-orbit coupling, *Phys. Rev. B*. **92**, 094434 (2015).
15. H. Imamura, P. Bruno, and Y. Utsumi, Twisted exchange interaction between localized spins embedded in a one- or two-dimensional electron gas with Rashba spin-orbit coupling, *Phys. Rev. B*, **69**, 121303(R) (2004).
16. A.A. Khajetoorians *et al*. Tailoring the chiral magnetic interaction between two individual atoms, *Nat. Commun*. **7**, 10620 (2016).
17. S. Kim *et al*. Correlation of the Dzyaloshinskii-Moriya interaction with Heisenberg exchange and orbital asphericity, *Nat. Commun*, **9**, 1648 (2018).
18. L. Petersen, and P. Hedegård, A simple tight-binding model of spin-orbit splitting of *sp*-derived surface states, *Surf. Sci*. **459**, 49-56 (2000).

19. C. Nistor *et al*. Orbital moment anisotropy of Pt/Co/AlOx heterostructures with strong Rashba interaction, *Phys. Rev. B*. **84**, 054464 (2011).
20. A. Belabbes, G. Bihlmayer, S. Blügel, and A. Manchon, Oxygen-enabled control of Dzyaloshinskii-Moriya interaction in ultra-thin magnetic films, *Sci. Rep*. **6**, 24634 (2016).
21. A. Hoffmann, Spin Hall effects in metals, *IEEE Trans. Magn*. **49**, 5172–5193 (2013).
22. S. Emori, U. Bauer, S.-M. Ahn, E. Martinez, and G.S.D. Beach, Current-driven dynamics of chiral ferromagnetic domain walls, *Nat. Mater*. **12**, 611 (2013).
23. A. Thiaville, S. Rohart, É, Jué, V. Cros, and A. Fert, Dynamics of Dzyaloshinskii domain walls in ultrathin magnetic films. *Europhys. Lett*. **100**, 57002 (2012).
24. S.S.P. Parkin, and S.-H. Yang, Memory on the racetrack, *Nat. Nanotech*. **10**, 195-198 (2015).
25. A. Fert, V. Cros, and J. Sampaio, Skyrmions on the track, *Nat. Nanotech*. **8**, 152-156 (2013).
26. K.-S. Ryu, L. Thomas, S.-H. Yang, and S.S.P. Parkin, Chiral spin torque at magnetic domain walls, *Nat. Nanotech*. **8**, 527-533 (2013).
27. J. Sampaio, V. Cros, S. Rohart, A. Thiaville, and A. Fert, Nucleation, stability and current-induced motion of isolated magnetic skyrmions in nanostructures, *Nat. Nanotech*. **8**, 839-844 (2013).
28. J.-W. Yoo, S.-J. Lee, J.-H. Moon, and K.-J. Lee, Phase diagram of a single skyrmion on magnetic nanowires, *IEEE Trans. Magn*. **50**, 1500504 (2014).

29. S.-G. Je *et al*. Emergence of huge negative spin-transfer torque in atomically thin Co layers, *Phys. Rev. Lett.* **118**, 167205 (2017).

30. M. Wellhőfer, M. Weißenborn, R. Anton, S. Pütter, and H.P. Oepen, Morphology and magnetic properties of ECR ion beam sputtered Co/Pt films, *J. Magn. Magn. Mater*. **292**, 345-358 (2005).

31. P.P.J. Haazen *et al*. Domain wall depinning governed by the spin Hall effect, *Nat. Mater*. **12**, 299-303 (2013).

32. J. Yu, X. Qiu, W. Legrand, and H. Yang, Large spin-orbit torques in Pt/Co-Ni/W heterostructures, *Appl. Phys. Lett*. **109**, 042403 (2016).

33. S.-G. Je, *et al*. Asymmetric magnetic domain-wall motion by the Dzyalishinskii–Moriya interaction, *Phys. Rev. B* **88**, 214401 (2013).

34. J. Cho, *et al*. Thickness dependence of the interfacial Dzyaloshinskii-Moriya interaction in inversion symmetry broken systems, *Nat. Commum*. **6**, 7635 (2015).

35. G.K. Hall, and C.H.B. Mee, The surface potential of oxygen on iron, cobalt and manganese, *Surf. Sci*. **28**, 598-606 (1971).

36. H.B. Wahlin, Thermionic properties of the iron group, *Phys. Rev*. **61**, 509-512 (1942).

37. A.Y.-C. Yu and W.E. Spicer, Photoemission studies of the electronic structure of cobalt, *Phys. Rev*. **167**, 674-167 (1968).

38. H.B. Michaelson, The work function of the elements and its periodicity, *J. Appl. Phys*. **48**, 4729-4733 (1977).

39. A.B. Cardwell, The thermionic properties of tantalum, *Phys. Rev*. **47**, 628-630 (1935).

40. A. Kiejna, Surface atomic structure and energetics of tantalum, *Surf. Sci*. **598**, 276-284 (2005).

41. B.J. Hopkins, and J.C. Rivière, Work function values from contact potential difference measurements, *Brit. J. Appl. Phys*. **15**, 941-946 (1964).

42. C. Davisson, and L.H. Germer, The thermionic work function of tungsten, *Phys. Rev*. **20**, 300-330 (1922).

43. C.J. Todd, and T.N. Rhodin, Work function in field emission—The (110) plane of tungsten, *Surf. Sci*. **36**, 353-369 (1973).

44. D.R. Lide, *CRC Handbook of Chemistry and Physics*75th edn (CRC Press, Boca Raton, FL, USA, 1994).

45. E.W.J. Mitchell, and J.W. Mitchell, The work functions of copper, silver and aluminium, *Proc. Roy. Soc.* (London). **A210**, 70-84 (1951).

46. G.C. Smith, C. Norris, C. Binns, and H.A. Padmore, A photoemission study of ultra-thin palladium overlayers on low-index faces of silver, *J. Phys. C***15**, 6481-6496 (1982).

47. H. Kawano, Effective work functions for ionic and electronic emissions from mono- and polycrystalline surfaces, *Prog. Surf. Sci*. **83**, 1-165 (2008).

48. H. Shelton, Thermionic emission from a planar tantalum crystal, *Phys. Rev*. **107**, 1553-1557 (1957).

49. J.K. Grepstad, P.O. Gartland, and B.J. Slagsvold, Anisotropic work function of clean and smooth low-index faces of aluminium, *Surf. Sci*. **57**, 348-362 (1976).

50. L.A. Dubridge, and W.W. Roehr, Photoelectric and thermionic properties of palladium, *Phys. Rev*. **39**, 99-107 (1932).

51. M. Uda, A. Nakamura, T. Yamamoto, and Y. Fujimoto, Work function of polycrystalline Ag, Au and Al, *J. Electron Spectrosc. Relat. Phenom*. **88**, 643-648 (1998).

52. M. Camp, and S.M.A. Lecchini, The work function of polycrystalline tungsten foil, *Proc. Phys. Soc*. **85**, 815-817 (1965).

53. P.A. Anderson, The work function of copper, *Phys. Rev*. **76**, 388-390 (1949).

54. P.A. Anderson, Work function of gold, *Phys. Rev*. **115**, 553-554 (1959).

55. P.O. Gartland, S. Berge, and B.J. Slagsvold, Photoelectric work function of a copper single crystal for the (100), (110), (111), and (112) faces, *Phys. Rev. Lett*. **28**, 738-739 (1972).

56. R. Bouwman, and W.M.H. Sachtler, Photoelectric determination of the work function of gold–platinum alloys, *J. Catal*. **19**, 127-140 (1970).

57. R.J. D'Arcy, and N.A. Surplice, Work function of titanium films, *Surf. Sci*. **36**, 783-788 (1973).

58. R.M. Eastment, and C.H.B. Mee, Work function measurements on (100), (110) and (111) surfaces of aluminium, *J. Phys. F***3**, 1738-1745 (1973).

59. J.E. Huheey, E.A. Keiter, and R.L. Keiter, *Inorganic Chemistry* 4th edn (HarperCollins College Publishers, NY, USA, 1993).

60. M. Montalti, A. Credi, L. Prodi, and M.T. Gandofi, *Handbook of Photochemistry* 3rd edn (CRC Press, Boca Raton, FL, USA, 2006).

61. P.J. Metaxas *et al*. Creep and flow regimes of magnetic domain-wall motion in ultrathin Pt/Co/Pt films with perpendicular anisotropy, *Phys. Rev. Lett*. **99**, 217208 (2007).

62. S. Emori *et al*. Spin Hall torque magnetometry of Dzyaloshinskii domain walls, *Phys. Rev. B.* **90**, 184427 (2014).

63. R. Lavrijsen *et al*. Asymmetric magnetic bubble expansion under in-plane field in Pt/Co/Pt: Effect of interface engineering, *Phys. Rev. B***91**, 104414 (2015).

64. Y. Guan, T. Koyama, and D. Chiba, Current-induced magnetic domain wall motion in Pt/Co/Pd and Pd/Co/Pt structures with opposite sign of Dzyaloshinskii-Moriya interaction, *AIP Adv*. **7**, 085123 (2017).

65. F. Ajejas *et al*. Tuning domain wall velocity with Dzyaloshinskii-Moriya interaction, *Appl. Phys. Lett*. **111**, 202402 (2017).

66. J. Cho *et al*. The sign of the interfacial Dzyaloshinskii-Moriya interaction in ultrathin amorphous and polycrystalline magnetic films, *J. Phys. D*. **50**, 425004 (2017).

67. A. Belabbes, G. Bihlmayer, F. Bechstedt, S. Blügel, and A. Manchon, Hund's rule-driven Dzyaloshinskii-Moriya interaction ad 3d-5d interfaces, *Phys. Rev. Lett*. **117**, 247202 (2016).

68. H. Yang, A. Thiaville, S. Rohart, A. Fert, and M. Chshiev, Anatomy of Dzyalishinskii–Moriya interaction at Co/Pt interfaces, *Phys. Rev. Lett*. **115**, 267210 (2015).

69. S. Woo *et al*. Current-driven dynamics and inhibition of the skyrmion Hall effect of ferromagnetic skyrmions in GdFeCo films. *Nat. Commun*. **9**, 959 (2018).

70. A. Soumyanarayanan, N. Reyren, A. Fert, and C. Panagopoulos, Emergent phenomena induced by spin-orbit coupling at surfaces and interfaces. *Nature*, **539**, 509–517 (2016).

71. A.K. Chaurasiya *et al*. Direct observation of interfacial Dzyaloshinskii-Moriya interaction from asymmetric spin-wave propagation in W/CoFeB/SiO_2 heterostructures down to sub-nanometer CoFeB thickness. *Sci. Rep*. **6**, 32592 (2016).

72. N.-H. Kim *et al*. Interfacial Dzyaloshinskii-Moriya interaction, surface anisotropy energy, and spin pumping at spin orbit coupled Ir/Co interface. *Appl. Phys. Lett*. **108**, 142406 (2016).

73. D.-S. Han *et al*. Asymmetric hysteresis for probing Dzyaloshinskii-Moriya interaction. *Nano Lett.* **16**, 4438-4446 (2016).

74. H. Jia, B. Zimmermann, and S. Blügel, First-principles investigation of chiral magnetic properties in multilayers: Rh/Co/Pt and Pd/Co/Pt. *Phys. Rev. B.* **98**, 144427 (2018).

75. J.H. Franken, M. Herps, H.J.M. Swagten, and B. Koopmans, Tunable chiral spin texture in magnetic domain-walls. *Sci. Rep*. **4**, 5248 (2014).

76. I.M. Miron *et al*. Current-driven spin torque induced by the Rashba effect in a ferromagnetic metal layer, *Nat. Mater*. **9**, 230-234 (2010).

77. S. Bandiera, R.C. Sousa, B. Rodmacq, and B. Dieny, Enhancement of perpendicular magnetic anisotropy through reduction of Co-Pt interdiffusion in (Co/Pt) multilayers. *Appl. Phys. Lett*. **100**, 142410 (2012).

78. P. Varga, E. Lundgren, J. Redinger, and M. Schmid, Ultrathin films of Co on Pt(111): an STM view. *Phys. Status Solidi A*, **187**, 97 (2001).

79. K. Oikawa *et al*. Direct observation of magnetically induced phase separation in Co-W sputtered thin films, *Appl. Phys. Lett*. **85**, 2559 (2004).

80. G. Ö stberg, B. Jansson, and H. Andrén, On spinodal decomposition in Co-W system, *Scr. Mater*. **54**, 595-598 (2006).

81. F. Hellman *et al*. Interface-induced phenomena in magnetism, *Rev. Mod. Phys*. **89**, 025006 (2017).

82. J.E. Ortega, F.J. Himpsel, G.J. Mankey, and R.F. Willis, Quantum-well states and magnetic coupling between ferromagnets through a noble-metal layer, *Phys. Rev. B*. **47**, 1540 (1993).

83. F.J. Himpsel, Magnetic quantum wells, *J. Phys. Condens. Matter*, **11**, 9483-9494 (1999).

84. C. Rüdt, A. Scherz, and K. Baberschke, Oscillatory Curie temperature in ultrathin ferromagnets: experimental evidence, *J. Magn. Magn. Mater*. **285**, 95-100 (2005).

85. P. Bruno, J. Kudrnovský, M. Pajda, V. Drchal, and I. Turek, Oscillatory Curie temperature of 2-D ferromagnets, *J. Magn. Magn. Mater*. **240**, 246-248 (2002).

86. S. Yakata, Y. Ando, T. Miyazaki, and S. Mizukami, Temperature Dependences of Spin-Diffusion Lengths of Cu and Ru layers, *Jpn. J. Appl. Phys*. **45**, 3892 (2006).

87. A. Arrott, Criterion for Ferromagnetism from Observations of Magnetic Isotherms, *Phys. Rev.* **108**, 1394 (1957).

88. C. Kittel, *Introduction to Solid State Physics* 8th edn (Wiley, New York, USA, 2004).

89. D. Chiba *et al*. Electrical control of the ferromagnetic phase transition on cobalt at room temperature, *Nat. Mater*. **10**, 853-856 (2011).

90. S.S.P. Parkin, R. Bhadra, and K.P. Roche, Oscillatory Magnetic Exchange Coupling through Thin Copper Layers, *Phys. Rev. Lett*. **66**, 2152 (1991).

91. M. Matczak *et al*. Antiferromagnetic magnetostatic coupling in Co/Au/Co films with perpendicular anisotropy, *J. Appl. Phys*. **114**, 093911 (2013).

92. Z.Y. Liu *et al*. Antiferromagnetic interlayer coupling in Pt/Co multilayers with perpendicular anisotropy, *Phys. Rev. B*. **79**, 024427 (2009).

93. D. Roundy, C.R. Krenn, M.L. Cohen, and J.W. Morris, Jr., Ideal Shear Strengths of fcc Aluminum and Copper, *Phys. Rev. Lett*. **82**, 2713 (1999).

94. C. Li, A.J. Freeman, and C.L. Fu, Electronic structure and surface magnetism of fcc Co(001), *J. Magn. Magn. Mater*. **75**, 53-60 (1988).

95. M.D. Stiles, Exchange coupling in magnetic heterostructures, *Phys. Rev. B*. **48**, 7238 (1993).

96. S. Yuasa, T. Nagahama, and Y. Suzuki, Spin-Polarized Resonant Tunneling in Magnetic Tunnel Junctions, *Science*, **297**, 234-237 (2002).

97. U. Ebels *et al*. Induced phase shift in interlayer magnetic exchange coupling: Magnetic layer doping, *Phys. Rev. B*. **58**, 6367 (1998).

98. J.C. Slonczewski, Current-driven excitation of magnetic multilayers, *J. Magn. Magn. Mater*. **159**, L1-L7 (1996).

99. S. Fukami, and H. Ohno, Magnetization switching schemes for nanoscale three-terminal spintronics devices, *Jpn. J. Appl. Phys*. **56**, 0802A1 (2017).

100. J. Ryu, S.-B. Choe, and H.-W. Lee, Magnetic domain-wall motion in nanowire: Depinning and creep, *Phys. Rev. B*. **84**, 075469 (2011).

101. A. Manchon *et al*. Current-induced spin-orbit torques in ferromagnetic and antiferromagnetic systems, *Rev. Mod. Phys*. **91**, 035004 (2019).

102. J. Hayakawa *et al*. Current-Induced Magnetization Switching in MgO Barrier Based Magnetic Tunnel Junctions with CoFeB/Ru/CoFeB Synthetic Ferrimagnetic Free Layer, *Jpn. J. Appl. Phys*. **45**, L1057-L1060 (2006).

103. N. Mikuszeit *et al*. Spin-orbit torque driven chiral magnetization reversal in ultrathin nanostructures, *Phys. Rev. B*. **92**, 144424 (2015).

104. S. Pizzini *et al.* Chirality-Induced Asymmetric Magnetic Nucleation in Pt/Co/AlO_x Ultrathin Microstructures, *Phys. Rev. Lett*. **113**, 047203 (2014).

105. P.-H. Jang, K. Song, S.-J. Lee, S.-W. Lee, and K.-J. Lee, Detrimental effect of interfacial Dzyaloshinskii-Moriya interaction on perpendicular spin-transfer-torque magnetic random access memory, *Appl. Phys. Lett*. **107**, 202401 (2015).

106. B. Barbara, Magnetization processes in high anisotropy systems, *J. Magn. Magn. Mater*. **129**, 79-86 (1994).

107. J. Moritz *et al*. Experimental evidence of a 1/*H* activation law in nanostructures with perpendicular magnetic anisotropy, *Phys. Rev. B*. **71**, 100402(R) (2005).

108. E. C. Stoner and E. P. Wohlfarth, A mechanism of magnetic hysteresis in heterogeneous alloys, *Philos. Trans. R. Soc*. **240**, 599 (1948).

109. F. Schumacher, On the modification of the Kondorsky function, *J. Appl. Phys*. **70**, 3184 (1991).

110. S. Krause *et al*. Magnetization Reversal of Nanoscale Islands: How Size and Shape Affect the Arrhenius Prefactor, *Phys. Rev. Lett*. **103**, 127202 (2009).

111. W. Wernsdorfer *et al*. Nucleation of Magnetization Reversal in Individual Nanosized Nickel Wires, *Phys. Rev. Lett*. **77**, 1873 (1996).

112. A. Lyberatos and R.W. Chantrell, The fluctuation field of ferromagnetic materials, *J. Phys. Condens. Matter*, **9**, 2623 (1997).

113. S. Lemerle *et al*. Domain Wall Creep in an Ising Ultrathin Magnetic Film, *Phys. Rev. Lett*. **80**, 849 (1998).

114. K.-J. Kim, J.-C. Lee, S.-B. Choe, and K.-H. Shin, Joule heating in ferromagnetic nanowires: Prediction and observation, *Appl. Phys. Lett*. **92**, 192509 (2008).

115. Y. Hibino *et al*. Electric field modulation of magnetic anisotropy in perpendicularly magnetized Pt/Co structure with a Pd top layer, *Appl. Phys. Exp*. **8**, 113002 (2015).

116. Y. Jibiki *et al.* Interface resonance in Fe/Pt/MgO multilayer structure with large voltage controlled magnetic anisotropy change, *Appl. Phys. Lett*. **114**, 082405 (2019).

117. K. Nawaoka, S. Miwa, Y. Shiota, N. Mizuochi, and Y. Suzuki, Voltage induction of interfacial Dzyaloshinskii-Moriya interaction in Au/Fe/MgO artificial multilayer, *Appl. Phys. Exp*. **8**, 063004 (2015).

118. H.L. Wang *et al*. Scaling of Spin Hall Angle in 3d, 4d, and 5d Metals from $Y_3Fe_5O_{12}$/Metal Spin Pumping, *Phys. Rev. Lett*. **112**, 197201 (2014).

119. C. Du, H. Wang, F. Yang, and P.C. Hammel, Systematic variation of spin-orbit coupling with *d*-orbital filling: Large inverse spin Hall effect in 3*d* transition metals, *Phys. Rev. B*. **90**, 140407(R) (2014).

Abstract in Korean

반전 대칭성이 깨진 자성 박막 구조에서 스핀들의 chiral 구조를 발현시켜주는 역할 때문에 Dzyaloshinskii-Moriya 상호작용(DMI)에 대한 연구가 활발하게 진행되고 있다. 충분히 큰 DMI 는 자구벽이 특정한 chirality 를 가지게 하는데, 이는 스핀 궤도 토크 (SOT)에 의한 자구벽 이동에서 중요한 요소이다. 그리고 DMI 가 클수록 자구벽 이동 속도의 최대값이 증가하는 것으로 알려졌다. 더욱이, 충분히 큰 DMI 는 magnetic skyrmion 이 만들어지는 데 중요한 역할을 하는데, 이것은 racetrack memory 나 논리소자로 응용될 수 있다. 그러므로, DMI 제어 역시 이 분야에서 중요하다.

DMI 에 대한 초기 연구는 I. Dzyaloshinskii 와 T. Moriya 에 의해 1960 년에 제시된 three-site atomic super-exchange interaction 으로 반강자성 산화물에서 수행되었다. 이후 A. Fert 와 P.M. Levy 가 1980 년에 spin-orbit scattering 으로 금속 물질에서 conduction-electron-mediated DMI 메커니즘이 제시되고부터, DMI 가 conduction-electron-mediated 현상과 관련이 있음을 보여주는 연구들이 최근에 진행되고 있다. 따라서 DMI 에 대한 더 깊은 연구들이 진행되었지만, 여전히 DMI 의 정확한 메커니즘이나 DMI 에 가장 결정적인 파라메터가 무엇인지에 대해서는 논란이 있다.

자성 다층 박막에서 DMI 에 대해 가장 널리 받아들여지는 개념은 DMI 가 계면효과라는 점이다. 그러므로 DMI 에 대한 연구는 주로 계면 상태 쪽으로 집중되었고, 따라서 DMI 를 극대화시키는 시도들은 주로 계면 상태를 바꾸어주거나 계면을 이루는 물질을 바꾸는 식으로 진행되었다. 하지만, 만약 DMI 가 온전히 계면 효과로만 이해되며 또한 그런 경향을 보인다면, DMI 를 제어하는 데는 제한된 방법 밖에 없을 것인데, DMI 크기는 오로지 계면에서만 정해지며, 그 계면은 오직 2 개뿐이기 때문이다. 게다가, DMI 는 spin-orbit coupling (SOC) 세기에 비례하는 것으로 알려져 있어서, SOC 가 큰 것으로 알려진 일부 중금속에 대해서만 주로 DMI 가 연구되고 있다.

우리는 DMI 에 대한 이해를 증진시키고 앞의 한계들을 극복하며 DMI 를 제어하는 새로운 방향을 제시하기 위한 연구들을 진행했다. Chapter 1 에서, 본 연구와 연관된 기본적인 자성 물리, 알려진 DMI 메커니즘, 그리고 DMI 측정법에 대해 설명하였다. 모든 chapter 에서 사용한 DMI 측정방법은 동일하므로, 자세한 DMI 측정 방법은 chapter 1 에서 설명하며 각 chapter 에서의 DMI 측정은 간단하게만 설명하였다. Chapter 1 이후, trilayer 구조의 샘플에서 각 요소들을 바꾸어주며 DMI 연구를 진행했다. Chapter 2, 3, 4 에서 DMI 의 비자성물질 의존성, 자성층 두께 의존성, 그리고 비자성층 두께 의존성을 각각 연구한 결과를 제시했다. Chapter 2, 3, 4 는 주로 DMI 의 물리적인 부분에 대한 연구인

반면, Chapter 5 는 DMI 제어를 통한 효율적 자성 소자 동작을 위한 응용 연구이다.

Chapter 2 에서, Pt/Co/X trilayer 샘플에서 DMI 에 가장 결정적인 파라메터로써 일함수를 발견했다. 그리고 DMI 와 일함수의 연관관계에 대한 메커니즘 등에 대한 논의를 진행했다. Chapter 2 이후로는, 대부분의 연구는 Pt/Co/W, Pt/Co/Cu trilayer 구조에 대해 집중적으로 연구를 진행했다.

Chapter 3 에서, Pt/Co/W, Pt/Co/Cu/W trilayer 구조에서 DMI 의 Co 두께 경향이 자성층 두께의 반비례성에서 벗어나는 점을 보였다. 보통 DMI 는 자성층 두께의 반비례 의존성을 보이는 것으로 예상되지만, 우리는 실험으로 DMI 의 완전한 발현에는 자성층의 critical thickness 가 존재함을 발견했다. DMI 의 경우와는 다르게, SOT 의 경우 전 Co 두께 영역에서 자성층 두께의 반비례 의존성을 보임을 확인했다. DMI 와 SOT 의 이런 차이점으로부터 계면 효과로 알려진 현상은 실제로 그 현상의 기원에 따라 구체적인 자성층 두께 경향이 달라질 수 있음을 알 수 있다.

Chapter 4 에서, Pt/Co/Cu trilayer 구조에서 Cu 두께가 증가함에 따라 DMI oscillation 함을 발견했다. 이 oscillation 주기를 Cu 의 박막 성장 방향과 더불어 양자 우물 효과와도 연관된 다른 현상인 Ruderman-Kittel-Kasuya-Yosida (RKKY) 상호작용과 비교를 하기 위해,

Co/Cu/(Pt)/Co 스핀 벨브 구조에서 RKKY 상호작용의 측정도 진행했다. 이로부터, DMI oscillation 은 Cu 층 내부의 양자 우물 현상과 관련이 있음을 추론하였다.

Chapter 5 에서, 샘플의 열적 안정성의 향상과 자화 반전 전류의 감소를 동시에 실현하는 시도를 진행했다. 보통 이 둘을 동시에 달성하는 것은 어려운 것으로 알려져있는데, Pt/Co/Pt trilayer 샘플에서 Co/Pt 계면에 Cu 를 아주 얇게 삽입하여 이 둘을 동시에 실현할 수 있음을 보였다. Cu 층 삽입의 가장 중요한 결과는 PMA 크기와 DMI 크기의 동시적인 증가이다. PMA 크기의 증가는 주로 열적 안정성의 증대로 연결되고, DMI 크기의 증가는 주로 자화 반전 전류 감소로 연결됨을 보였다.

Chapter 6 에서, 학위 기간 동안 연구한 결과들로부터의 전망을 제시했다. DMI 가 conduction electron-mediated 현상과 관련이 있다는 점을 기반으로 한 우리의 주요한 발견은 다층 자성 박막에서 DMI 에 대한 이해를 증진시키며, 그리고 기존 방법들의 한계들을 극복하여 DMI 를 제어하는 새로운 방향을 제시하였다.

Author's Biography

Yong-Keun Park

1. Department of Physics and Astronomy, Seoul National University
Gwanak-Ro 1, Gwanak-Gu, Seoul 08826, Republic of Korea
Tel : +82-2-884-9254 | E-mail : pyk071865@naver.com

2. Center for Spintronics, Korea Institute of Science and Technology
Hawolgok-dong 39-1, Seongbuk-Gu, Seoul 02792, Republic of Korea

Education

2008-2014 B.S. in Physics
Department of Physics, Inha University
Graduation with Summa Cum Laude

2014-2020 Ph.D. in Physics
Department of Physics and Astronomy, Seoul National University

Research Interest

Spin-orbit coupling-related phenomena
(Dzyaloshinskii-Moriya Interaction, Spin Hall effect)

Spin orbit torque
Magnetic domain wall motion

Skills

Magnetic film & oxide film fabrication
Photo-Lithography & E-Beam Lithography
Dry etch process
Electrical measurement of MR
Labview
Mathematica
Matlab

Publication List

1. Soong-Geun Je, Sang-Cheol Yoo, Joo-Sung Kim, ***Yong-Keun Park***, Min-Ho Park, Joon Moon, Byoung-Chul Min, and Sug-Bong Choe, "Emergence of Huge Negative Spin-Transfer Torque in Atomically Thin Co Layers" *Phys. Rev. Lett.* **118**, 167205 (2017).

2. Joo-Sung Kim, Yune-Seok Nam, Dae-Yun Kim, ***Yong-Keun Park***, Min-Ho Park, and Sug-Bong Choe, "Comparison between spin-orbit torques measured by domain-wall motions and harmonic measurements" *AIP Advances* **8**, 056009 (2018).

3. Dae-Yun Kim, Min-Ho Park, ***Yong-Keun Park***, Joo-Sung Kim, Yune-Seok Nam, Hyeok-Cheol Choi, Duck-Ho Kim, Soong-Geun Je, Byoung-Chul Min, and Sug-Bong Choe, "Chirality-induced antisymmety in domain-wall speed" *NPG Asia Materials* **10**, e464 (2018).

4. Dae-Yun Kim, Min-Ho Park, ***Yong-Keun Park***, Ji-Sung Yu, Joo-Sung Kim, Duck-Ho Kim, Byoung-Chul Min, and Sug-Bong Choe, "Huge domain-wall speed variation with respect to ferromagnetic layer thickness in ferromagnetic Pt/Co/TiO_2/Pt films" *Appl. Phys. Lett*. **112**, 062406 (2018).

5. Dae-Yun Kim, Min-Ho Park, ***Yong-Keun Park***, Joo-Sung Kim, Yoon-Seok Nam, Hyun-Seok Hwang, Duck-Ho Kim, Soong-Geun Je, Byoung-Chul Min, and Sug-Bong Choe, "Magnetic domain-wall tilting due to domain-wall speed asymmetry" *Phys. Rev. B.* **97**, 134407 (2018).

6. Yune-Seok Nam, Dae-Yun Kim, Min-Ho Park, ***Yong-Keun Park***, Joo-Sung Kim, Duck-Ho Kim, Byoung-Chul Min, and Sug-Bong Choe, "Distinct stochasticities between ferromagnetic domain-wall motions driven by magnetic field and electric current" *Appl. Phys. Lett.* **112**, 172401 (2018).

7. ***Yong-Keun Park***, Dae-Yun Kim, Joo-Sung Kim, Yune-Seok Nam, Min-Ho Park, Hyeok-Cheol Choi, Byoung-Chul Min, and Sug-Bong Choe, "Experimental observation of the correlation between the interfacial Dzyaloshinskii-Moriya interaction and work function in metallic magnetic trilayers" *NPG Asia Materials*, **10**, 995–1001 (2018).

8. Joo-Sung Kim, ***Yong-Keun Park***, Hyun-Seok Whang, Jung-Hyun Park, Byoung-Chul Min, Sug-Bong Choe, "Artifact-free optical spin-orbit torque magnetometry" *Appl. Phys. Lett*. **114**, 182402 (2019).

9. Dae-Yun Kim, Nam-Hui Kim, ***Yong-Keun Park***, Min-Ho Park, Joo-Sung Kim, Yune-Seok Nam, Jinyong Jung, Jaehun Cho, Duck-Ho Kim, June-Seo Kim, Byoung-Chul Min, Sug-Bong Choe, and Chun-Yeol You, "Quantitative accordance of Dzyaloshinskii-Moriya interaction between domain-wall and spin-wave dynamics" accepted in *Phys. Rev. B.*
10. Tomoe Nishimura, Dae-Yun Kim, Duck-Ho Kim, Yune-Seok Nam, ***Yong-Keun Park***, Yoichi Shiota, Takahiro Moriyama, Byoung-Chul Min, Sug-Bong Choe, and Teruo Ono, "Interfacial Dzyaloshinskii-Moriya interaction and damping-like spin-orbit torque in $[Co/Gd/Pt]_N$ magnetic multilayers" submission in *Phys. Rev. Applied*.
11. ***Yong-Keun Park***, Joo-Sung Kim, Yune-Seok Nam, Seyyoung Jeon, Jung-Hyun Park, Kyoung-Whan Kim, Hyun-Woo Lee, Byoung-Chul Min, and Sug-Bong Choe, "Interfacial atomic layers for full emergence of interfacial Dzyaloshinskii-Moriya interaction" Submitted to *NPG Asia Materials*.
12. ***Yong-Keun Park***, Joo-Sung Kim, Yune-Seok Nam, Ji-Sung Yu, Sug-Bong Choe, and Byoung-Chul Min, "The simultaneous achievement of thermal stability enhancement and switching current density reduction by engineering of Dzyaloshinskii-Moriya interaction" Article in preparation.
13. ***Yong-Keun Park***, Jung-Hyun Park, Sug-Bong Choe, and Byoung-Chul Min, "Oscillation of Dzyaloshinskii-Moriya interaction with quantum well in Pt/Co/Cu trilayer" Article in preparation.

Awards and Scholarship

Sept. 2008.
- Dec. 2013. Tuition scholarship from Inha University
Feb. 2014. Graduation with Summa Cum Laude
Mar. 2019.
- Aug. 2019. Brain Korea 21 (BK 21) scholarship
Jun. 2019. Scholarship in 10^{th} International symposium on Metallic Multilayers (MML)

Research Experience

Jul. 2012
- Feb. 2014. **Quantum Functional Materials Laboratory in Inha University**

Hydrothermal synthesis of $(Na,Li)NbO_3$
Measurement of piezoelectricity of $(Na,Li)NbO_3$
Measurement of pyroelectric current generation in PMN-PT film
Measurement system setup for measurement of pyroelectricity
Powder XRD measurement

Mar. 2014.
- Feb. 2020. **Terahertz Magnetic Nano-device Laboratory in Seoul National University**

&

Feb. 2015.
- Feb. 2020. **Center for Spintronics, Post-silicon Semiconductor Institute in Korea Institute of Science and Technology**

Ultrathin ferromagnetic film & oxide film fabrication
Micro-&nano-size structure patterning via Photolithography & E-Beam Lithography
Dry etching process
Maintaining of ultrahigh vacuum sputter system
Optical measurement of domain wall motion via MOKE
Electrical measurement of magnetization switching
GI-XRD
Atomic force microscopy
Vibrating sample magnetometer with temperature variation